

# UC Santa Cruz

## UC Santa Cruz Electronic Theses and Dissertations

### Title

Local Structure of Metastable Defect Complexes and Phase Transitions

### Permalink

<https://escholarship.org/uc/item/1v5417xq>

### Author

MacKeen, Cameron

### Publication Date

2019

### Supplemental Material

<https://escholarship.org/uc/item/1v5417xq#supplemental>

### License

[CC BY-NC 4.0](#)

Peer reviewed|Thesis/dissertation

UNIVERSITY OF CALIFORNIA  
SANTA CRUZ

**LOCAL STRUCTURE OF METASTABLE DEFECT COMPLEXES  
AND PHASE TRANSITIONS**

A dissertation submitted in partial satisfaction of the  
requirements for the degree of

DOCTOR OF PHILOSOPHY

in

PHYSICS

by

**Cameron MacKeen**

March 2019

The Dissertation of Cameron MacKeen  
is approved:

---

Professor Frank Bridges, Chair

---

Professor Sue A. Carter

---

Professor David P. Belanger

---

Dean Lori Kletzer  
Vice Provost and Dean of Graduate Studies

Copyright © by  
Cameron MacKeen  
2019

# Table of Contents

List of Figures	v
List of Tables	xii
Abstract	xiv
Dedication	xvi
Acknowledgments	xvii
<b>1 Introduction</b>	<b>1</b>
1.1 Organic Perovskites . . . . .	5
1.2 Calcium Fluorite . . . . .	8
1.3 Lithium Niobate . . . . .	9
<b>2 X-ray absorption background</b>	<b>11</b>
2.1 Theoretical . . . . .	11
2.1.1 Generalized Pair-Distribution Function . . . . .	16
2.2 Experiment . . . . .	19
2.3 Analysis . . . . .	21
<b>3 Organic Lead Halide Perovskites: Coordination, and Vibration</b>	<b>25</b>
3.1 Evolution of Iodoplumbate Complexes in Methylammonium Lead . . . .	25
3.1.1 Introduction . . . . .	26
3.1.2 Sample Preparation . . . . .	30
3.1.3 Data Acquisition . . . . .	30
3.1.4 EXAFS Data Reduction and Fitting . . . . .	32
3.1.5 Results and Discussion . . . . .	33
3.1.6 Conclusions . . . . .	45
3.2 Anharmonicity in MAPbBr <sub>3</sub> . . . . .	47
3.2.1 EXAFS Data . . . . .	49
3.2.2 Fits . . . . .	59

<b>4</b>	<b>Calcium Fluorite doped with Ytterbium</b>	<b>75</b>
4.1	Overview . . . . .	75
4.2	Shortcoming of Impurity Trapped Exciton Model . . . . .	77
4.3	Role of Interstitial Fluorine Defects in Meta-stable Valence States . . .	83
4.3.1	Calculations . . . . .	86
4.4	Results . . . . .	87
4.4.1	XANES . . . . .	87
4.4.2	EXAFS . . . . .	92
4.4.3	Anomalous Emission . . . . .	101
4.5	Experimental methods . . . . .	103
4.5.1	Theoretical Calculations and $F_i$ Dynamics . . . . .	105
4.6	Conclusion . . . . .	113
<b>5</b>	<b>Doped Lithium Niobate</b>	<b>115</b>
5.1	Lithium Niobate Doped with of Zinc . . . . .	115
5.1.1	Local environment about the Li and Nb sites . . . . .	119
5.1.2	EXAFS data and analysis . . . . .	119
5.2	$Er^{3+}$ , $In^{3+}$ , and $Hf^{4+}$ Dopants . . . . .	130
5.2.1	Substitution models for In and Er . . . . .	132
5.2.2	Substitution models for Hf . . . . .	132
5.2.3	Ionic radii . . . . .	133
5.2.4	EXAFS data and analysis . . . . .	134
5.2.5	Fits of data . . . . .	138
5.2.6	Discussion . . . . .	148
5.3	Experimental details . . . . .	159
5.3.1	Zinc . . . . .	159
5.3.2	In, Er, Hf . . . . .	161
	<b>Bibliography</b>	<b>163</b>

# List of Figures

1.1	Diagram showing anomalous emission intensity is inversely related to total $\text{Yb}^{2+}$ concentration. . . . .	8
3.1	k-space data of the measured samples. Note that the trace for $\text{PbI}_2$ (top) is multiplied by 0.5, to be on the same scale as the other samples. . . .	31
3.2	angle=270 . . . . .	34
3.3	Fourier transform of eq 2 (i.e., EXAFS equation), $\text{FT} [k\chi(k)]$ , vs r-space distance from the absorbing Pb atom (r). Both the magnitude (outer envelope) and the real part (inner curves) of the Fourier transform are shown for the data. The left column shows the extended X-ray absorption fine structure (EXAFS) r-space data for six frozen single-step $\text{MAPbI}_3$ precursor solutions with corresponding fits: $\text{PbI}_2$ , 1:1 $\text{PbI}_2$ :MAI, 1:1.5 $\text{PbI}_2$ :MAI, 1:3 $\text{PbI}_2$ :MAI, 1:1 $\text{PbI}_2$ :MAI with 0.5 M HI, and 1:1 $\text{PbI}_2$ :MAI with 1.0 M HI (from top to bottom, respectively). The right column shows the individual components used in the fits for each sample. . . . .	36
3.4	Pb-I bond lengths from our experimental data (black, red and blue) and selected literature values of compounds relevant for $\text{MAPbI}_3$ fabrication (green). Note that our data most closely resembles $\text{PbI}_2$ -DMF(1) [1] and $\text{PbI}_2$ -DMF(2) [2] albeit with longer terminal Pb-I bonds, especially in the samples containing HI. . . . .	37
3.5	Real-space extended X-ray absorption fine structure (EXAFS) fit parameters extracted from Figure 1. The top panel plots the correlated Debye-Waller factor ( $\sigma^2$ ), the middle panel the Pb—I components positions from the absorbing Pb atom, and the bottom panel the total iodide coordination number of the Pb atoms in solution. Note that disorder increases as the value of $\sigma^2$ increases and the Pb atoms in both $\text{PbI}_2$ and $\text{MAPbI}_3$ exhibit octahedral iodide coordination ( $\text{PbI}_6$ ). . . . .	38
3.6	Pb L-III edge X-ray absorption near edge structure (XANES) spectra of the measured samples. The legend refers to the $\text{PbI}_2$ :MAI molar ratio with the $\text{PbI}_2$ sample not containing any MAI. . . . .	41

3.7	Linear combination fit of the 1:1 PbI <sub>2</sub> :MAI X-ray absorption near edge structure (XANES) data. . . . .	42
3.8	angle=270 . . . . .	50
3.9	Low temperature (10K) Br e-space near-edge with two different 12 spline background fits. The automatic background fits itself to the expected multielectronic excitation hump, which then results in a poor background near $E_{min}$ . By manually fixing a knot, we minimize low-r amplitude in r-space. . . . .	52
3.10	angle=270 . . . . .	53
3.11	Br K-edge data in k-space that exhibits a similar temperature dependence. Upon closer inspection of zero-crossings, there is an accordian effect similar in magnitude to Pb L <sub>III</sub> edge data. . . . .	54
3.12	After reducing Br K-edge data by removing residual Pb absorption and manually spline fitting, we transform into real space to find a clear peak $\sim 3$ Å. Then we can back fourier transform only this first peak, associated with nearest neighbor Pb coordination, to see individual contribution to the anharmonicity in the k-space data is due to the nearest neighbor. . .	56
3.13	Back transformation into k-space of the first Pb–Br peak in Pb edge r-space data. . . . .	57
3.14	angle=270 . . . . .	58
3.15	Fit for the average (6 scans) Br 10K data. . . . .	60
3.16	Fit for the average (6 scans) Pb 10K data. . . . .	61
3.17	Shift in bond length (nominally 2.977 Å) for the Pb–Br bond as a function of temperature, extracted from Pb edge data. The vertical black lines represent the nominal temperatures for orthorhombic to tetragonal transition (left), and the tetragonal to cubic transition (right). These values were fixed in Br edge fit due to the correlation between $C_3$ and $\Delta r$ . There is a smooth increase in bond-length until part-way through the tetragonal phase, where there appears to be a small step. . . . .	63
3.18	Fit parameter $\sigma^2$ for the first neighbor of each edge. This shows nearly identical broadening with temperature, taking a linear form without major discontinuity at nominal phase transition temperatures. . . . .	64
3.19	A blown-up example of how $\Delta k$ is measured in back-transformed Br k-space data. . . . .	67
3.20	Asymmetric fit parameter $C_3$ of the first neighbor for both edges in black squares and red triangles for the Br–Pb and Pb–Br peak respectively. This quantifies the anharmonic motion resulting in an asymmetric pair distribution, likely due to the transverse motion of Br at the octahedral corners. In blue and purple triangles is the $C_3$ parameter extracted from the temperature dependence of zero-crossings in k-space. One can see how closely it follows the $C_3$ from fitting. . . . .	68
3.21	A blown-up example of isosbestic point in back fourier transformed Br data, $k_{b,n}$ , and it's relative value compared to corresponding zero-crossings.	70

3.22	A comparison of isosbestically integrated $C_3$ and $C_3$ from fitting, with Pb results on the left, and Br results on the right. The dashed red curve shows error bounds when extracting $k_{b,n}$ from an isosbestic region, and demonstrates the sensitivity of the integrated $C_3$ when isosbestic regions are not point-like. . . . .	72
3.23	Symmetric distributions (solid lines) are plotted with their asymmetric counterparts (dashed lines) using $r$ and $\sigma^2$ values at several temperatures extracted from fitting. Asymmetric distributions plotted here are piecewise functions defined as : $\frac{\alpha^{1+s}}{\Gamma[1+s]}(r-r_0)^s e^{-\alpha(r-r_0)} \Theta(r-r_0)$ [3]. With a positive $C_3$ , the peaks of asymmetric distributions reside at lower $r$ than symmetric distributions, but exhibit a high tail as $r$ increases. . . . .	73
4.1	The normalized Yb $L_{III}$ edge absorption coefficient, $\mu$ , as a function of total Yb concentration (0.01, 0.05, and 0.1 % Yb) for fresh samples at 10 K. The $Yb^{2+}$ peak is at 8942 eV while the $Yb^{3+}$ peak at 8949 eV. The $Yb^{3+}$ peak still dominates even at the lowest concentration, 0.01% Yb. .	78
4.2	Fit of the $L_{III}$ edge for the 0.01% Yb sample. The normalized data are shown as circles while the fit is shown as a green line. The blue and red pseudo-Voigt peaks show the contributions for $Yb^{2+}$ and $Yb^{3+}$ respectively; the main step function is shown as a purple line. . . . .	80
4.3	The estimated $Yb^{2+}$ and $Yb^{3+}$ concentrations and the relative anomalous emission intensity (see Fig. 4.4) as a function of the nominal concentration $n_o$ (0.01–0.1% Yb) for fresh samples. It is clear that the emission intensity is not directly proportional to the concentration of $Yb^{2+}$ ions. . . . .	81
4.4	The anomalous emission spectra are plotted for the samples studied using XANES, keeping the geometry the same and the incident UV power level constant. . . . .	82
4.5	Evolution of Yb $L_{III}$ XANES spectra as a function of x-ray exposure time $t$ for multiple scans at 200 K, for $CaF_2:Yb$ (.01%). At $t = 0$ , the sample had some x-ray exposure and Yb was already slightly reduced. The 8942 eV peak is associated with $Yb^{2+}$ and the 8949 eV peak with $Yb^{3+}$ . Over $\sim 3$ hrs, the valence changes from mostly 3+ to mostly 2+. Note also the changes in the EXAFS range above 8955 eV. Insets: a): XANES from a different experimental run; little x-ray exposure (open black circles), after x-ray exposure at 200 K ( $\sim 4$ hr - red) from multiple EXAFS scans at the Yb $L_{III}$ , and after heating to 320 K (green squares). The scan at 320 K has slightly less $Yb^{2+}$ than the initial scan. b): Similar changes when another fresh sample is exposed to x-rays at 7940 eV, 1 keV below the Yb $L_{III}$ edge. The same valence reduction occurs over a time period of 200 min. (red solid curve). . . . .	88



4.6	The fraction of $\text{Yb}^{2+}$ ( $f(2+)$ ) as a function of x-ray exposure time at 200 K for .01% Yb; $f(2+)$ changes from about $\sim 0.3$ to 0.7, and varies roughly logarithmically with $t$ (lines). Insets: a) Sum of the integrated areas for the two peaks as a function of $\text{Yb}^{2+}$ fraction. This sum decreases slightly as the valence decreases from mostly 3+ to mostly 2+. b) An example of a fit of the XANES to two pseudo-Voigt peaks plus a step function.	90
4.7	Examples of $k$ -space data at the Yb $\text{L}_{\text{III}}$ edge for the fresh sample, and after full valence reduction.	93
4.8	EXAFS $r$ -space data at 10 K for a fresh sample, and after maximum valence reduction. Peaks in the EXAFS data correspond to shells of neighbors surrounding the Yb defect. The fast oscillatory function is the real part $R$ of the Fourier transform (FT) while the amplitude functions are $\pm\sqrt{R^2 + I^2}$ ; $I$ is the imaginary part of the FT. There is a large increase in the distance ( $\sim 0.15$ Å) for the first peak near 1.9 Å, for the valence reduced sample (red trace), compared to the as-made sample (black). In contrast for the second, Yb-Ca peak, the pair distance changes very little upon valence reduction.	94
4.9	Fits of the real space data for the fresh sample (top) and the valence reduced sample (bottom) using the model discussed in the text. The Fourier transform window is $3.5\text{-}10.0$ Å $^{-1}$ , with a $0.3$ Å $^{-1}$ Gaussian rounding; the fitting range in $r$ -space is $1.5\text{-}4.7$ Å.	96
4.10	Top: full fit to fresh sample (green line) and data (red squares). The components for the fit are plotted individually below the total fit. The nearest neighbor F peak is fit using two Yb-F standards with different parameters (see Table 4.1); the larger near neighbor peak (red) corresponds to $\text{Yb}^{3+}$ and has a shorter Yb-F bond length. At the bottom, the three multi-scattering (MS) peaks are offset and plotted on an expanded vertical scale (X 3.3); the lowest plot which peaks near 4 Å dominates the MS contributions and is nearly out of phase with the long Yb-F peak.	97
4.11	Top: full fit to the reduced sample (green line) and data (red squares). Components are plotted individually below the total fit. The main differences are the shift of the first peak to higher $r$ (the larger near neighbor peak (black) corresponds to $\text{Yb}^{2+}$ ) and the prominence of the second fluorine peak compared to the fresh sample fit. At the bottom, again on an expanded vertical scale (X 3.3), the small MS components are plotted. The farthest multi-scattering peak occurs at a higher $r$ (peaks near 4.15 Å) compared to the fresh sample near 4.0 Å, and is reduced in amplitude due to broadening.	98
4.12	The normalized absorption spectra shows that the UV absorption centered at 3.4 eV (365 nm) remains relatively unchanged between the fresh samples and the x-ray exposed sample that no longer exhibits the anomalous luminescence.	101

- 4.13 Normalized plots (80 K) of the yellow-green emission for two samples never exposed to x-rays (red circle; green diamond), the sample with extensive x-ray exposure (black, not normalized) and the x-ray exposed sample after annealing at 900 K (square purple symbols). The nearly flat (black) trace for the x-ray exposed sample has a remnant from the background subtraction. Each scan can be fit to a sum of three Lorentzians; importantly, the relative amplitudes of the components for the annealed sample are different. . . . . 102
- 4.14 A diagram of different meta-stable states observed in  $\text{CaF}_2\text{:Yb}(.01\%)$ . As-made sample exhibits anomalous luminescence (AE) and most Yb in  $3+$  state with a non-local charge compensating  $\text{F}_i^-$ . X-ray exposure at 200K excites interstitial  $\text{F}^-$  resulting in recombination and an increased amount of  $\text{Yb}^{2+}$  while quenching AE. Warming to room temperature increases  $\text{F}_i^0$  mobility and locally compensated  $\text{Yb}^{3+}$  complexes emerge, but AE does not return. . . . . 105
- 4.15 Partial representation of a fluorite crystal structure surrounding one Yb dopant ion in blue, located in the  $\text{YbF}_8$  cube that is shaded in blue. Some of the  $\text{Ca}^{2+}$  ions located at the center of every other cube are plotted in light grey; crystal fluoride ions in green are located at the vertices of all cubes. Five cubes around interstices are shaded in colors (dark grey, violet, green, red, and magenta); at their center an interstitial fluoride ion  $\text{F}_i^-$  is indicated in the same color. The distance from the Yb ion (in blue) and each of the interstitial fluorides plotted are:  $d_{\text{F}_i-\text{Yb}} = 2.73$  (dark grey), 4.73 (violet), 6.11 (green), 8.19 (red), and 13.7 Å (magenta). Each *ab initio* calculation comprises the  $\text{YbF}_8$  cluster and one of the five  $\text{F}_i\text{F}_8$  cubes embedded in the fluorite crystal. See text and Figs. 4.16 for details. . . . . 106
- 4.16 Diabatic configuration coordinate energy diagrams for  $\text{F}_i^-/\text{Yb}^{3+}$  electron transfer in  $\text{CaF}_2$  at different  $\text{F}_i-\text{Yb}$  distances are plotted together in this figure. The diagrams show the existence of a critical distance  $d_{\text{F}_i-\text{Yb}}^{\text{critical}} \simeq 8.19\text{Å}$ . For  $d_{\text{F}_i-\text{Yb}} < d_{\text{F}_i-\text{Yb}}^{\text{critical}}$  the  $\text{F}_i^0-\text{Yb}^{2+}$  minima lie on the left and above the  $\text{F}_i^--\text{Yb}^{3+}$  ground state in the grey region, hence the hole-electron  $\text{F}_i^0-\text{Yb}^{2+}$  pair spontaneously recombines; for  $d_{\text{F}_i-\text{Yb}} > d_{\text{F}_i-\text{Yb}}^{\text{critical}}$  they lie on the right and below the  $\text{F}_i^--\text{Yb}^{3+}$  ground state curve, in the white region, hence the  $\text{F}_i^0-\text{Yb}^{2+}$  hole-electron pair state is metastable. Note that when  $\text{F}_i^0$  moves away from (or towards)  $\text{Yb}^{2+}$  after reduction, the energy curve of the  $\text{F}_i^0-\text{Yb}^{2+}$  hole-electron pair shifts down (or up). The  $\text{F}_i^0-\text{Yb}^{2+}$  ground state minima are connected with a vertical dotted line for comparisons. At very large separations the energy for the  $\text{F}_i^0-\text{Yb}^{2+}$  hole-electron pair is only slightly higher than that for the  $\text{F}_i^--\text{Yb}^{3+}$  ground state and is not seen on this scale. . . . . 107

5.1	The environment about the Li (top) and Nb (bottom) sites in LiNbO <sub>3</sub> . Bonds are shown for the nearest O atoms and the pair distances for the first few shells are indicated for each site. . . . .	120
5.2	Left: the $k$ -space data for sLNO (0.7 mol% Zn) and cLNO (4.4 mol% Zn) samples; sLNO black line, cLNO red dashed line, at 10K. The data for sLNO have more noise at high $k$ because of the much lower Zn concentration, and this limits the Fourier transform (FT) range. Right: Plot of the corresponding fast FT (FFT) of the $k$ -space data with an FT window 3.8-13.2 Å <sup>-1</sup> ; the FT window is Gaussian rounded using a width, 0.2 Å <sup>-1</sup> . There is a tiny difference between the data for sLNO and cLNO - the sLNO $r$ -space plot has a slightly larger amplitude ( $\sim 1\%$ ) for all Zn-Nb peaks, consistent with a lower dopant concentration. For the $r$ -space data (here and in later plots), the fast oscillating function is the real part, $R$ , of the FFT while the amplitude is $\pm\sqrt{R^2 + I^2}$ where $I$ is the imaginary part of the FFT. . . . .	123
5.3	A fit (solid line) of the Zn K edge data (squares) for sLNO with 0.7 mol% Zn, to a sum of functions calculated using FEFF[4]; the $r$ -space fit range was 1.3-4.3 Å, and the FT range was 3.8-13.2 Å <sup>-1</sup> ; remaining degrees of freedom, 4. The fit is excellent over the entire fit range, particularly near 3.5 Å where a large Zn-Nb peak would exist if significant Zn were on the Nb site. The main individual peaks are plotted beneath the fit; the weak peaks for more distant neighbors - and also two MS peaks - are shown in an expanded view (zoomed by 2.5) in bottom panel. . . . .	125
5.4	The effect on the EXAFS plot if a small Zn-Nb peak with an actual distance of 3.76 Å, corresponding to 10 % Zn on the Nb site, is added to 90 % of the fit to the Li site. This adds a peak near 3.4-3.5 Å on the EXAFS plot, and even for this small amount of Zn on Nb, the shape of the real part of the transform, $R$ , is changed significantly. . . . .	128
5.5	$k^2\chi(k)$ vs $k$ from top to bottom: at the In K edge, black - cLNO, 0.7 mol% In, blue - 2.8 mol% In; at the Er L <sub>III</sub> edge, red - sLNO, 0.55 mol% Er, purple - cLNO, 2.3 mol% Er; and at the Hf L <sub>III</sub> edge, green - sLNO, 0.57 mol% Hf. The plots are displaced vertically for clarity. . . . .	135
5.6	Comparison of the $r$ -space data [FT $k^2\chi$ ] for 0.7 mol% and 2.8 mol% In doped cLNO at 10 K. The FT range is 4.1 - 14.7 Å <sup>-1</sup> . The differences between the two traces are very small, with the largest deviations in the 2.75-3.25 Å range. In this and subsequent $r$ -space plots the fast oscillation is the real part $R$ of the FT while the envelop function is $\pm\sqrt{R^2 + I^2}$ where $I$ is the imaginary part of the FT. . . . .	136

5.7	Top: Comparison of $r$ -space data at 10 K for 0.55 mol% Er in sLNO (red) and 2.3 mol% Er in cLNO (blue). The largest change is at the Er-Nb peak near 2.9 Å which is smaller in the sLNO sample, suggesting possibly less Er on the Li site for sLNO. The FT range is 4.1 - 11.5 Å <sup>-1</sup> . Bottom: $r$ -space data at 10 K for 0.57 mol% Hf in sLNO (blue). Note the smaller amplitude near 2.9 Å, and the larger peak near 3.6 Å compared to the Er (or In) data, indicating some Hf is on an Nb site. FT range is 3.8-12.7 Å <sup>-1</sup> . . . . .	137
5.8	Fits of the $r$ -space data [FT $k^2\chi$ ] for 0.7 mol% In doped LiNbO <sub>3</sub> at 10 and 300K (data - blue squares; fit - red lines); see text for model. The amplitude at 300K is significantly reduced from thermal vibrations for the In-Nb peaks above 2.5 Å. The FT range is 4.1-14.7 Å <sup>-1</sup> , while the fit range is 1.2-3.9 Å; $S_0^2 = 1.0$ . . . . .	139
5.9	Fits of the 0.55 mol% Er (sLNO) and 2.3 mol% Er (cLNO) at 10 K (data - blue squares; fit - red line). A good fit is achieved up to $\sim 4.5$ Å; see text for model and Table 5.5 for main parameters. The FT range is 4.1-11.5 Å <sup>-1</sup> and fit range is 1.1-4.6 Å. . . . .	143
5.10	Fits of the 0.57 mol% Hf (sLNO) at 10 K (data - blue squares; fit - red line). A good fit is achieved up to 4.5 Å; see text for model and Table 5.6 for main parameters. The FT range is 3.8-12.7 Å <sup>-1</sup> with a Gaussian rounding of the FT window by 0.2 Å <sup>-1</sup> ; the fit range is 1.0-4.2 Å. . . .	146
5.11	M-Nb distances for the first two Nb neighbors about the Li site vs type of dopant on the Li site. The dotted horizontal lines are the Li-Nb distances at 3.06 and 3.36 Å for the undistorted lattice. The M-Nb pair distances increase with valence (and also the dopant ionic radius) except for the Hf dopant. . . . .	149
5.12	Top: Plot of the solution energies of In dopants for models (i), (ii) , and (iii) of Ref. [5] as a function of T to show extrapolations to higher T. These extrapolations suggest that the lowest energy model may change when the defect is frozen in at high temperatures, thus motivating defect calculations at much higher temperatures. Bottom: Similar extrapolations for the three lowest energies for Hf dopants[6]. Although scheme (vi) is lowest below room temperature, scheme (ii) is lower at high T. . .	156

# List of Tables

4.1	Results of the EXAFS fits for the fresh and valence reduced samples; $\text{Yb}^{2+}\text{-F}$ and $\text{Yb}^{3+}\text{-F}$ are for sites with valence 2+ and 3+ respectively. Fit range in $r$ -space, 1.5-4.7 Å. The amplitude is the degeneracy for each shell, but is split for the first shell as a result of the two valence states. $\sigma^2$ is the correlated Debye Waller factor where $\sigma$ is the width of the pair distribution function. The errors show the reproducibility of the data in fits of multiple scans. Including systematic effects the errors for $r$ are $\sim 0.01$ Å for the first two neighbors, and up to .02 Å for further peaks. Due to the correlations between N and $\sigma$ , systematic uncertainty is typically 10-15% for these parameters. $S_0^2 = 1.0$ . . . . .	100
5.1	Fit results for the Zn K edge data at 10K, for the sLNO (0.7 mol%) and cLNO (4.4 mol%; nominal 5 mol%) samples, plus distances from diffraction (Diff.). The Zn-O3 shell represents two longer Zn-O shells (three neighbors each at 3.28 and 3.43 Å; which collapse to a single peak with six O neighbors at an average distance near 3.25 Å. The second column gives corresponding pair distances about the Li site from diffraction for congruent $\text{LiNbO}_3$ . The errors for $r$ are $\pm 0.01$ Å for the major peaks and most relative errors for $\sigma^2$ are $\pm 0.0005$ Å <sup>2</sup> . However systematic errors in $\sigma^2$ can be $\sim 10$ %. . . . .	124
5.2	Ionic radii tabulated by Shannon[7] for different dopants and host cations with 6-fold coordination. The $\text{O}^{2-}$ ionic radius corresponds to an oxygen in 4-fold coordination with it's neighbors. The much larger radius of $\text{Er}^{3+}$ compared to other ions results in the larger positive shifts in bond length for Er-O bonds. . . . .	134
5.3	Summary of dopants studied and type of host crystal (sLNO or cLNO) with measured concentrations given in mol %. . . . .	134
5.4	Fit parameters for fits of the In data. The In-O3 peak near 3.3 Å is a sum of two peaks at nominally 3.29 and 3.43 Å in pure $\text{LiNbO}_3$ (only the average - 3.36 Å is listed below, under diffraction. The In-In peak assumes that In-In pairs form in Li sites 3.77 Å apart.) . . . . .	141

5.5	Table of significant fit parameters. Due to the relatively large ionic radius of Er, all significant peaks have a positive shift in bond length. Note the Er-O3 peak is a sum of peaks at 3.29 and 3.43 Å in undistorted crystal; average distance 3.36 Å. The difference between the stoichiometric and congruent sample is negligible. . . . .	145
5.6	Fit parameters for the Hf L <sub>III</sub> edge data. The subscript on the pair indicates the substitution site, except for Hf-O2; this peak is the sum of three peaks at distances 2.06 and 2.26 Å from the Li site and 2.14 Å from the Nb site; average distance 2.15 Å (for 50 % occupation of each site). The average Li site Hf-O3 distance in the undistorted lattice is 3.36 Å, the average of 3.29 and 3.43 Å. Similarly the Nb site average Hf-O4 distance is 3.673 Å, the average of 3.620 and 3.73 Å. For this particular fit the fraction of Hf on an Nb site was 53%; however because of interference, the fit is sensitive to the initial parameters - in particular, the values for $\sigma^2$ and the substitution site fraction are correlated. From many different fits the occupation is $50 \pm 10\%$ on each site. The errors for $\sigma^2$ are also large $\sim 10\%$ . . . . .	147

## Abstract

### Local Structure of Metastable Defect Complexes and Phase Transitions

by

Cameron MacKeen

To understand and predict phenomena in solid materials, we often look at how the lattice structure brings about such an effect. Our lab analyzes the extended x-ray absorption fine structure (EXAFS) to closely study the physical configuration of atoms in a lattice. I will talk about the interesting local structure of the following compounds: Organic lead-halide perovskites  $\text{MAPbI}_3$  and  $\text{MAPbBr}_3$ , ytterbium doped calcium fluoride ( $\text{CaF}_2\text{:Yb}$ ), and lithium niobate doped with Zn,Er,In, and Hf.

Organic perovskites have been a material of high interest for harvesting light. In order to improve crystallization of solution based methylammonium lead iodide ( $\text{MAPbI}_3$ ), we aim to maximize lead-iodide coordination via an excess of iodide precursors: methylammonium iodide (MAI) and hydroiodic acid (HI). We find that a surplus of HI results in higher order and coordination for the nearest Pb–I atomic shell (six iodine neighbors). In another study, we look into the disorder and vibrational properties of  $\text{MAPbBr}_3$  in different structural phases. This dissertation includes a temperature dependent study on the local structure of  $\text{MAPbBr}_3$ , and a rigorous quantifying of the anharmonicity parameter,  $C_3$ , that represents dynamic disorder.  $C_3$  increases nonlinearly with temperature and results in an asymmetric pair distribution for the nearest Pb–Br shell.

Calcium fluoride doped with ytterbium is a doped simple FCC crystal with a down-shifted anomalous luminescence. A long lived excited state decays with a yellow-green emission and can be induced with UV exposure. With two consistent methods quantifying amount of Yb in the 2+ and 3+ state, we present compelling evidence that the impurity trapped exciton model does not explain this system. Further, we can elucidate the various metastable states of this system and their relation to strange observations.

Finally, lithium niobate has piqued interest in frequency conversion device engineering as a non-linear optical material. There lacks a general model for how the photorefraction is affected by different species of dopants, but there are proposed charge compensating substitution schema. We judge models of substitution schema based on solution energy calculations using our EXAFS results of lithium niobate doped with zinc, indium, erbium, and hafnium.



*Dedicated to my parents, Kenneth and Virginia, who nurtured curiosity ever  
since taking Brendon and me to a field to gaze upon Hale-Bopp.*

## Acknowledgments

First and foremost I am grateful to Frank “Bud” Bridges; he has been the most helpful, hard-working, and intellectually humble person with whom I have had the pleasure to work. I would also like to especially thank the members of my committee, Dave Belanger and Sue Carter for their time, insightful commentary and guidance.

I am grateful to the students who shared countless hours in the lab with me and who shared shifts at SLAC National Laboratory with me. These include graduate students Leila Jewell, Renee Sully, Trevor Keiber, Katie Hellier, and Valentin Urena Baltazar; and undergraduates Allen Miller, Patrick Nast, Nathan Martinez, Mika Remulla, Ryan Dudschus, Logan Knudson, and Jason Gruzdas.

I want express my appreciation to all of those who made or shared samples for the research: Drew May, Brian Maple, Laszlo Kovács, Ghada Abdelmageed, Mike Reid, Jon-Paul Wells, David Cahen and Yevgeny Rakita. I also want to thank our other collaborators for their efforts and thoughtful discussion, this list includes Luis Seijo, Z. Barandiarán, Mike Reid, Jon-Paul Wells, Ryand Davis, Apurva Mehta, Laszlo Kovács, Mike Toney, Drew May, and Mike Kozina. Finally, I would like to thank the colleagues I lived with, Joe Schindler, Christoph Lee, and Webster Rasmussen. Many fond memories scrambling out of boulder fields with Christoph, fun times talking disc with Joey , and rugged tasks with Webster dismantling the junk Ford explorer. I hope to break broth with them again.

# Chapter 1

## Introduction

To understand and predict phenomena in solid materials, we often look at how the lattice structure brings about such an effect. In considering the general dependence of phase transitions on broken symmetry, it seems appropriate to closely study the physical configuration of atoms in a lattice. Specifically, the defects that break these symmetries affect how energy is minimized in the crystal structure. As different symmetry groups allow different phases of matter (i.e. ferroelectricity and noncentrosymmetry), manipulating fundamental material properties can often be done by controlling defects. To initiate the evolutions of crystal engineered devices, we need to know a few things to exploit a novel behavior. We need to know how to recreate the phenomena reliably, and control it. In order to achieve that, we need to know why a defect or change in the structure results in the peculiar characteristic.

The Bridges' group studies a variety of materials (mostly inorganic) by investigating experimentally observed phenomena and the corresponding series of models

developed by theorists. We employ extended x-ray absorption fine-structure (EXAFS) analysis to probe the local structure around different atomic species in a material. Further we investigate general electronic properties, like valence state, by looking at the X-ray Absorption Near-edge Structure (XANES). Details and background on our experimental technique will be provided in the subsequent chapter. In each of our experiments, we vary different environmental parameters (dopant conc., fabrication method, temperature, x-ray exposure time) to dig into how the local structure changes overall material characteristics.

In exploring the physical mechanisms responsible for properties of a material, we rely on studying a material in its different states. Simply, if we change a parameter that turns a phenomenon "on" or "off" (like magnetism) then we can collect x-ray absorption data of the system in both states. From this x-ray absorption data at a particular edge, we aim to extract system details like neighboring atom species, bond-length, bond stiffness (correlated Debye-Waller factor), and coordination. In many of our studied materials peculiar phenomena are a result of defects in the system. These defects can vary from local point defects to extended complexes, consisting of a dopant (extrinsic) or vacancies (intrinsic) situated on another atom's site (substitution), or in between lattice positions (interstitial).

A popular type of defect that is introduced by sample makers is an extrinsic defect from low concentrations of dopants. Our experimental approach is appropriate because we can explicitly deduce the neighborhood around the dopant atom to see if it is the same as another atoms in the compound. If so, then we conclude that the dopant is

substituting on a particular site, but often we will find local distortions of bond-length which may be due to a different preferred valence or a different ionic radius. Upon successfully delineating the structural parameters of our sample, the final step is relating the structure to the observed physical properties.

Our experiments are instigated by a few collaborating parties which include a group that has modeled a defect scheme and a group that can provide us a sample. It is our interest to provide definitive empirical parameters for what the local structure looks like, mostly in an effort to rule out or confirm the plausibility of certain models. It is crucial to intricately and fundamentally understand how local structure affects macroscopic (or microscopic) properties if we want to realize the full potential of future crystal engineered devices. While it is true engineers can exploit a phenomenon that is misunderstood, optimization seems to rely on a comprehensive knowledge of the underlying physics.

All except for the organic perovskites of the compounds included in this manuscript are investigated for defect type, formation, and consequence to characteristics. Organic perovskites have been a material of high interest for harvesting light. Organic lead halide perovskites have a small and tunable band gap and long charge carrier diffusion lengths. Higher efficiency and reliability is sought and can be achieved by understanding the pathways to degradation and maximize halide coordination. There are further questions about organic lead halide perovskites, like the mechanism for their limited radiative recombination rate [8], that have provoked us to look into the disorder and vibrational properties of  $\text{MAPbBr}_3$  in different phases.

Calcium fluoride doped with ytterbium is a doped simple FCC crystal with a down-shifted anomalous luminescence. A long lived excited state decays with a yellow-green emission and can be induced with UV exposure. Originally we wanted to collect EXAFS data of the transient relaxing state due to it's longevity, but found more nuances to the system. After collaborating with theorists who specialized in simulating complex electronic excitations, we found clear evidence that the old model of an impurity trapped exciton could not be valid, and instead the phenomenon observed is described by an inter valence charge transfer model.

Finally, lithium niobate has piqued interest in different eras as a non-linear optical material. In the 60's and 70s, the remarkable photo-refractive behavior was explored as a way of writing holographic memory [9]. Today, the engineers seek to minimize photorefractive response to take advantage of the second harmonic generation. In specialized applications where quasi phase matching is used to increase frequency generation device efficiency, engineers seek to periodically pole doped lithium niobate [10]. There lacks a general model for how the photorefraction is affected by different species of dopants, so we are still left with empirical evaluation of possible candidates. To start, we aim to judge models of substitution schema based on our EXAFS results of lithium niobate doped with zinc, indium, erbium, and hafnium.

## 1.1 Organic Perovskites

Organic and inorganic lead halide perovskites (HaPs) have attracted a great amount of attention for inexpensive and efficient light harvesting and as light to electrical power converting materials. The efficiency of solar cells based on HaPs, has increased extremely rapidly in the last few years and with solution engineered films has already reached power conversion efficiencies  $> 20\%$  [11]. This class of light harvesters comprised of relatively earth-abundant materials are among the strongest candidates for affordable solar photovoltaic (PV) devices [12]. Characteristics that stand out include high quantum efficiency, a low electron-hole recombination rate, a long diffusion length and a slow scattering rate, plus a low, but quite reasonable mobility; there are also indications of ion mobility and ferroelectricity [13] see Reviews [12] [14]. Further evidence suggests that the electronic properties are coupled to phonons and recent measurements indicate strongly anharmonic behavior at 300K [15] and above [16] These materials are therefore expected to have many defects, but if they do, then the implication is that many defects are not optically and electronically active. If indeed significant densities of optoelectronically inactive mobile point defects are present, those might allow self-repair of these materials, although doing so usually decreases device performance [14]. It is important to understand how the unusually good properties of halide perovskites arise, and thus, a solid understanding of defects and disorder is needed. To date there have not been extensive investigations of the local structure of a pure (as-made) lead halide perovskite as a function of temperature, although detailed measurements at 300K [17]

and 350K [16] exist. Diffraction studies have shown that MAPbI<sub>3</sub> crystals undergo a structural phase transition from cubic to tetragonal at T 327 K, and from tetragonal to orthorhombic at T 162K [18] [19] [20]. Further, there remain questions about the optoelectronic properties of the halide perovskites (i.e., the low rate of recombination and limited mobility), answers to which may be discovered when investigating the origin of disorder in these structures. While a large number of different measurements of the carrier mobility show the temperature-dependent signature of acoustic phonon scattering, calculations overestimate the experimental values by an order of magnitude. Other explanations for the temperature dependence (optical phonons, polarons) do not fit the experimentally observed results. Recent theoretical calculations suggest that polar fluctuations on the timescale of electronic processes (picoseconds) are present in organic lead halide perovskites, and that although diffraction studies observe a phase transition to a cubic structure at 327 K, the electrons in the material experience a distorted tetragonal crystal [21]. Such polar domains could reduce the recombination rate, and would lead to disorder in the local structure. A Raman scattering study has revealed that these local polar fluctuations are not necessarily unique to organic perovskite hybrids, but are also present in CsPbBr<sub>3</sub> [22]. X-ray and neutron diffraction measure the time-averaged atomic positions within the unit cell of a crystalline phase. For materials with high levels of dynamic disorder, this can smear out the local atom-atom correlations that are short time lived ( $\sim$  picosecond) for lead halide perovskites, based on inelastic neutron scattering, simulations and other probes [16] [17]. Thus, these measurements complement the nearly instantaneous atom-atom correlations (10-



15 picoseconds) obtained from EXAFS, and by combining information on fast (EXAFS) and slow (diffraction) atom-atom correlations, we should be able to learn what are the characteristics of the dynamical disorder in lead halide perovskites. For example rapid ferroelectric fluctuations would increase the width of the pair distribution function in EXAFS and hence the correlated Debye-Waller factor  $\sigma^2$ . If large anharmonicity exist for the Pb and I atoms, with possibly some ion hopping [17] the distribution functions for the Pb-I and I-I pairs should show both an increased width and a large T-dependent asymmetry parameter called C3.[23]

This thesis also includes the investigation of local structure present in single-step precursor solutions of methylammonium lead iodide (MAPbI<sub>3</sub>) perovskite as a function of organic and inorganic precursor ratio, as well as with hydriodic acid (HI), using X-ray absorption spectroscopy. An excess of organic precursor as well as the use of HI as a processing additive has been shown to lead to the formation of smooth, continuous, pinhole free MAPbI<sub>3</sub> films, whereas films produced from precursor solutions containing molar equivalents of methylammonium iodide (MAI) and PbI<sub>2</sub> lead to the formation of a discontinuous, needle-like morphology. We now show that as the amount of excess MAI in the precursor solution is increased, the iodide coordination of iodoplumbate complexes present in solution increases. The use of HI results in a similar increase in iodide coordination. We therefore offer insight into how solution chemistry can be used to control MAPbI<sub>3</sub> thin film morphology by revealing a strong correlation between the lead coordination chemistry in precursor solutions and the surface coverage and morphology of the resulting MAPbI<sub>3</sub> film. More information can be found in CH.

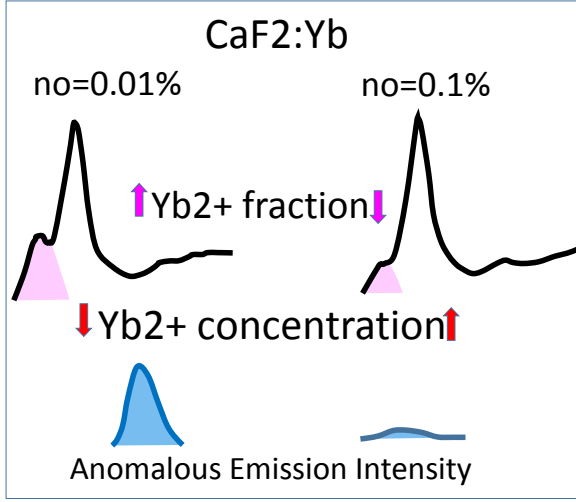


Figure 1.1: Diagram showing anomalous emission intensity is inversely related to total  $\text{Yb}^{2+}$  concentration.

3.

## 1.2 Calcium Fluorite

A fresh sample of Yb-doped  $\text{CaF}_2$  exhibits an anomalous redshifted luminescence after UV excitation, attributed to the relaxation of impurity trapped excitons (ITE) [24; 25; 26].  $\text{CaF}_2:\text{Yb}$  is the archetype system for this model, in which each  $\text{Yb}^{2+}$  ion is excited into a long lived (ms) exciton state. Upon de-excitation, the emission intensity should be proportional to the  $\text{Yb}^{2+}$  concentration [25], but that could not be checked when this model was first proposed. When substituting on a Ca site, Yb can be expected to have a valence of 2+ like the calcium atom. Due to the larger ionic radius of Yb compared to the Ca ion [7], a defect complex consisting of a smaller radius  $\text{Yb}^{3+}$  and interstitial fluorine can arise. Using the x-ray absorption near edge

structure (XANES) technique we determine the fractions of  $\text{Yb}^{2+}$  and  $\text{Yb}^{3+}$  for low Yb concentrations, 0.01% to 0.1%, and thus determine the net concentration of  $\text{Yb}^{2+}$ . A comparison with luminescence data shows that the intensity is not proportional to the  $\text{Yb}^{2+}$  concentration, and only a fraction of  $\text{Yb}^{2+}$  ions contributes to the anomalous luminescence. This is inconsistent with the ITE model and illustrates the importance of checking the dependence of the emission intensity on the  $\text{Yb}^{2+}$  concentration.

### 1.3 Lithium Niobate

Many dopants are incorporated into  $\text{LiNbO}_3$  (LNO) to modify the physical properties, particularly many optical properties [27; 28]. To understand these changes, the substitution site for the dopant must be known. Here we provide a detailed EXAFS study of the local environment about the metal (M) ion dopants Zinc, Indium, Erbium, and Hafnium in LNO, using crystals grown in both stoichiometric and congruent forms; the latter grows naturally with a slight excess of Nb and some Li vacancies. In primarily substitutes at the Li site in congruent material; Er also substitutes mostly on the Li site with a small fraction roughly 10 % on the Nb site - the substitution sites for Er do not appear to change much between stoichiometric and congruent LNO. For Hf, approximately half the dopant substitutes on Li and half on Nb. In all cases, self charge compensating schemes where a dopant resides on both sites are not consistent with the data. Some charge compensating defects are required, and can occupy several nearby sites in the crystal leading to many slightly different distributions, some of which may

be meta-stable. For each dopant, changes in the the M-O shell approximately follow the ionic radius of the dopant ion [7]; in addition the Nb neighbors about M on a Li site, are shifted away from the dopant, with large displacements for some dopants such as Er. Comparisons with other experiments and existing calculations are discussed [29; 30].

## Chapter 2

# X-ray absorption background

### 2.1 Theoretical

The x-ray absorption technique we employ focuses on exciting either the K edge or  $L_{III}$  edge of a certain material; in doing so a core electron is excited into the continuum. The wavefunction of this photoelectron back-scatters off of neighboring atoms and interferes with itself, in turn affecting the probability of ejection of a core electron. For simplicity this phenomenon is treated as a one electron theory. There are other concurrent phenomena to consider including: multi-electronic excitations, multi-path scattering, auger processes, atomic EXAFS, amplitude reduction, inelastic scattering, and pinhole effects.

Some of these can be minimized experimentally, like eliminating any pinholes by making a uniform layer of sample powder with small crystallites ( $< 5$  microns). Others effects like atomic EXAFS can be filtered out by removing a slowly oscillating

background, so as minimize signal at  $\sim 1 \text{ \AA}$  in real-space. Further, features like multi-electron excitations and monochromator glitches can be identified and removed using small-scale polynomial interpolation. The remaining phenomena are roughly modeled and included in simulating the EXAFS function,  $\chi(k)$ .

Using Fermi's golden rule, we can treat the probability of absorption as follows:

$$\mu_0 \propto | \langle \psi_f | H | \psi_i \rangle |^2 = A_0 \int |\Psi_f^\dagger \hat{\epsilon} \cdot \vec{r} \Psi_i|^2 \quad (2.1)$$

This equation can be applied in describing of absorption of an x-ray ejecting a core electron from an isolated atom, and is derived from the Fermi's golden rule and the dipole approximation of the Hamiltonian of a charged particle in an electromagnetic field. With this relation between absorption and electronic wavefunctions we can model the absorption of an ensemble of isolated atoms, like a gas. We would find a smooth absorption profile post-edge, where-as in materials with ordered lattice structures we see a oscillations in this post-edge structure. This is due to the complication of summing over all of final states, including the perturbed ones of the backscattered photoelectron. We now must consider the ordered environment around an atom in a lattice.

A similar approach is used except we now include an extra term to the final state:

$$|\Psi_f \rangle = |\Psi_f^0 \rangle + \Delta \Psi_f \rangle \quad (2.2)$$

With this new form, we can simplify the innerproduct (with the Hamiltonian)

and end up with two components: the isolated atom component, and the backscattering component. For absorption to be affected by a backscattering event, the ejected photoelectron must return to the original absorbing atom while still in its excited state, resulting in a coherent final state. Let us apply fermi's golden rule to our newly introduced  $\Psi_f$ .

$$\mu_0\alpha | \langle \psi_f^0 | H | \psi_i \rangle |^2 \left( 1 + \langle \psi_i | H | \Delta \psi_f \rangle \frac{\langle \psi_f^0 | H | \psi_i \rangle^*}{| \langle \psi_i | H | \psi_f^0 \rangle |^2} + \langle \Delta \psi_f | H | \psi_i \rangle \frac{\langle \psi_i | H | \psi_f^0 \rangle^*}{| \langle \psi_f^0 | H | \psi_i \rangle |^2} \right) \quad (2.3)$$

The above is factored to convey the separation between the absorption of a bare atom, and the affected portion from the interference in the final state. We can convey this more simply as so:

$$\mu = \mu_0(1 + \chi) \quad (2.4)$$

The modulation of absorption is from  $\chi(E)$  so we must derive an approximation for the interfering photoelectron wavelets. When an x-ray is absorbed, a photoelectron with wavenumber  $k$  is excited into the continuum. Employing the dipole approximation for the damped wavefunction of a photoelectron, our outgoing wavefunction takes the form:

$$(\hat{\epsilon} \cdot \hat{r})^2 \frac{e^{-ikr + i\delta_c(k)}}{kr} \quad (2.5)$$

where  $\delta_c(k)$  is the phase shift of the wavefunction from the original absorbing atom. There is a non-negligible probability of inelastic scattering of the photoelectron be-

fore reaching a neighbor. So if we want the wavefunction at a distance  $r=R$  from the absorbing atom, we are left with :

$$(\hat{\epsilon} \cdot \hat{r})^2 \frac{e^{-ikr+i\delta_c(k)}}{kr} e^{\frac{-r}{\lambda(k)}} \quad (2.6)$$

where  $R$  is the distance of an atomic shell, or backscattering atom. In the event of the photoelectron scattering off of a neighbor, we have a wavefunction propagating back to the host atom. We must include the complex backscattering factor,  $f(\pi, k)$ , from a neighboring atom, and weight it with  $k$ . Also we have to consider the phase shift in the wavefunction from the backscatterer as well so we get a wavefunction of the form:

$$(\hat{\epsilon} \cdot \hat{r})^2 \frac{e^{-ikr+i\delta_c(k)}}{kR} e^{\frac{-r}{\lambda(k)}} k |f(\pi, k)| \frac{e^{-ik(r-R)+i\delta_b(k)}}{kr} \quad (2.7)$$

Since we are interested in absorption, we can take the imaginary part of this expression and we have the modulation of the wavefunction (of one wavelet) due to a single backscattering neighbor in equation 2.8.

$$(\hat{\epsilon} \cdot \hat{r})^2 |f(\pi, k)| e^{\frac{-2r}{\lambda(k)}} \frac{\sin(2kr + 2\delta_c(k) + \delta_b)}{kr^2} \quad (2.8)$$

but we have been treating this neighbor as a point, so we simply include a symmetric pair-distribution function:

$$g(r) = \frac{1}{\sqrt{2\pi}\sigma} e^{\frac{-(r+R_i)^2}{2\sigma^2}} \quad (2.9)$$

where  $\sigma$  is the width of the symmetric pair distribution function and  $R_i$  is the centroid, physically corresponding to the distance of the atomic shell. Rewriting our  $\chi(k)$  equation



integrated over  $r$ ,

$$\int_0^\infty (\hat{\epsilon} \cdot \hat{r})^2 |f(\pi, k)| g(r) e^{\frac{-r}{\lambda(k)}} \frac{\sin(2kr + 2\delta_c(k) + \delta_b)}{kr^2} dr \quad (2.10)$$

we can employ an approximation, provided  $\frac{\sigma}{R_i} \ll 1$  and the potential is harmonic, to end with:

$$\chi(k) \approx (\hat{\epsilon} \cdot \hat{r})^2 |f(\pi, k)| e^{-2k^2\sigma^2} e^{\frac{-r}{\lambda(k)}} \frac{\sin(2kr + 2\delta_c(k) + \delta_b)}{kr^2} \quad (2.11)$$

Now we have the derivation for the modulation due to a single backscatterer with a gaussian distribution of pair distances. It follows that we can sum over wavelet contributions, taking into consideration an multi-electronic effect loss factor,  $S_0$ , and degeneracy of each atomic shell,  $N_i$ .

$$\chi(k) = \sum_i \frac{N_i S_0^2}{kr_i^2} f(\pi, k) e^{-2R_i/\lambda(k)} e^{-2\sigma^2 k^2} \sin(2kr_i + 2\phi_c + \phi_b) \quad (2.12)$$

The time-scale for decoherence of the ejected photoelectron is  $\sim 10^{-15}$  s, so EXAFS offers a snapshot of the radial pair-distribution function around the excited atom, as opposed to a longer time-averaged picture of the local structure. There is a bit of absorption modulation from each unique backscatter event,  $\chi(k)$ , so for  $\chi(k)$  we sum over each atomic shell and include the degeneracy,  $N_i$ , of the equivalent positions. The mean free-path term,  $e^{-2r_i/\lambda(k)}$ , is included to account for both the non-negligible probability of inelastic scattering and the termination of the core-hole lifetime. The oscillatory part of  $\chi(k)$ ,  $\frac{\sin(2kr_i + 2\phi_c + \phi_b)}{kr_i^2}$ , contains a few pieces of information. First, the

farther away the scattering shell, the faster the oscillation in  $\chi(k)$ . Second, the scaling factor from the EXAFS equation of  $1/k$  implies there is a bounded range for which the EXAFS signal,  $\chi(k)$ , is reasonable. Typically we start with weighting our data with a factor of  $k$  so as to stretch the  $k$ -range. If there is strong EXAFS signal at high  $k$ , the  $\chi$  function can be weighted by higher orders of  $k$ , like  $k^2$  or  $k^3$ . Third, the term  $\phi$  in the argument is determined by the atomic species of backscatterer, and is calculated for each element by FEFF [4]. The other part of the EXAFS equation that depends on species of neighbor is  $f(\pi, k)$ .

When we evaluate fits and compile results, we use a fourier transform of our simulated  $\chi(k)$  convolved with our well behaved pair-distribution function. Analyzing  $\chi(r)$  is easier for a wide audience, as the magnitude (or modulus) of our  $\chi(r)$  generally represents the existence of an atom at the peak of an envelope.

### 2.1.1 Generalized Pair-Distribution Function

The previously derived  $\chi(k)$  may not work in situations where a neighboring atom is in an anharmonic potential. This may be obvious in the data when we observe an experimental  $\chi(k)$  function that appears to stretch out at high  $k$  as temperature increases, leading to a skewed gaussian in our  $r$ -space data. Initially, the assumption of dissimilar pair-distribution functions was a major limitation in EXAFS fitting [31]. Let us revisit our previous approximation, and use a generalized  $g(r)$ . So going back to equation 2.7 and ignoring the polarization term, we have a  $\chi(k)$  that reduces to:

$$\frac{e^{i(2kR-\delta)}}{kR^2} e^{\frac{-R}{\lambda(k)}} |f(\pi, k)| \quad (2.13)$$

This allows us to simply write down the following generalized  $\chi(k)$  where we employ an unknown pair distribution function.

$$\chi(k) = \sum_i N_i S_0^2 |f(\pi, k)| \text{Im} \left[ \int_0^\infty \frac{g_i(r_i) e^{\frac{-2r_i}{\lambda}} e^{2ikr_i}}{kr_i^2} dr_i \right] \quad (2.14)$$

Using substitution of  $x = r - r_0$  and  $\tilde{f}(k) = f(k)e^{i\phi(k)}$  pulling a phase out of our effective backscattering amplitude, we can write the above integral as follows:

$$\chi(k) = \sum_i \frac{N_i S_0^2 |\tilde{f}(\pi, k)|}{kr_0^2} e^{-2r_0/\lambda} \text{Im} \left[ e^{i(2kr_0 + \phi(k))} \int_{-r_0}^\infty \frac{g(x) e^{\frac{-2x}{\lambda}} e^{2ikx}}{\left(1 + \frac{x}{r_0}\right)^2} dx \right] \quad (2.15)$$

We have gone down this more rigorous route to derive  $\chi(k)$  from an unknown pair-distribution, so let us focus only on the integral now. We can lump terms into a new PDF,  $G(x)$ , which is commonly used in literature [32].

Setting  $G(x) = \frac{g(x) e^{\frac{-2x}{\lambda}}}{\left(1 + \frac{x}{r_0}\right)^2}$  we can average over our unknown PDF and expand in terms of cumulants:

$$\int_{-r_0}^\infty G(x) e^{2ikx} dx = \langle e^{2ikx} \rangle = \sum_0^\infty \frac{(2ik)^n}{n!} = 1 + 2ik\langle x \rangle - 2k^2\langle x^2 \rangle - \frac{4}{3}ik^3\langle x^3 \rangle + \frac{2}{3}k^4\langle x^4 \rangle \quad (2.16)$$

This is a power expansion in terms of  $\langle x \rangle$ , where  $\langle x \rangle = \int G(x) x^n dx$ . This expansion converges for a small range of  $k$  [32], so we look to cumulant expansion with cumulants  $C_n$ :

$$\langle e^{\eta x} \rangle = e^{\sum_0^\infty \frac{\eta^n C_n}{n!}} \quad (2.17)$$

and when applied to our power series:

$$\sum_0^\infty \frac{C_n (2ik)^n}{n!} = \ln(\langle e^{2ikx} \rangle) = \ln\left(\sum_0^\infty \frac{(2ik)^n}{n!}\right) \quad (2.18)$$

Concerning ourselves with the first four orders, and assuming  $\langle x \rangle = 0$  at the center of the PDF, then we are left with the following cumulants:

$$C_1 = \langle x \rangle = 0$$

$$C_2 = \langle x^2 \rangle = \sigma^2$$

$$C_3 = \langle x^3 \rangle$$

$$C_4 = \langle x^4 \rangle - 3\langle x^2 \rangle^2$$

After going through the more rigorous route of an unknown distribution, we have the following equation for a single atomic shell:

$$\chi(k) = \frac{N_i S_0^2}{k r_i^2} F_B(k) e^{-2r_i/\lambda(k)} e^{-2\sigma^2 k^2 + \frac{2}{3} k^4 C_4} \times \sin\left(2k\left((r_i + \Delta r) - 2\sigma^2\left(\frac{1}{r_i} + \frac{1}{\lambda}\right)\right) - \frac{4}{3} C_3 k^3 + \phi(k)\right) \quad (2.19)$$

With this explicit formula, we can see how the expected accordion effect in k-space behaves. The phase factor  $\phi(k)$  is generally temperature independent and assume no  $C_3$  contribution in the argument of  $\sin()$ . Our zero-crossing at  $k \sim 10 \text{\AA}^{-1}$  implies  $2kR_{eff}$  is a multiple of  $\pi + C$ , where C is some constant offset. If we introduce a positive

$C_3$  and assume  $R_{eff}$  is a fixed centroid of the PDF, our zero-crossing can only happen at higher  $k$ . Also worth noting is that the apparent shift of the zero-crossing will be more exaggerated at high  $k$  values.

## 2.2 Experiment

To collect data with a strong enough signal, we need a brilliant x-ray source. We use the x-rays provided by the Stanford Synchrotron Radiation Lightsource (SSRL) which has a flux of  $2 \times 10^{12}$  photons/sec with a spot size of 4 x 18 mm unfocused; the slits are often set to be  $\sim 1 \times 7$  mm in our experiments. Typically, we use a double monochromator with silicon (220) crystals to select our energy. Energy resolution is important, as we are measuring fine oscillations in the absorption spectrum at high energies ( $\geq 5$ keV). Energy resolution of the monochromator is determined by the Bragg characteristics of the monochromator, beam divergence depending on vertical beam profile and sample distance, and selected energy. Si(220) crystals have a resolution of  $\frac{\Delta E}{E} \sim 0.590 \times 10^{-4}$ . We generally use an unfocused beam so our limit in resolution is dominated by beam spread; our approximate mean resolution is 1eV, which is sufficient for energy precision. Monochromators can exhibit “glitches” which occur when more than one set of lattice planes simultaneously satisfy the Bragg condition. These variations in the incident intensity show up in the EXAFS data when the sample is non-uniform [33] or when a significant fraction of higher harmonics is present.

To measure absorption we usually employ the ion chambers situated before

and after the beam hits the sample. These ion drift chambers work by measuring the current induced when the x-ray ionizes the detector gas ( $\text{N}_2$  or  $\text{Ar}$ ); the current is directly proportional to the number of photons absorbed in the detector gas.

The detection decreases slightly with increasing energy. In transmission we use identical detectors for  $I_0$  and  $I_1$ , for which this effect cancels out when taking  $\mu$  to be the log ratio of counts. Ignoring this introduces a negligible E dependence in sigma.

These currents are converted to counts, and our measured  $\mu$  is the log ratio of the counts before and after the sample. This works well if the atomic edge we are trying to probe has a strong signal, but in studying low concentration dopants, and thin films, we have to go beyond this technique for measuring absorption, and instead rely on fluorescence measurements.

As stated in the theoretical section, the photoelectron has a modulated probability as a function of energy of being ejected into the continuum. In turn, there is a modulated probability of the core-hole existing, which results in a modulated probability of a radiative recombination of that core-hole and another electron. This recombination leaves us with a fluorescence signal, which can be detected by a multi-element fluorescence detector. There are some parameters to consider when extracting  $\mu$  from fluorescence data, like the detector geometry, the self-absorption of the sample, and the overlapping of unwanted signal (other elements, x-ray scatter).

In most cases, the aforementioned obstacles are not present except for selecting the correct fluorescence signal. It is important to only include counts from the specific edge you are interested in, and this is done by observing changes in spectrum at 100eV

above and below the edge. If there are undesired dominant peaks present, it can be useful to use physical signal filtering techniques, i.e. taping different foils over detector window. The most frequently encountered undesired peak is from elastic x-ray scatter off of the sample, and to filter this out we make use of Soller slits. By using a Z-1 notch filter in conjunction with Soller slits we can maximize our signal which is the fluorescence of the desired edge in the sample.

Another complication with fluorescence EXAFS is that the sample itself can satisfy Bragg conditions, resulting in sharp Bragg peaks in the post-edge structure. Like the monochromator glitches mentioned above, we are left to use a function of our Real-Space X-ray Absorption Package (RSXAP) to interpolate the data without the Bragg spike. This does suffice, as glitches and Bragg peaks are no more than 3 data points long.

## 2.3 Analysis

The aim in our EXAFS analysis is to reduce the absorption data to an experimental  $\chi(k)$ , and fit the data with a sum of simulated  $\chi(k)$  functions that correspond to discrete atomic shells surrounding the host atom. To start, we de-glitch, normalize, and average absorption spectra in energy space. Then, we want to select a post-edge region that starts at 15eV above the edge, and extends to 500-1000eV above the edge. This region is fit to a sum of 5-10 splines which models the slowly varying background function; usually the spacing of the splines (the connections are known as “knots”) increases with

energy. Certain edges have special near-edge structure due to multi-electronic excitations, causing them to have a broad peak of enhanced absorption. It becomes necessary to fix a knot at a certain energy to assure the low-E region of the spline fit function is convex.

Once the the slowly oscillating background is subtracted, we are left with our experimental  $\chi(k)$  function, which we then weight with  $k$  to emphasize data in the region  $6 \text{ \AA}^{-1} < k < k_{max}$ . Now, it is common to fourier transform the data from reciprocal space (k-space) to real space. Doing so and looking at the modulus of the transform leaves us with an experimental radial pair distribution convoluted with the backscattering amplitude. Sometimes just using the modulus of the transform is misleading, as particular combinations of neighboring atoms lead to the destructive interference of the real part of the fourier transform of  $\chi(k)$ , denoted as  $\text{Re}\{\text{FFT}[k\chi(k)]\}$ . The only way to know this is by fitting the data.

For simulating scatter paths we employ FEFF7, which uses a muffin tin atomic potential to simulate effective scattering amplitudes. We start with atomic positions (lattice basis vectors) and a symmetry group, which is permuted into an input file of positions of all atoms in a radius of  $< 9 \text{ \AA}$  from the excited atom. We then generate normalized standards of each atomic shell so we build a set of theoretical  $\chi(k)$  to be used in a linear combination fit in r-space. FEFF7 also provides us with multi-scattering paths and estimates the amplitude of such signals. At a certain relative threshold we are compelled to include multi-scattering standards in our fits, and often it is necessary as our simple single backscatterer model does not fit the data well. Multiscatter paths



of importance include forward scattering, which are strongly enhanced when the photoelectron is scattered at an angle  $\theta \leq 15^\circ$ . Depending on energy and atomic species, this event is analogous to a lensing and in turn an enhancement of the scattered wavefunction. Forward scattering paths are of significance when probing structural phase transitions, as the amplitude of such a scatter path is quickly killed when atoms are snapped out of their nearly co-linear arrangement.

Our fitting is done using RSFIT [23], the complimentary software package to RSXAP. For each standard we generally vary three variables from the EXAFS function:  $\sigma$ ,  $r$ ,  $N$ . First, we aim to include as many reasonable constraints as our fits include many parameters; so fixing  $N$  to the degeneracy of each atomic shell is common practice. This is an important first step, as there exists a strong correlation between  $\sigma$  and  $N$ , and we are interested in obtaining quantities for  $\sigma$  as a function of temperature. With our fits, we are limited to a certain number of free parameters as we want to have a reasonable number of degrees of freedom. Degrees of freedom in our fits are defined as follows [34]:

$$DoF = \frac{2}{\pi} \Delta r \Delta k + 2 - (3 \times p + 1 - c) \quad (2.20)$$

Where  $p$  is the number for of standards (or peaks), and  $c$  is the number of constraints. The first term is the derived number of independent data points using Stern's criteria [34]. When a local structure is complicated and degeneracies are broken, it becomes imperative to find other constraints like constraining  $\sigma$  of two similar neighbors to each other. It is easy but meaningless to fit data perfectly with an excess of free parameters, so care must be taken when including multiscatter paths.

When going through fit iterations, we initially look for a fit with  $R \leq 15\%$ ,  $1 \leq DoF$ ,  $.035 \leq \sigma \leq .15$ ,  $|\Delta r| \leq 0.15$ . If the fit continually hits the limit we re-evaluate starting values; for example, when using a standard to fit a dopant bond-length, a pair distance shift can occasionally be  $\geq 0.15\text{\AA}$  in magnitude. There are main features that we qualitatively evaluate, like how the fit follows the data at certain sharp dips in the envelope and phase. These features aid us in finding the unique fit that simulates the interference pattern around our excited atom.

## Chapter 3

# Organic Lead Halide Perovskites: Coordination, and Vibration

Section 3.1 in the following chapter is an adapted version of the following paper [35]:

A. Sharenko, C. MacKeen, L. Jewell, F. Bridges, M. Toney, “Evolution of Iodoplumbate Complexes in Methylammonium Lead Iodide Perovskite Precursor Solutions”, *Chem. Mater.*, **29** (3), 2017

### 3.1 Evolution of Iodoplumbate Complexes in Methylammonium Lead

Here we investigate the local structure present in single-step precursor solutions of methylammonium lead iodide ( $\text{MAPbI}_3$ ) perovskite as a function of organic and inorganic precursor ratio, as well as with hydriodic acid (HI), using X-ray absorption

spectroscopy. An excess of organic precursor as well as the use of HI as a processing additive has been shown to lead to the formation of smooth, continuous, pinhole free MAPbI<sub>3</sub> films, whereas films produced from precursor solutions containing molar equivalents of methylammonium iodide (MAI) and PbI<sub>2</sub> lead to the formation of a discontinuous, needlelike morphology. We now show that as the amount of excess MAI in the precursor solution is increased, the iodide coordination of iodoplumbate complexes present in solution increases. The use of HI results in a similar increase in iodide coordination. We therefore offer insight into how solution chemistry can be used to control MAPbI<sub>3</sub> thin film morphology by revealing a strong correlation between the lead coordination chemistry in precursor solutions and the surface coverage and morphology of the resulting MAPbI<sub>3</sub> film.

### 3.1.1 Introduction

Lead halide perovskites have attracted an immense amount of attention over the past several years because of the rapid ascent of their photovoltaic efficiency [36] [37] To date, solution-processed lead halide perovskite photovoltaic devices have been reported with certified power conversion efficiencies exceeding 20 % [38] Recent advances are in large part due to the development of processing techniques that produce smooth, continuous films necessary for the active layer in a high-efficiency photovoltaic device. Forming such a smooth, continuous film using a singlestep solution processing protocol requires careful control of the chemistry of precursor solutions and/or the film deposition conditions [39] [40] Specifically, it is known that spin-casting a solution containing molar

equivalents of methylammonium iodide (MAI) and  $\text{PbI}_2$  fails to produce a continuous film and instead produces a discontinuous, needlelike morphology that produces shorts and a relatively low power conversion efficiency upon incorporation into a photovoltaic device. A common workaround is to cast films from solutions containing a molar excess of MAI, which produces a more continuous, smoother  $\text{MAPbI}_3$  film [41] [42]

A disadvantage of this methodology is that the excess MAI must then be removed from the film via thermal decomposition, requiring higher temperature and/or longer annealing protocols that can lead to grain coarsening and film roughening [43] An alternative method for producing smooth, continuous lead halide perovskite films with a singlestep protocol is to incorporate a small amount of hydriodic acid (HI) into the casting solution [44] HI has therefore been used as an additive for the fabrication of high-efficiency photovoltaic devices [45] [46] [47] Lead halide perovskite precursor solutions containing both the inorganic and organic precursor have been described as soft coordination networks [42] or sol-gels [48]. Stamplecoskie et al. suggested that  $\text{PbI}_2$  and the higher-order iodoplumbate coordination complexes  $\text{PbI}_3^-$   $\text{PbI}_3^{--}$  and  $\text{PbI}_4^{2--}$  exist in equilibrium in solutions where the iodide concentration exceeds the lead concentration by more than an order of magnitude [49] Changes in the absorption band edge of precursor solutions as a function of precursor molar ratio have thus been qualitatively explained in terms of relative changes in the populations of iodoplumbate coordination complexes that are present in solution [42] The presence of these complexes in perovskite precursor solutions and their exact structure and relationship to specific precursor chemistries, however, have not been directly verified or quantified and been only

indirectly inferred, nor, to the best of our knowledge, has any experimental evidence been presented to explain what role HI serves in precursor solutions. Herein, we use X-ray absorption spectroscopy of the Pb L-III edge to probe the local structure of the Pb ions in precursor solutions as a function of the precursor molar ratio and the presence of HI to aid in the development of a mechanistic understanding of how solution chemistry can be tuned to produce the smooth, continuous films required for the fabrication of efficient photovoltaic devices.

The remaining portion of this subsection is a summary of background information presented in Sec. 2.1. Extended X-ray absorption fine structure (EXAFS) refers to the oscillatory region of an X-ray absorption spectrum beginning 30 eV above an absorption edge. This oscillatory structure, denoted as  $\chi$ , arises from the backscattering of photoelectrons from various shells of neighboring atoms and can be expressed in terms of total absorption,  $\mu$ , for the edge of interest and average absorption above the edge  $\mu_0$ :

$$\chi(E) = \frac{\mu(E) - \mu_0(E)}{\mu_0(E)} \quad (3.1)$$

The extracted  $\chi(E)$  data are then converted from energy to wave vector or k-space. From perturbation theory,  $\chi(k)$  is a sum of waves of the following form: [50]

$$k\chi(k) = \sum_i \frac{N_i S_0 F(k, r_i) e^{-2\sigma_i^2 k^2}}{r_i^2} \sin[2kr_i + \phi_i(k, r_i)] \quad (3.2)$$

where  $k$  is the photoelectron wave vector,  $N$  is the number of neighbors (coordination

number),  $S_0^2$  is the amplitude reduction factor (equal to 1.0 here),  $F(k,r)$  is the backscattering amplitude,  $\phi(k,r)$  is the total phase shift (absorbing and backscattering), and  $\sigma$  is the width of the pair distribution function. Waves at different  $r$  add constructively or destructively, leading to a complex function in  $k$ -space. A Fourier transform (FT) of  $k\chi(k)$  into real space ( $r$ -space) then produces peaks corresponding to the distances from the absorbing atom to different neighbor atoms. The phase term  $\phi(k,r)$  can be approximately written as  $-2k\alpha + \Phi(k)$ ; when combined with the  $2kr$  term, the effective distance on an EXAFS plot is  $r - \alpha$ , where  $\alpha$  is the phase shift of approximately 0.3 — 0.5 Å. As a consequence of the phase shift, the peaks on an EXAFS plot are therefore shifted to shorter distances compared to actual atomic spacings. By fitting the data using eq 2 (the EXAFS equation), local structure information about the absorbing atom can be extracted up to approximately 4 — 5 Å, including the distance to neighboring (backscattering) atoms, their chemical identity, and the coordination number [51] In this study, MAPbI<sub>3</sub> precursor solutions in dimethylformamide (DMF) with different PbI<sub>2</sub>:MAI molar ratios (1:1, 1:1.5, and 1:3) as well as 1:1 PbI<sub>2</sub>/MAI precursor solutions with different amounts of HI and a solution of PbI<sub>2</sub> without MAI are investigated via EXAFS. Data were acquired at approximately 5 K using a helium cryostat on solutions that were flash-frozen in liquid nitrogen to prevent hydrogen gas evolution during X-ray irradiation, which complicates data collection and can introduce measurement artifacts [52] Additionally, sample cooling is recommended for samples containing soft metals to prevent EXAFS signal attenuation due to thermal effects [53] Sample cooling thus leads to higher EXAFS amplitudes at high wave vectors and hence facilitates the

interpretation of EXAFS.

### 3.1.2 Sample Preparation

All solution preparation took place in a nitrogen filled glove box. The following chemicals were used as received: Sigma-Aldrich lead(II) iodide (99.999%), Dyesol methylammonium iodide, Sigma-Aldrich Hydriodic acid (HI) (57 wt.%), and Sigma-Aldrich N,N-Dimethylformamide (99.8%, Extra Dry, AcroSeal). The  $\text{PbI}_2$ :MAI solutions were prepared at approximately 1 M concentration with respect to  $\text{PbI}_2$ . The  $\text{PbI}_2$  solution prepared without MAI was made with a concentration of approximately 0.4 M due to solubility limitations. HI was added to 1:1  $\text{PbI}_2$ :MAI solutions after solutions were stirred on a 70 C hotplate for several hours. HI concentrations were chosen to approximate concentrations previously reported in the literature [44] [45] [46] [47]

### 3.1.3 Data Acquisition

Data were acquired at the Stanford Synchrotron Radiation Lightsource on beam line 4-1 at approximately 5 K using a helium cryostat. Solutions were flash frozen in liquid nitrogen before placing in cryostat. Previous work has shown that such flash freezing results in local arrangements comparable to those found in room temperature solutions and results in very small changes to bond lengths[54] [55] A Lytle detector was used to acquire fluorescence signal, which is the signal that has been analyzed and presented herein. Nitrogen filled ion gauges were used to monitor signal before and after transmission through the sample. A small portion of the beam passed through a Pb



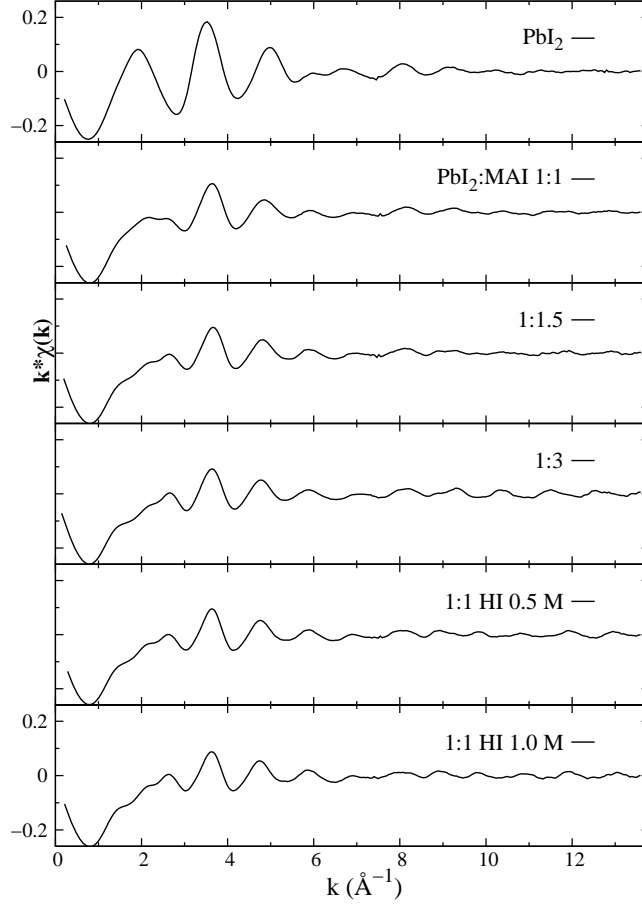


Figure 3.1: k-space data of the measured samples. Note that the trace for  $\text{PbI}_2$  (top) is multiplied by 0.5, to be on the same scale as the other samples.

metal foil in order to serve as an energy standard.

Each sample was measured five times consecutively. A Si (220) double crystal monochromator was used with 2 mm slits leading to an energy resolution of 5 eV (balancing the trade-off between a slight damping of the EXAFS oscillations at low  $k$  and increased signal for larger slits).

### 3.1.4 EXAFS Data Reduction and Fitting

First, a pre-edge background subtraction was carried out to remove contributions from other atoms and edges and isolate the contribution for the edge of interest—here the Pb L<sub>III</sub> edge. Then, a slowly varying average absorption above the edge,  $\mu_0$ , was removed by fitting to a spline function starting  $\sim 30$  eV above the absorption edge. Next, the extracted absorption oscillations  $\chi(E)$  (see Eq. 3.1 in the main text) were converted to k-space (Figure 3.1), and then Fourier transformed from k-space to real-space using a k-window from 4-13.5  $\text{\AA}^{-1}$  with a window rounding of 0.2  $\text{\AA}^{-1}$ . To fit the real-space data, we generated a series of theoretical standards ( $k^*\chi(k)$ ) for various atom pairs, e.g. Pb-I, Pb-Pb and Pb-O, at appropriate distances using FEFF7 [56] including standards derived from PbI<sub>2</sub>, PbI<sub>2</sub>-DMF [1] PbO, and PbO<sub>2</sub> crystal information files (CIFs). Of these, Pb-I components from the PbI<sub>2</sub>-DMF CIF were used for fitting. When fitting data other than the PbI<sub>2</sub> sample, we used a range of 1.9-4.3  $\text{\AA}$ , as there were no significant peaks below 3  $\text{\AA}$ . We explored the possibility of Pb-N and Pb-C components in the data but these were found to be insignificant via the Hamilton F-test [57]. The PbI<sub>2</sub>-DMF CIF file generated five unique non-degenerate Pb-I scattering paths ranging from 3.0-3.4  $\text{\AA}$ , but path lengths differing by less than 0.11  $\text{\AA}$  cannot be resolved in EXAFS and were therefore combined. We were left with three components to fit the region from 3.0-3.4  $\text{\AA}$ , and generally found the two components under 3.3  $\text{\AA}$  to be dominant.

When fitting the PbI<sub>2</sub> data we found there is a large low-r contribution from

a Pb-O scattering path, so we fit down to 1.7 Å instead of 1.9 Å. The PbI<sub>2</sub>-DMF Pb-O component was used in the initial fit, which resulted in an increase in bond length of the Pb-O peak of 0.17 Å relative to 2.44 Å. We therefore modified the standard to have a longer bond length and found no significant change in parameters or quality of fit. In contrast to the other samples the PbI<sub>2</sub> data could be fit with just one Pb-I component; if two Pb-I components were used, the second component shifted significantly to lower  $r$  and the two peaks were too close together to be resolved using the experimental  $k$ -range [50] Thus a two Pb-I component fit was not justified for this sample.

### 3.1.5 Results and Discussion

The data were fit in  $r$ -space using a sum of theoretical pair functions calculated from a PbI<sub>2</sub>-DMF crystal structure [1] using FEFF7 [56] These pair functions [Pb—O, Pb—I(1), Pb—I(2), and Pb—I(3)] are based on the atomic spacings within the crystal structure, which serve as starting points for the fits. For each pair, the distribution of distances is a Gaussian of width  $\sigma$  and amplitude  $N$ . The disorder for various shells of atoms is inferred from  $\sigma^2$ , the correlated Debye-Waller factor, with disorder increasing with the value of  $\sigma^2$ . The left side of Figure 1 displays the  $r$ -space EXAFS data of each sample and the fit, while the right side displays the individual Pb—I and/or Pb—O components. The PbI<sub>2</sub> plot is distinctly different from the rest of the data in that it exhibits a large peak at approximately 2.2 Å. This peak corresponds to a Pb—O bond, consistent with the knowledge that DMF coordinates with Pb<sup>2+</sup> ions in solution via the formation of Pb—O bonds [58] The PbI<sub>2</sub> data additionally exhibit a large, broad peak

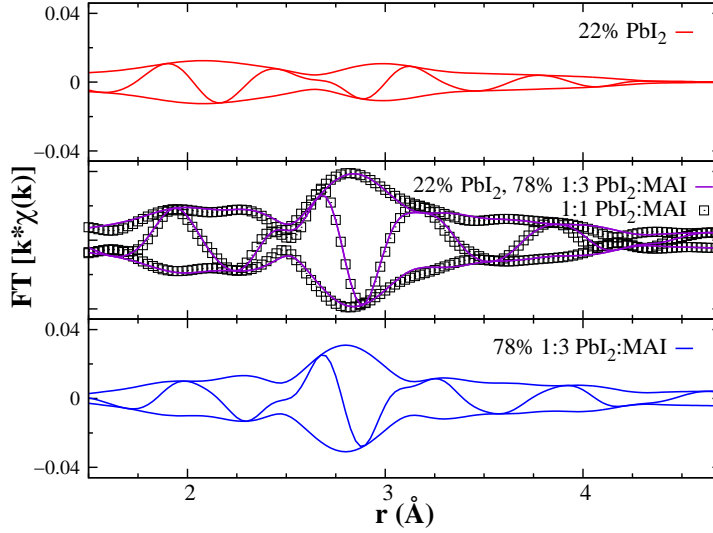


Figure 3.2: In this and subsequent r-space plots the fast oscillation is the real part  $Re$  of the FT while the envelop function is  $\sqrt{Re^2 + Im^2}$  where  $Im$  is the imaginary part of the FT. Linear combination fit (purple) of the 1:1 PbI<sub>2</sub>:MAI real space extended x-ray absorption fine structure data (open squares). The amplitude of the PbI<sub>2</sub> (red) and 1:3 PbI<sub>2</sub>:MAI (blue) data has been rescaled to 22% and 78% of their respective full amplitudes in order to aid comparison between the standards (red and blue curves) used to produce the linear combination fit (purple curve).

at approximately 3 Å that we have fit using a single Pb—I component.

In contrast, the data from solutions containing PbI<sub>2</sub> and MAI required three Pb—I components to adequately fit the data. As illustrated in 3.5, the first two Pb—I components for the samples with HI are very well ordered with small  $\sigma^2$  values. They dominate the r-space data, and the interference between these two components produces the dip at 2.85 Å that is not observed in the other samples.

The Pb—I(3) component of these samples, however, is slightly broader and less well-defined. For the samples without HI, the Pb—I(2) and Pb—I(3) components generally become increasingly disordered as the concentration of MAI increases from 1 to 3 M, with the Pb—I(2) component of the 1:3 PbI<sub>2</sub>/ MAI sample exhibiting significantly more disorder than any component in any of the samples.

Given the 10–15 % systemic error for coordination numbers from EXAFS fits as a result of correlations between N and  $\sigma$  [50] Pb ions total iodide coordination generally increases with an increase in MAI concentration and with the use of HI. Specifically, the total iodide coordination number increases from the PbI<sub>2</sub> (no MAI) sample to the 1:1 PbI<sub>2</sub>/MAI sample and then again to the 1:1.5 PbI<sub>2</sub>/MAI sample. The coordination number then remains constant within experimental error for the 1:1.5 and 1:3 PbI<sub>2</sub>/MAI samples. The iodide coordination number is largest, however, for the samples incorporating HI. The use of HI thus increases iodide coordination without introducing significantly more structural disorder in contrast to the use of excess MAI that increases both coordination number and structural disorder.

In general, the measured Pb—I(n) distances group into three rather distinct

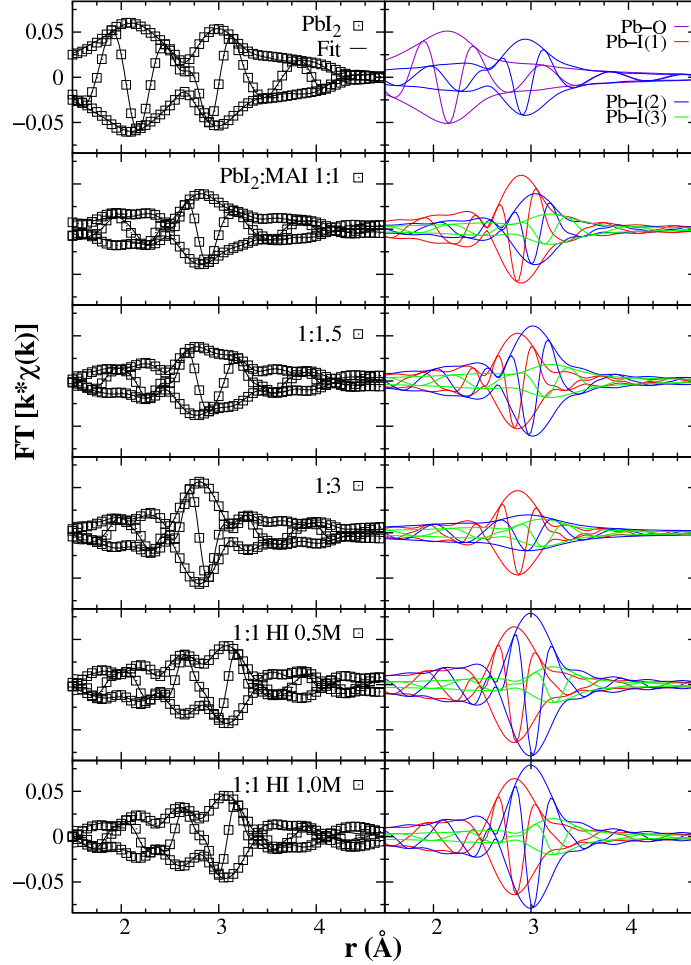


Figure 3.3: Fourier transform of eq 2 (i.e., EXAFS equation),  $FT [k\chi(k)]$ , vs  $r$ -space distance from the absorbing Pb atom ( $r$ ). Both the magnitude (outer envelope) and the real part (inner curves) of the Fourier transform are shown for the data. The left column shows the extended X-ray absorption fine structure (EXAFS)  $r$ -space data for six frozen single-step  $MAPbI_3$  precursor solutions with corresponding fits:  $PbI_2$ , 1:1  $PbI_2$ :MAI, 1:1.5  $PbI_2$ :MAI, 1:3  $PbI_2$ :MAI, 1:1  $PbI_2$ :MAI with 0.5 M HI, and 1:1  $PbI_2$ :MAI with 1.0 M HI (from top to bottom, respectively). The right column shows the individual components used in the fits for each sample.

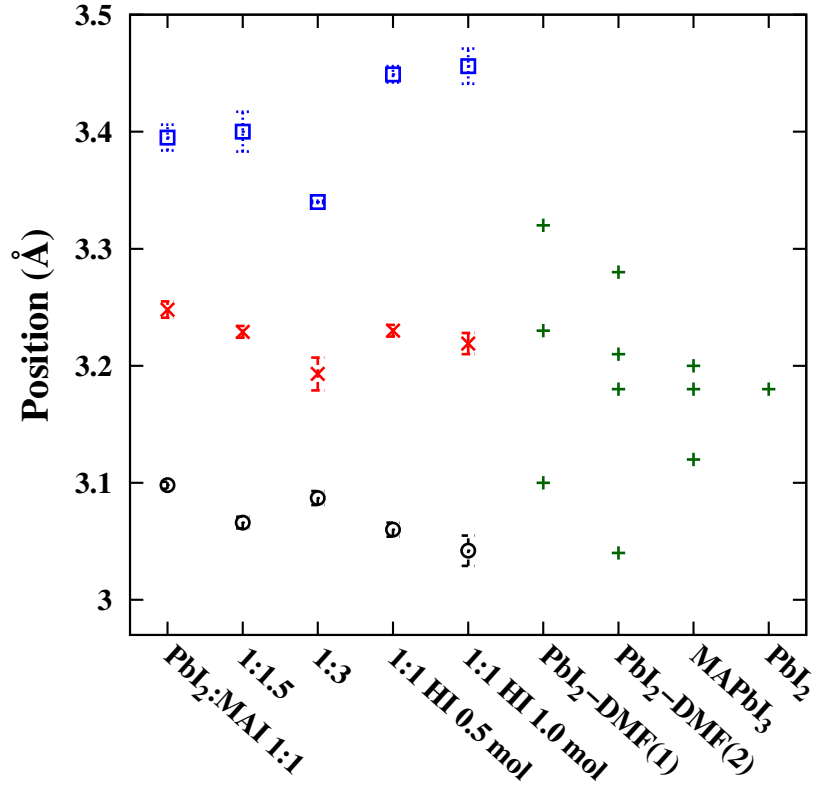


Figure 3.4: Pb-I bond lengths from our experimental data (black, red and blue) and selected literature values of compounds relevant for MAPbI<sub>3</sub> fabrication (green). Note that our data most closely resembles PbI<sub>2</sub>-DMF(1) [1] and PbI<sub>2</sub>-DMF(2) [2] albeit with longer terminal Pb-I bonds, especially in the samples containing HI.

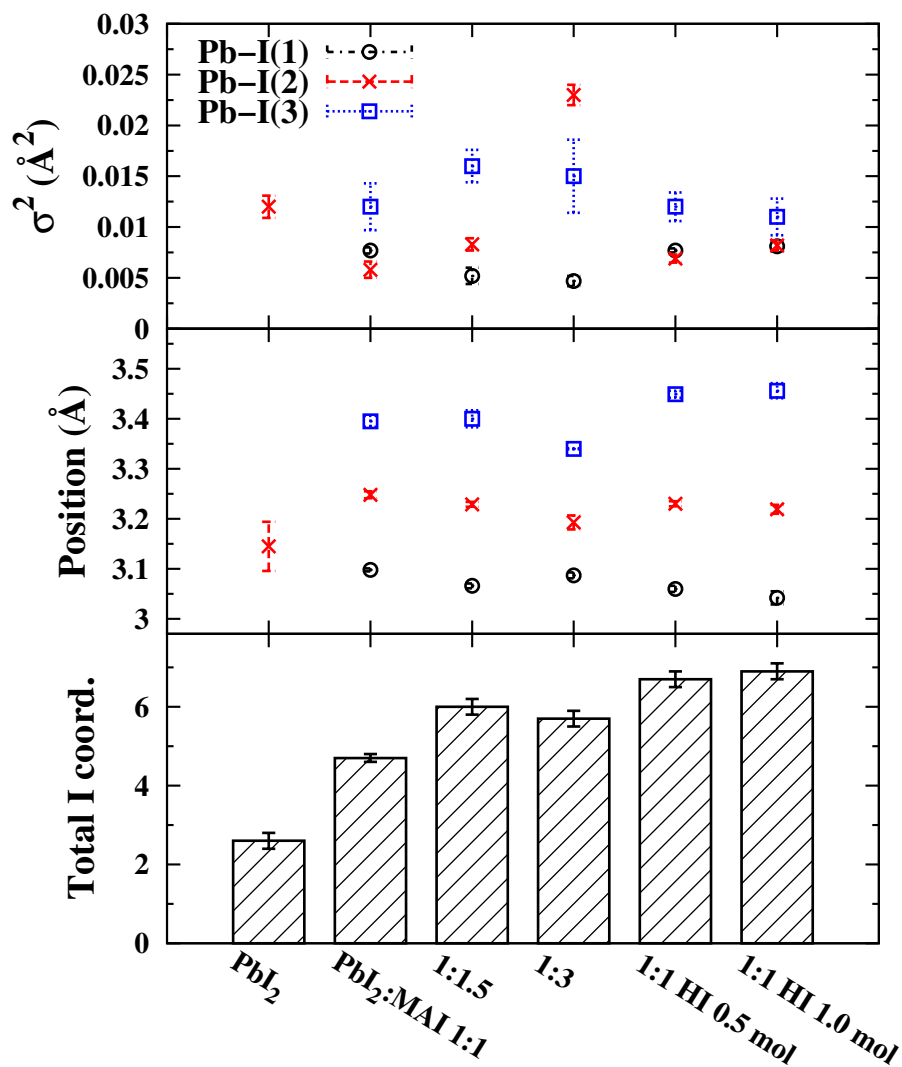


Figure 3.5: Real-space extended X-ray absorption fine structure (EXAFS) fit parameters extracted from Figure 1. The top panel plots the correlated Debye–Waller factor ( $\sigma^2$ ), the middle panel the Pb—I components positions from the absorbing Pb atom, and the bottom panel the total iodide coordination number of the Pb atoms in solution. Note that disorder increases as the value of  $\sigma^2$  increases and the Pb atoms in both PbI<sub>2</sub> and MAPbI<sub>3</sub> exhibit octahedral iodide coordination (PbI<sub>6</sub>).



spacings:  $\sim 3.1 \text{ \AA}$ ,  $\sim 3.2 - 3.25 \text{ \AA}$ , and  $\sim 3 \text{ \AA}$  [39] (see Fig. 3.5). Some insight into the possible origin of these spacings can be obtained by reference to the Pb—I bond lengths in  $\text{PbI}_2$ —DMF crystalline complexes [19,22,23] where extended octahedral Pb—I fragments are observed. These complexes structures have been determined with X-ray diffraction to understand their function as intermediate phases in the fabrication of  $\text{MAPbI}_3$  films [2] [59]. Our data are similar to data for these complexes in that both sets of data can be grouped into three distinct spacing regimes with comparable distances (Fig. 3.5). This is in contrast to the Pb—I bond lengths in  $\text{PbI}_2$ , which has only a single spacing, and tetragonal  $\text{MAPbI}_3$ , which has three spacings but lacks a spacing comparable to the Pb—I(3) spacing measured for our data. On the basis of these comparisons, we speculate that the iodoplumbate complexes that we observe in the perovskite precursor solutions are most similar to the extended octahedral Pb—I fragments in previously reported  $\text{PbI}_2$ —DMF crystalline compounds rather than to  $\text{PbI}_2$  or  $\text{MAPbI}_3$ , albeit with longer terminal Pb—I bonds. Furthermore, the samples with HI exhibit nearly identical pair distances for each Pb—I component. Their Pb—I(1) component is slightly shorter and their Pb—I(3) component slightly longer compared to those of the samples without HI, suggesting the use of HI leads to a slightly different complex compared to the use of excess MAI. There is also likely a very small Pb—O contribution for the 1:1  $\text{PbI}_2$ /MAI sample near  $2 \text{ \AA}$ , but multishell fits including a Pb—O component are not significant using the Hamilton F-test (discussed further below) [57].

We now present the X-ray absorption near edge structure (XANES) data of

the measured samples (Fig. 3.6). As XANES is a probe of the local chemical bonding environment of an absorbing atom, it can be used to provide further structural insight complementary to EXAFS. The  $\text{PbI}_2$  XANES data exhibit large peaks at 13050 and 13082 eV. The samples containing both  $\text{PbI}_2$  and MAI exhibit significantly less intense peaks at approximately 13061 and 13085 eV similar to simulated XANES spectra of higher-order iodoplumbate complexes [60]. The 1:1  $\text{PbI}_2$ :MAI data are unique in that its peak at 13061 eV is noticeably less intense than the spectra from the other samples containing both  $\text{PbI}_2$  and MAI, and it exhibits a large shoulder at approximately 13052 eV not present in any of the other spectra.

The XANES data additionally exhibit an isosbestic point at approximately 13056 eV. As the higher-order iodoplumbate complexes exhibit extremely similar XANES spectra that greatly differ from the XANES spectrum of  $\text{PbI}_2$ , [60] and as X-ray spectroscopy data are a weighted average of the coordination environment of all absorbing atoms in solution, the presence of an isosbestic point is consistent with spectra with contributions from both Pb ions with  $\text{PbI}_2$ -like coordination and Pb ions present in higher-order iodoplumbate complexes, the relative proportion of each shifting as a function of the relative MAI or HI concentration. We have exploited this observation to improve our understanding of the unique XANES spectra of the 1:1  $\text{PbI}_2$ /MAI sample by performing a linear combination fit of its real-space EXAFS spectra using the  $\text{PbI}_2$  and 1:3  $\text{PbI}_2$ /MAI samples as standards (??). The 1:1  $\text{PbI}_2$ /MAI EXAFS data can be modeled using approximately 22%  $\text{PbI}_2$  and 78% 1:3  $\text{PbI}_2$ /MAI. When we then use these same weightings in corresponding sums of the XANES data to reconstruct the 1:1

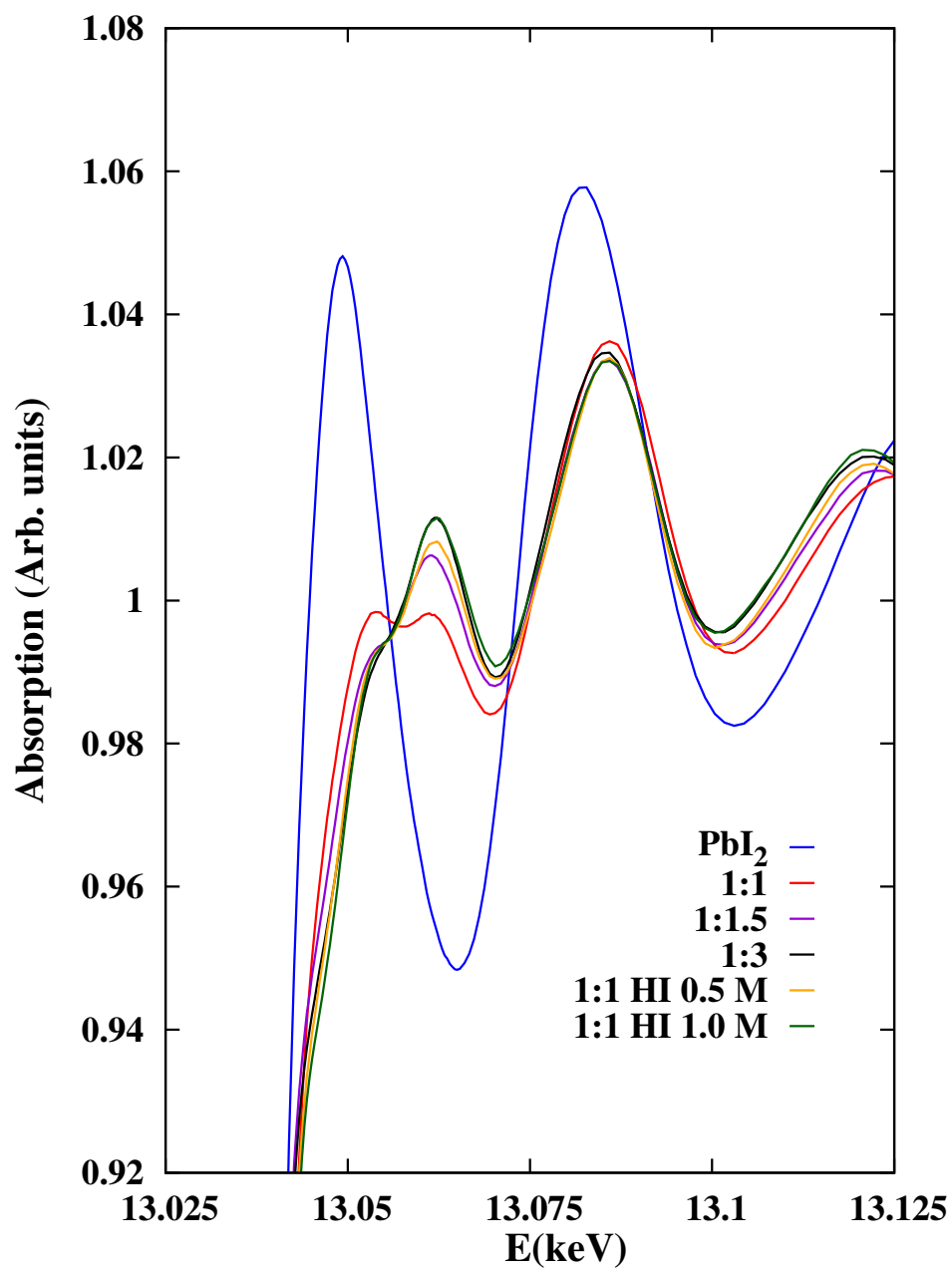


Figure 3.6: Pb L-III edge X-ray absorption near edge structure (XANES) spectra of the measured samples. The legend refers to the  $\text{PbI}_2$ :MAI molar ratio with the  $\text{PbI}_2$  sample not containing any MAI.

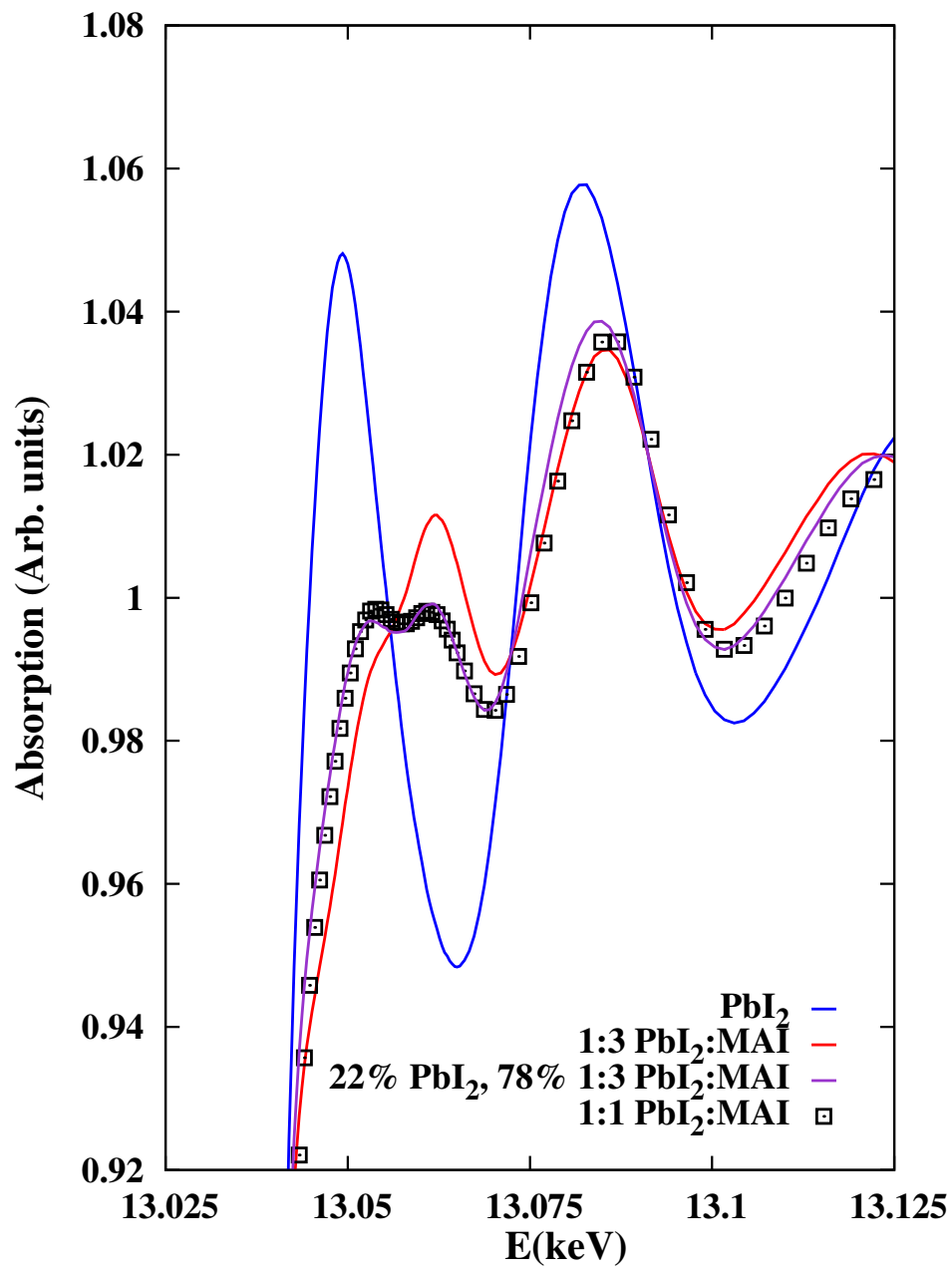


Figure 3.7: Linear combination fit of the 1:1  $\text{PbI}_2$ :MAI X-ray absorption near edge structure (XANES) data.

PbI<sub>2</sub>/MAI XANES data, we find this reconstruction matches the 1:1 PbI<sub>2</sub>/MAI XANES data extremely well (Figure 4). This linear combination fitting then suggests that the local chemical bonding environment of the 1:1 PbI<sub>2</sub>/MAI sample likely does have a small Pb—O component similar to that of the PbI<sub>2</sub> sample. This similarity is likely due to the presence of some remaining PbI<sub>2</sub>—DMF coordination in the 1:1 PbI<sub>2</sub>/MAI sample. The difficulty in obtaining a fit with a Pb—O component included for the 1:1 PbI<sub>2</sub>/MAI EXAFS data arises because the Pb—O peak in this sample is small and does not significantly contribute to its overall amplitude; therefore, the quality of the fit only slightly decreases when this peak is removed. In the simpler, two-component linear combination fit, the ratio of Pb—O to Pb—I is fixed in the PbI<sub>2</sub> data, and the fit is slightly better in the 1:1 PbI<sub>2</sub>/MAI linear combination data near 2 Å (??) compared to the EXAFS data fit using the theoretical pair functions (Figure 1). The very good fit of the reconstructed XANES data relative to the experimental XANES data using the weighting from the EXAFS linear combination fitting therefore indicates that a small amount of Pb—O coordination is present in the 1:1 sample but not for higher concentrations of MAI.

The presented EXAFS data then reveal that DMF coordinates to PbI<sub>2</sub> through the formation of Pb—O bonds but that as MAI is added to the solution, I<sup>−−</sup> ions displace DMF molecules to form higher-order iodoplumbate complexes. In general, the total iodide coordination number and structural disorder of these complexes increase with an increase in MAI concentration. The presented XANES data and the associated linear combination fitting additionally suggest that excess MAI or HI must be added

to solutions to fully displace coordinated DMF molecules as the 1:1  $\text{PbI}_2/\text{MAI}$  XANES data could be reconstructed with a significant contribution from the  $\text{PbI}_2$  XANES data, which EXAFS revealed to encompass significant Pb–DMF coordination. EXAFS data also revealed that the use of HI both increases the total iodide coordination number with little decrease in structural order and slightly alters the structure of iodoplumbate complexes in solution by shortening the Pb—I(1) component and expanding the Pb—I(3) component compared to those seen with the use of a molar excess of MAI. The complexes formed via the use of HI exhibited higher iodide coordination numbers compared to the use of equivalent concentrations of MAI, which may just be the result of the more efficient and complete dissociation of HI compared to that of MAI, thus resulting in a higher concentration of  $\text{I}^-$  ions at similar HI and MAI concentrations. On the basis of comparisons of Pb—I spacings, it appears the iodoplumbate complexes present in single-step  $\text{MAPbI}_3$  precursor solutions are most similar to known isolated intermediate phases produced during the synthesis of  $\text{MAPbI}_3$  rather than to  $\text{PbI}_2$  or  $\text{MAPbI}_3$ , but in the case of the solutions containing HI or excess MAI without coordinated solvent molecules.

Having identified the presence of higher-order iodoplumbate complexes in  $\text{MAPbI}_3$  precursor solutions as the result of the use of excess MAI or HI, we are able to offer some mechanistic insight into how these processing conditions may affect film formation. The presence of coordinated solvent in 1:1  $\text{PbI}_2/\text{MAI}$  solutions likely leads to the needlelike, discontinuous film morphology these films produce as this morphology is similar to that of the  $\text{PbI}_2$ –DMF crystals precipitated from supersaturated  $\text{PbI}_2/\text{MAI}$  solutions [48]

The improved morphology associated with use of excess MAI or HI is thus likely in part the result of the elimination of  $\text{PbI}_2$ -DMF coordination. Additionally, the higher-order iodoplumbate complexes these conditions generate in solution have been shown to be important to proposed solid state transformation pathways associated with smooth, continuous perovskite films [59] [61] The increased solubility associated with higher-order iodoplumbate complexes will also change the kinetics of film formation during deposition, which has proven to be a generally useful strategy for fabricating smooth, continuous perovskite films [62] [63] [64] The specific chemical complexes present in solution also directly affect the progression of phases precipitated from solution as described by Ostwalds Rule of Stages [65] However, because of the limitations of our data, specifically the low signal-to-noise ratio and overlapping multiple scattering features at larger real spacings, we cannot comment on various hypotheses about the role nanoparticles present in solution may play in film formation [42] [66]. Interestingly, the slightly altered iodoplumbate structure generated in solution as a result of the use of HI compared to excess MAI may in part explain recent observations that HI stabilizes the cubic polymorph of  $\text{MAPbI}_3$  at room temperature [67].

### 3.1.6 Conclusions

In summary, we have used Pb  $L_{\text{III}}$  edge EXAFS and XANES data of single-step  $\text{MAPbI}_3$  precursor solutions to reveal the lead coordination environment as a function of precursor solution chemistry. It was found that as excess MAI is added to solutions  $\text{I}^{--}$  ions displace coordinated DMF molecules to form higher-order iodoplumbate complexes,

i.e.,  $\text{PbI}_4^{2-}$ ,  $\text{PbI}_5^{3-}$ , and  $\text{PbI}_6^{4-}$ . Solutions containing molar equivalents of  $\text{PbI}_2$  and MAI exhibited significant DMF coordination, perhaps explaining the extremely discontinuous, needlelike film morphology these films produce. When  $\text{PbI}_2$  and MAI are combined in DMF, the iodoplumbate complexes that form most closely resemble the solid state intermediate complexes identified as being mechanistically important for the synthesis of  $\text{MAPbI}_3$ , rather than  $\text{PbI}_2$  or  $\text{MAPbI}_3$  itself, albeit without coordinated solvent in the case of solutions with HI or excess MAI. Importantly, we have offered what to the best of our knowledge is the first experimental evidence of the role HI plays as a solvent additive in improving  $\text{MAPbI}_3$  film morphology. HI acts as a source of  $\text{I}^{--}$  ions, thus allowing the formation of the iodoplumbate complexes formed with the addition of excess MAI, but with a slightly increased coordination number, slightly less structural disorder, and a modified structure. These results may more generally explain the usefulness of other halogen-containing solution additives as means of improving film morphology [68] [69] [70] Our results offer important information about the coordination chemistry and local structural environment of single-step perovskite precursor solutions, which furthers our mechanistic understanding of how solution chemistry can be used to tune final film morphology by carefully controlling the lead coordination complexes present in solution. Such understanding will become increasingly important as perovskite chemistries become more diverse [47] [71] and more robust, scalable solution-processing protocols are developed for the manufacture of large area perovskite devices and modules [72] [73]



### 3.1.6.1 ACKNOWLEDGMENTS

This work was supported by the Laboratory Directed Research and Development Program at SLAC under Contract DE-AC02- 76-SF00515. Use of the Stanford Synchrotron Radiation Lightsource, SLAC National Accelerator Laboratory, is supported by the U.S. Department of Energy, Office of Science, Office of Basic Energy Sciences, under Contract DEAC02- 76SF00515. The authors thank Drs. Sharon Bone and Ryan Davis for their help with data interpretation and acquisition, respectively. Additionally, Kevin A. Bush is thanked for his invaluable assistance with sample preparation and Dr. Matt Newville for his assistance with proof of concept data acquisition.

## 3.2 Anharmonicity in MAPbBr<sub>3</sub>

In the past five years, a majority of the solar perovskite research has focused on lead iodide perovskites, but recently research has been shifting to lead bromide perovskites. Although methylammonium lead bromide (CH<sub>3</sub>NH<sub>3</sub>PbBr<sub>3</sub>) has shown lower peak efficiencies of 10.4 % compared to it's iodide counterpart at  $\sim 22\%$  , it has proven more robust with a larger bandgap[74]. This larger bandgap leads to a high open circuit voltage device [75] and shows promise in tandem device applications [76]. Concerning degradation, it appears that tuning the bandgap of a more robust material (perhaps a blend of organic and inorganic lead halide perovskites) will prove to be the successful path to commercial devices, see [77].

The goal of this project was to investigate local and average structure of bro-

mide perovskites  $\text{CH}_3\text{NH}_3\text{PbBr}_3$  ( $\text{MAPbBr}_3$ ),  $\text{CH}_5\text{N}_2\text{PbBr}_3$  ( $\text{FAPbBr}_3$ ), and  $\text{CsPbBr}_3$ , and elucidate the role of static and dynamic disorder in structural phase transitions. Due to beam time limitations and issues with powdered sample crystallite size this thesis only includes a thorough analysis of the organic  $\text{MAPbBr}_3$  perovskite. The expected phase transitions in  $\text{MAPbBr}_3$  are at  $T \sim 147$  K (orthorhombic to tetragonal), and  $T \sim 236$  K (tetragonal to cubic). The transition from  $pnma$  to  $I4/mcm$  may include an intermediate tetragonal phase, and as will be shown, the transitions in this material are complex.

Organic and inorganic lead halide perovskites exhibit extremely soft bonds and anharmonic vibrations in the cubic phase (room temperature). Dynamic disorder that leads to local symmetry breaking may be the key to understanding the surprisingly low recombination rates in these solar perovskites [78], a characteristic that sets them apart from other light harvesters.

Samples were fabricated by David Cahen and Yevgeny Rakita at the Bar Ilan University in Ramat Gan, Israel, and include annealed and unannealed powders. Due to the softness of the powder we believed grinding would introduce disorder; however, the sample fabricators had to be cautious minimizing degradation while annealing. The  $\text{MAPbBr}_3$  was powdered with grain size of  $< 5 \mu\text{m}$  and annealed at  $90^\circ$  for 15 minutes after grinding. We found no significant difference in the EXAFS scans between annealed and unannealed samples.

### 3.2.1 EXAFS Data

The data were collected for this sample at beamline 4-1 using the Si (220) crystal set. For each annealed sample, 3 scans were collected for two different samples; but due to the negligible difference in data between them, we end up averaging all 6 scans together for each temperature. The expected phase transitions at 147K and 236K compel us to collect EXAFS data at  $\pm 5\text{K}$  around the transitions in search of fit parameter discontinuities. Before meaningful analysis in k-space and r-space could take place, great care had to be taken in reducing the data.

The k range for the Pb  $L_{III}$  edge data is limited by the Br K edge, which it runs into. With this in mind, we observed clear oscillations of the tail of Pb edge in the pre-edge of the Br data, thus knowing that it needed to be subtracted. We fit the first peak in r-space of the Pb data in a Gaussian rounded k-window of  $3.8\text{--}10 \text{ \AA}^{-1}$ . With parameters optimized and locked, we shifted the k window to  $3.8\text{--}19.7 \text{ \AA}^{-1}$  for one iteration to simulate the extended oscillations of the Pb—Br scatter path. This k-space simulated data file was converted into energy space and interpolated with splines to form a continuous “stencil” function. This Pb “stencil” was then shifted by  $\sim 1\text{eV}$  to nicely fit the Br data pre-edge. the results can be seen in Fig. 3.8.

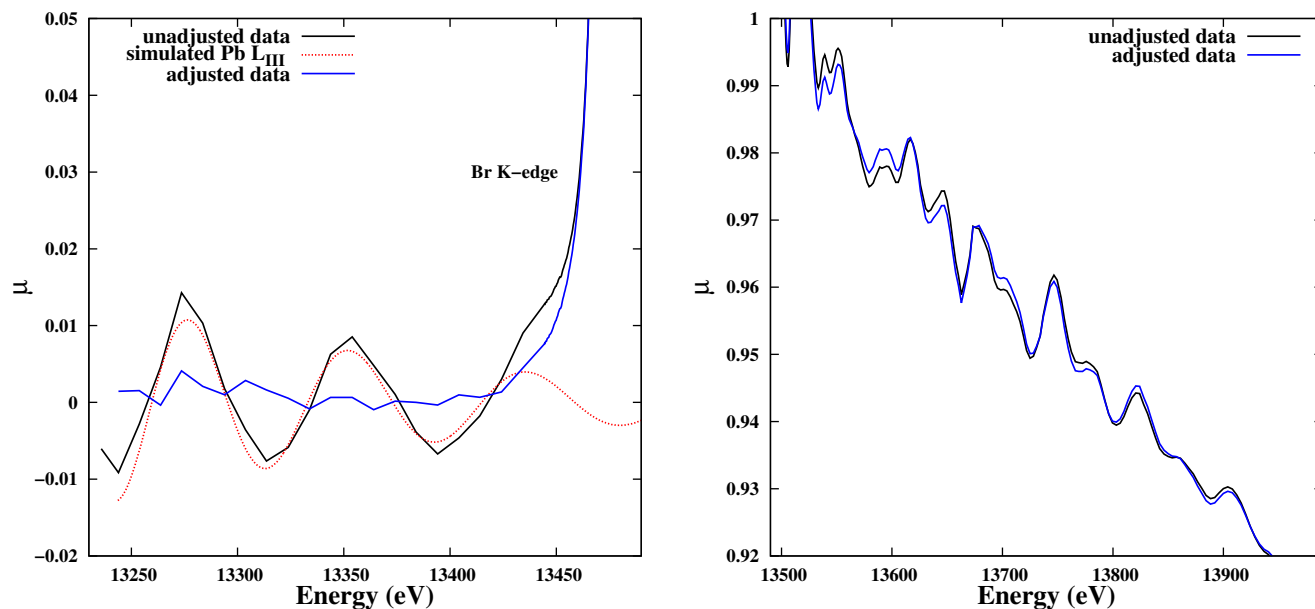


Figure 3.8: Before Br data could be fully reduced we had to address the oscillations in the pre-edge, which were the tail end of the Pb L<sub>III</sub> edge. To account for the Pb oscillations up to  $k \sim 20 \text{ \AA}^{-1}$  the first peak (highly coordinated Pb—Br) of the real-space Pb data was fit. Those fit parameters were fixed as we extended the k-window to beyond the range of our Pb data and simulated the dominant oscillation into the Br K edge. The resulting stencil was interpolated into a continuous function and fit to the first 20 points of data below the edge in the Br data. You can see this fit and resulting subtraction of the Pb background in the pre-edge (left) and resulting adjustment in the EXAFS region in energy space.

The complex background in the Br data also consisted of a multi-electronic excitation at  $\sim 90$  eV above the edge, manifesting itself as a broad bump in absorption. If left unaccounted for, this type of broad bump in the XANES-to-EXAFS transitional region (in  $E$ -space) can lead to poor spline fitting near a false  $E_{min}$ . The poor background fit results in high amplitude below  $1.5 \text{ \AA}$  in  $r$ -space, a region where we do not expect any atomic shell. In the RSXAP data reduction package, there is a hidden manual menu for addressing these issues and the solution is usually fixing a certain knot for the spline polynomial background fit. By fixing one knot, the background function can be diverted from forming a concave “cup” shape in the XANES region; we expect to get a background function that has a convex “hump” when approaching  $E_{min}$  – see Fig 3.9.

Now with properly reduced data, we quickly find novel behavior present in both edges: the accordion effect at high  $k$ . Temperature dependent EXAFS data does not usually exhibit a shift in zero-crossings, and in this case we see zero-crossings increasing with temperature and  $k$ . In the  $k$ -space data in Figs. 3.10 and 3.11 we find the zero-crossings increase with temperature and with  $k$ , a clear sign of anharmonicity turning on as  $T$  increases. This can be understood by looking quickly back at Ch. 2; we recall the oscillatory functional form of  $\chi(k)$  when including the cumulant expansion:

$$\sin\left(2k\left((r_i + \Delta r) - 2\sigma^2\left(\frac{1}{r_i} + \frac{1}{\lambda}\right)\right) - \frac{4}{3}C_3k^3 + \phi(k)\right) \quad (3.3)$$

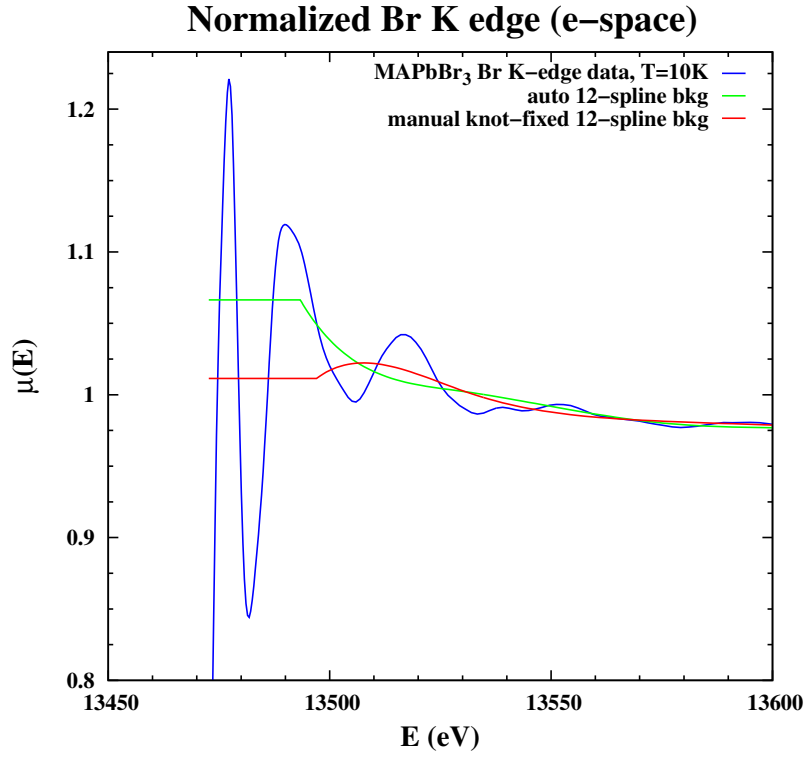


Figure 3.9: Low temperature (10K) Br e-space near-edge with two different 12 spline background fits. The automatic background fits itself to the expected multielectronic excitation hump, which then results in a poor background near  $E_{min}$ . By manually fixing a knot, we minimize low-r amplitude in r-space.

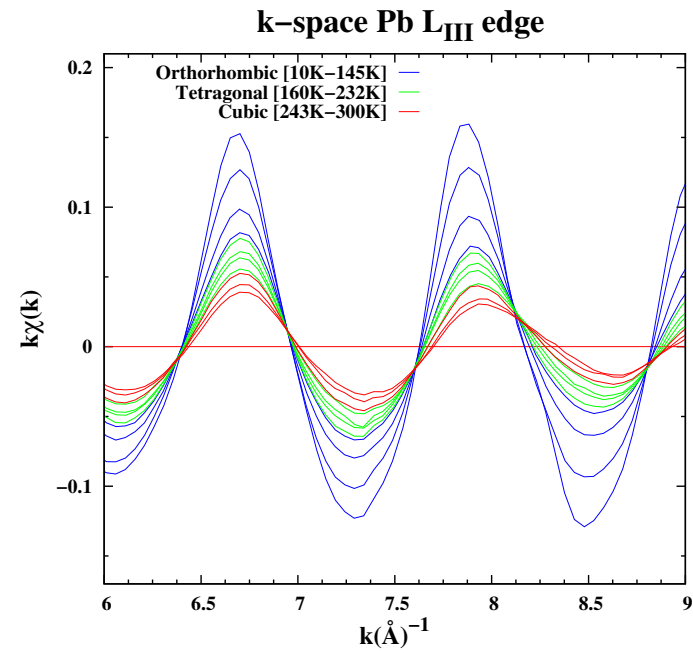
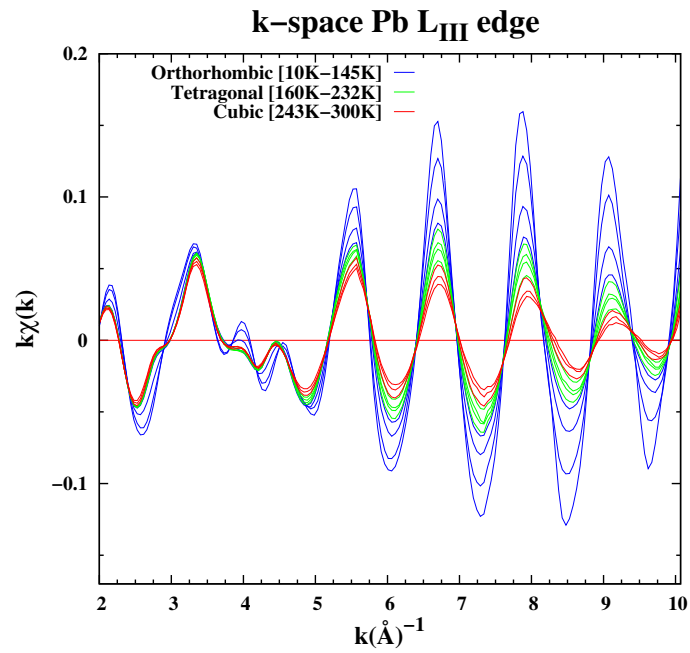


Figure 3.10: Pb L<sub>III</sub> data in k-space that exhibits an unusual temperature dependence. Upon closer inspection of zero-crossings, the accordion effect associated with anharmonic motion is evident; at high  $k$ , the positions of the zero-crossings move to higher  $k$  as  $T$  increases.

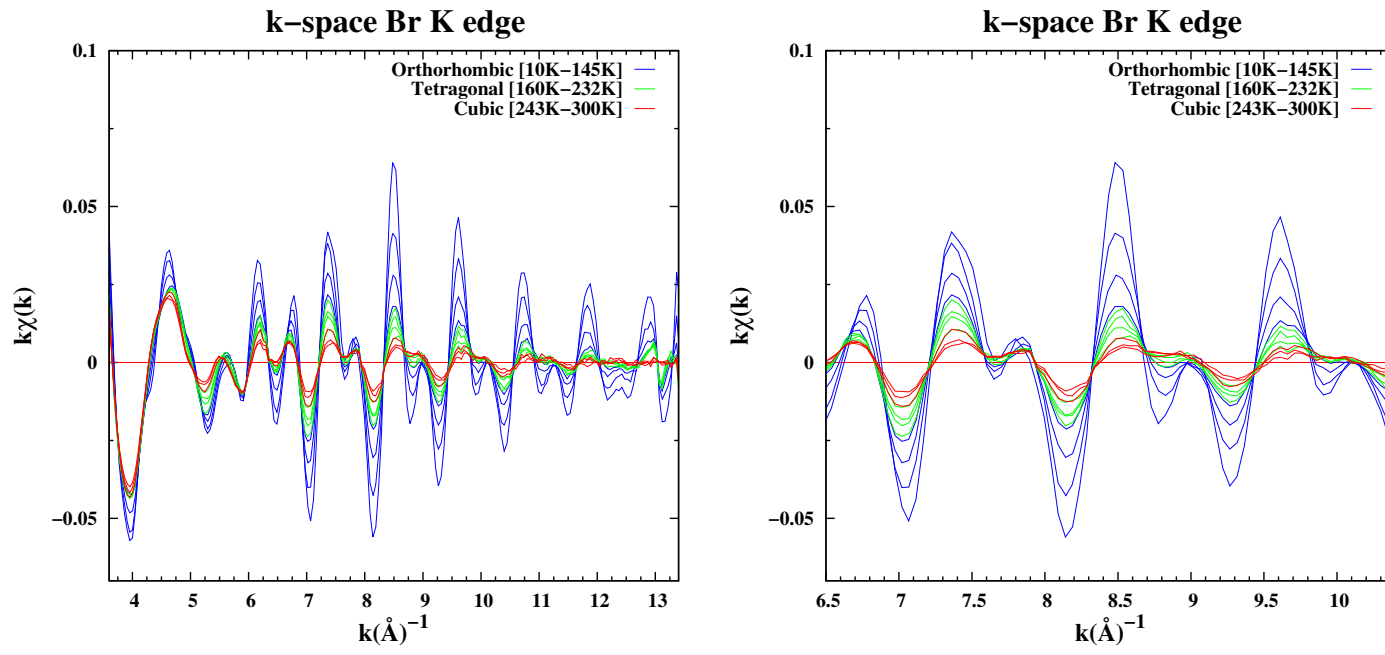


Figure 3.11: Br K-edge data in  $k$ -space that exhibits a similar temperature dependence. Upon closer inspection of zero-crossings, there is an accordian effect similar in magnitude to Pb  $L_{III}$  edge data.



The asymmetry of a pair distribution is quantified by the term  $C_3$  in the EXAFS equation, and in our fit. By looking at the data we can see there is a dominant anharmonic bond pair. In assuming it is the nearest neighbor, we can take a back fourier transform from r-space to k-space where we only include the large low r peak (at  $\sim 3\text{\AA}$ ). When this is done, we can see in Figs. 3.12 and 3.13 a clear accordion effect and thus conclude that it we are observing anharmonicity of Pb-Br bond.

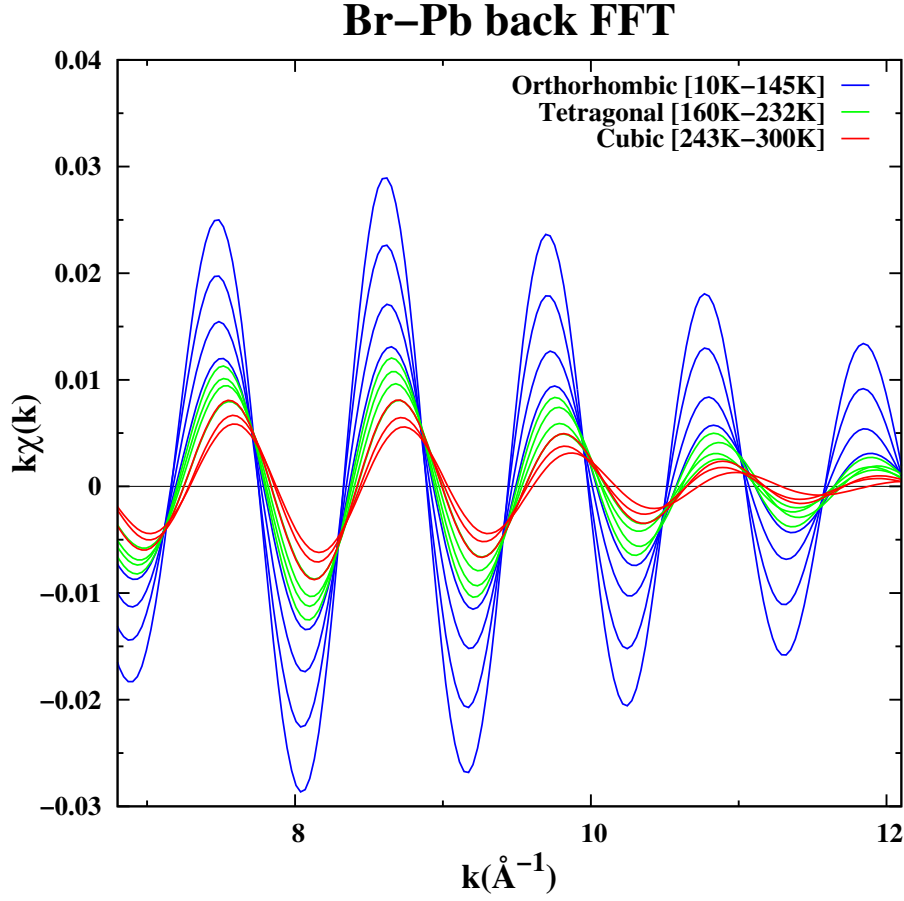


Figure 3.12: After reducing Br K-edge data by removing residual Pb absorption and manually spline fitting, we transform into real space to find a clear peak  $\sim 3$  Å. Then we can back fourier transform only this first peak, associated with nearest neighbor Pb coordination, to see individual contribution to the anharmonicity in the k-space data is due to the nearest neighbor.

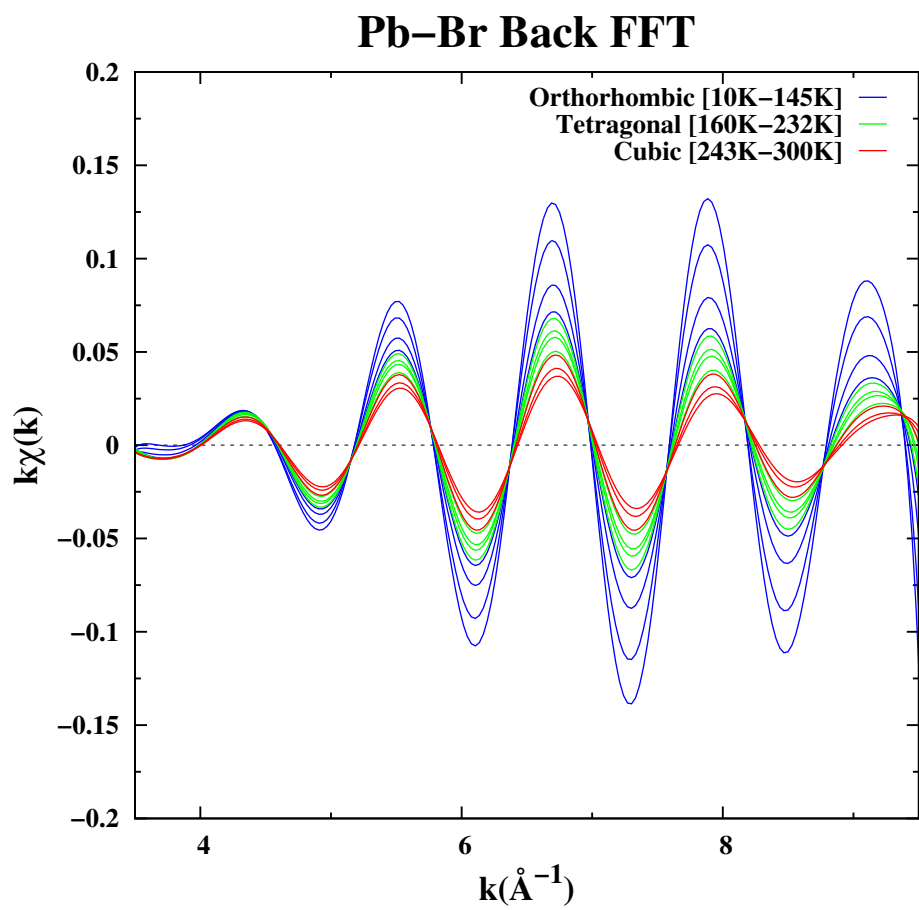


Figure 3.13: Back transformation into  $k$ -space of the first Pb–Br peak in Pb edge  $r$ -space data.

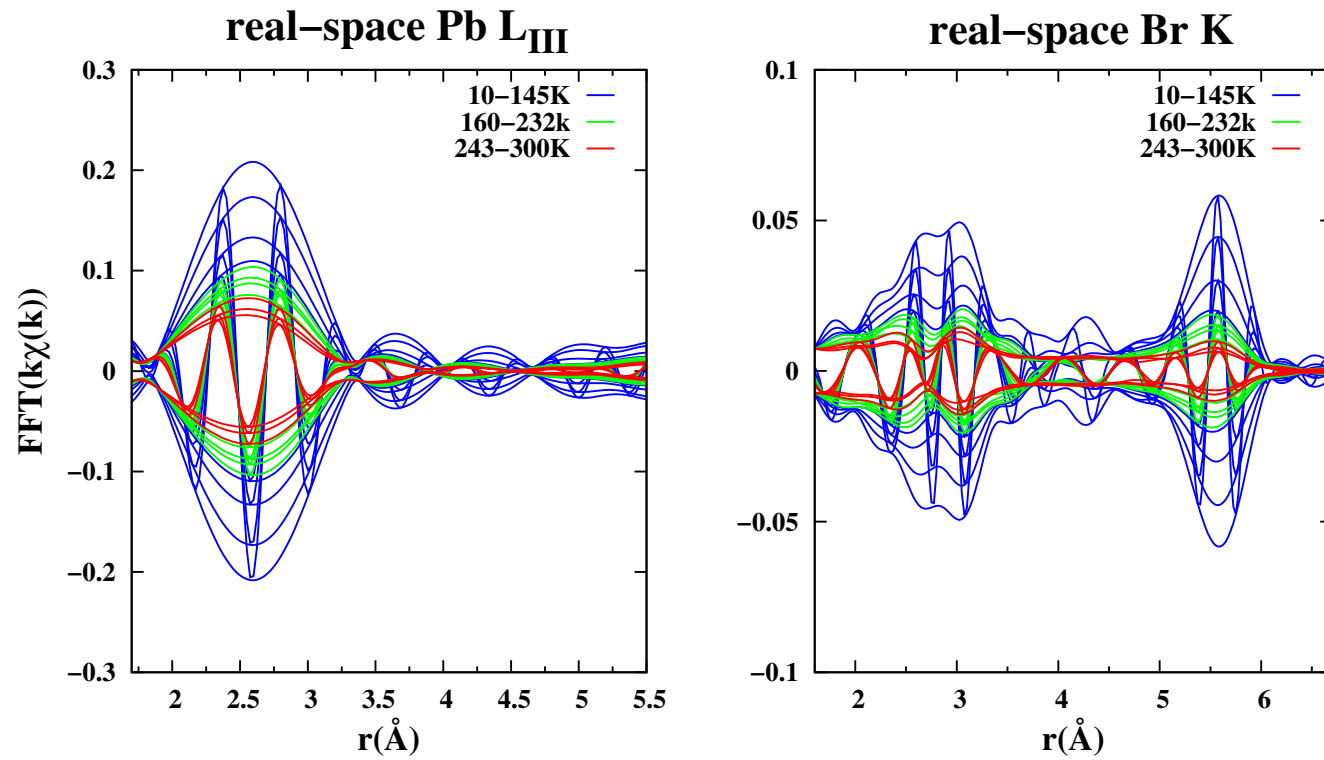


Figure 3.14: Averages of real space data of the Pb L<sub>III</sub> and Br K edges. Each color corresponds to a nominal structural phase.

### 3.2.2 Fits

The fits are to the first peak, and the Pb fit consists of a Pb—Br standard at 2.97 Å with bromine degeneracy of 6. The Br edge data is more difficult to fit; we use a two-fold degenerate Br—Pb standard at 3.11 Å and a small Br—N standard at 3.43 Å which were generated from a *pnma* cif file. The fits to the low-T real-space data can be viewed in Figs. 3.15 and 3.16 for Br and Pb respectively. The Pb data has low amplitude structure beyond the nearest Br neighbor; the latter is realistically a distribution of several slightly different bond-lengths in the low-T phase (*pnma*) but can be fit well with one broad Pb—Br peak. The coordination and order in the first shell Pb—Br provided for a good fit and greater certainty than the Br data in  $\Delta r$  values as a function of temperature, see Fig 3.17. The  $\Delta r$  values from the Pb edge fit are used and fixed in the Br fit, as we expect the same bond-length shifts for both edges. Further, when extracting the  $C_3$  from fits we must minimize to or eliminate the correlation factor between  $\Delta r$  and  $C_3$  (as well as  $E_0$  which is fixed to -6eV). By fixing the r-shifts to the best values for each temperature for the Br K edge data, we will be able to directly compare the magnitude of  $C_3$  from the fit of each edge.

The Br data has a more complex structure. At  $r \sim 3\text{\AA}$  in Fig. 3.15 we find a triple peak form, a result of interference between two bond pairs: Br—Pb that exhibits it's hallmark double-peak, and Br—N at 3.43 Å. The intermediate regime from 4–5.4 Å shows little structure even though there are 8 Br—Br second shell neighbors. We expect the softness and resulting disorder in these bond pairs, as well as the destructive

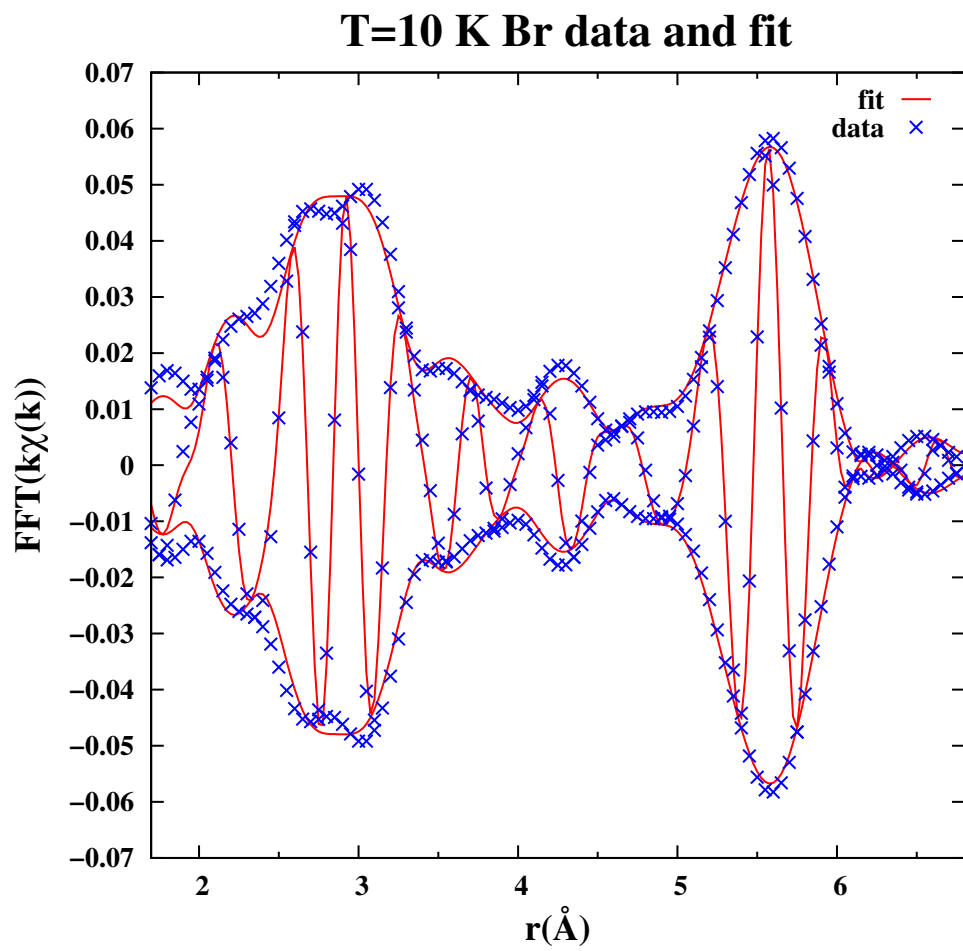


Figure 3.15: Fit for the average (6 scans) Br 10K data.

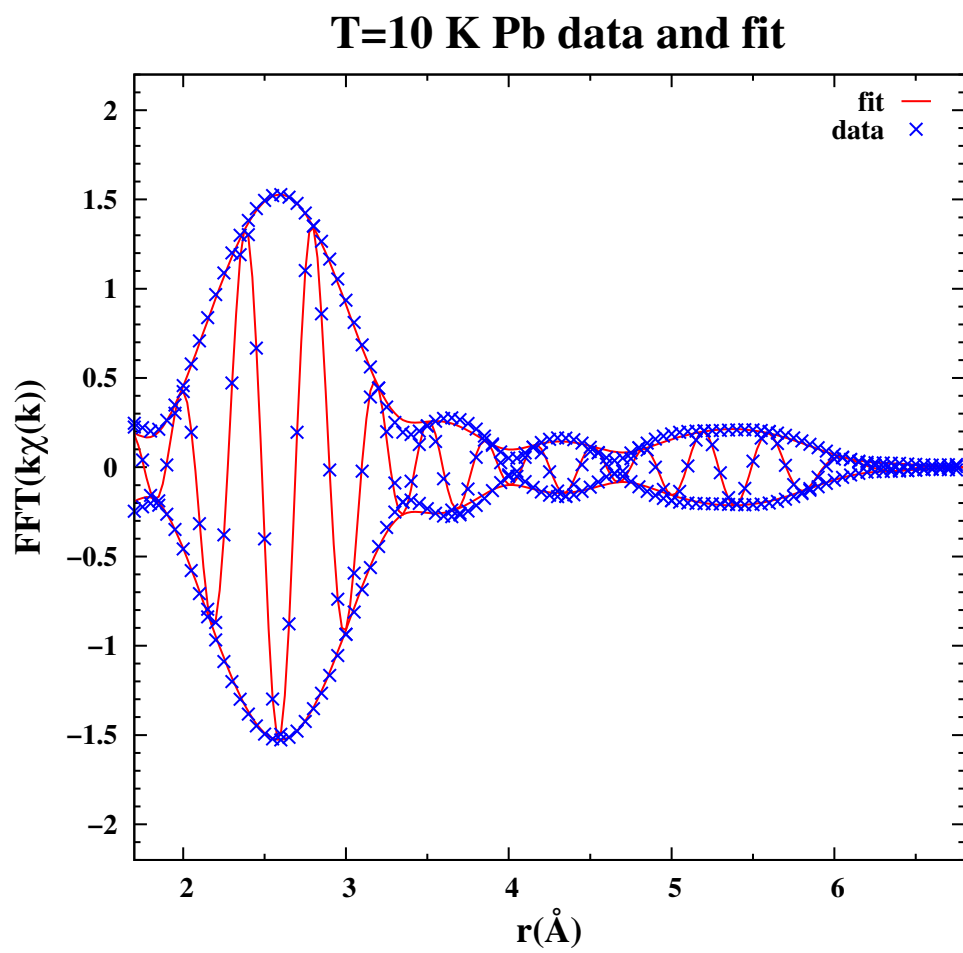


Figure 3.16: Fit for the average (6 scans) Pb 10K data.

interference between scatter paths, to be the cause of this. The region above 4 Å was fit separately, and then the peaks and parameters were locked for the relaxing total fit ranging from 1.9–7 Å.



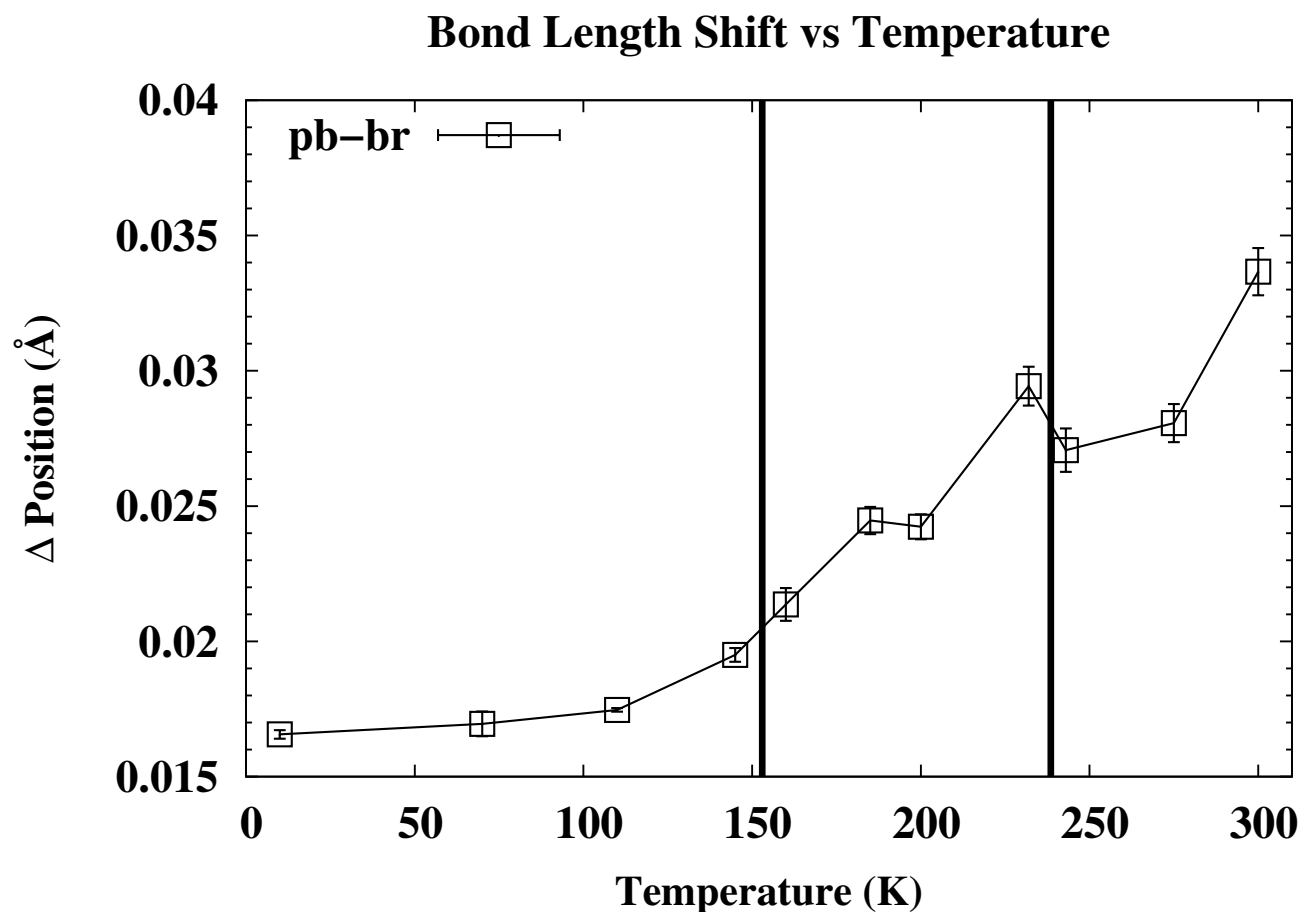


Figure 3.17: Shift in bond length (nominally  $2.977 \text{ \AA}$ ) for the Pb–Br bond as a function of temperature, extracted from Pb edge data. The vertical black lines represent the nominal temperatures for orthorhombic to tetragonal transition (left), and the tetragonal to cubic transition (right). These values were fixed in Br edge fit due to the correlation between  $C_3$  and  $\Delta r$ . There is a smooth increase in bond-length until part-way through the tetragonal phase, where there appears to be a small step.

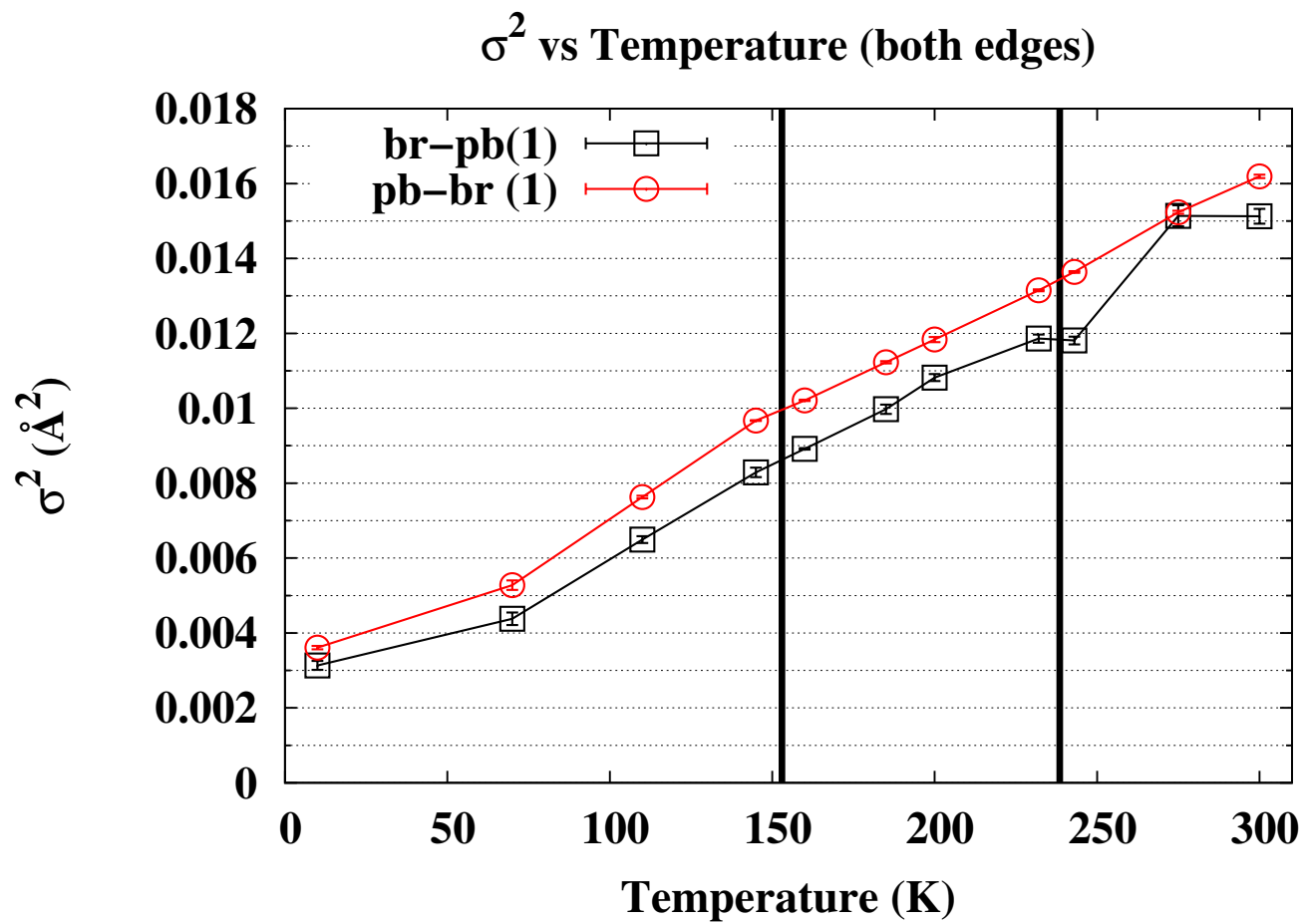


Figure 3.18: Fit parameter  $\sigma^2$  for the first neighbor of each edge. This shows nearly identical broadening with temperature, taking a linear form without major discontinuity at nominal phase transition temperatures.

The plot  $\sigma^2$  vs. temperature shows a linear relationship for the first shell from both edges, with slightly differing slope:  $4.61 \times 10^{-5} \text{ \AA}^2/\text{K}$  and  $4.48 \times 10^{-5} \text{ \AA}^2/\text{K}$  for Br and Pb data respectively when fitting with a linear model through the origin. These linear approximations will be relevant when extracting the  $C_3$  parameter from isosbestic points in k-space.

When appropriate, we can include the  $C_3$  parameter in fitting a bond-pair that we assume to have an asymmetric distribution. Using the oscillatory approximation from eq. 3.3 we see there can be non-negligible correlations between  $C_3$  and  $r$ . We account for this by fitting Pb data and using those temperature dependent bond-lengths in the Br fit (of the same bond-pair). Upon fitting the Br peak we converge on a similar temperature dependence of  $C_3$ , which will remain even when letting the  $\Delta r$  parameter free. The resulting  $C_3$  from fitting is seen in Fig. 3.20 as black and red for Br and Pb data respectively.

After plotting and quantitatively analyzing the zero crossings of k-space data, we sought to derive a new method of deriving  $C_3$  directly from data. If we consider a general form of the oscillating part of  $\chi$  as  $\sin(\Theta)$ , then at zero crossings we have the following condition:

$$\Theta(T) = 2kr_i - \frac{4}{3}C_3^{(i)}k^3 + \phi(k) = 2\pi m \quad (3.4)$$

for each temperature,  $i$ , and integer  $m$ . If we take the difference of  $\Theta$  at two temperatures, the  $\phi$  term cancels and we end up with the following formula for  $C_3$ :

$$C_3 = \left(\frac{2}{3}\right) \left( \frac{\frac{\Delta k}{k_0^3} + \frac{\Delta r}{k_0^2}}{1 + 3\frac{\Delta k}{k_0}} \right) \quad (3.5)$$

where  $k_0$  is the zero-crossing at 10K,  $\Delta r = r_{i,n} - r_{0,n}$ , and  $\Delta k = k_{i,n} - k_{0,n}$ . The convention we use here is indexing temperature with  $i$ , and crossing number with  $n$ , and in Fig 3.19 we graphically show how the  $\Delta k$  is measured. This entails that we can derive a  $C_3$  at each  $n^{th}$  crossing, and so our uncertainties plotted in Fig 3.20 are derived from the standard deviation of our calculated  $C_3$ . Due to complicated background removal and lower signal-to-noise in Br data, we have larger uncertainties using this method. We were pleased to find such agreement between this new method and the fit parameter  $C_3$ .

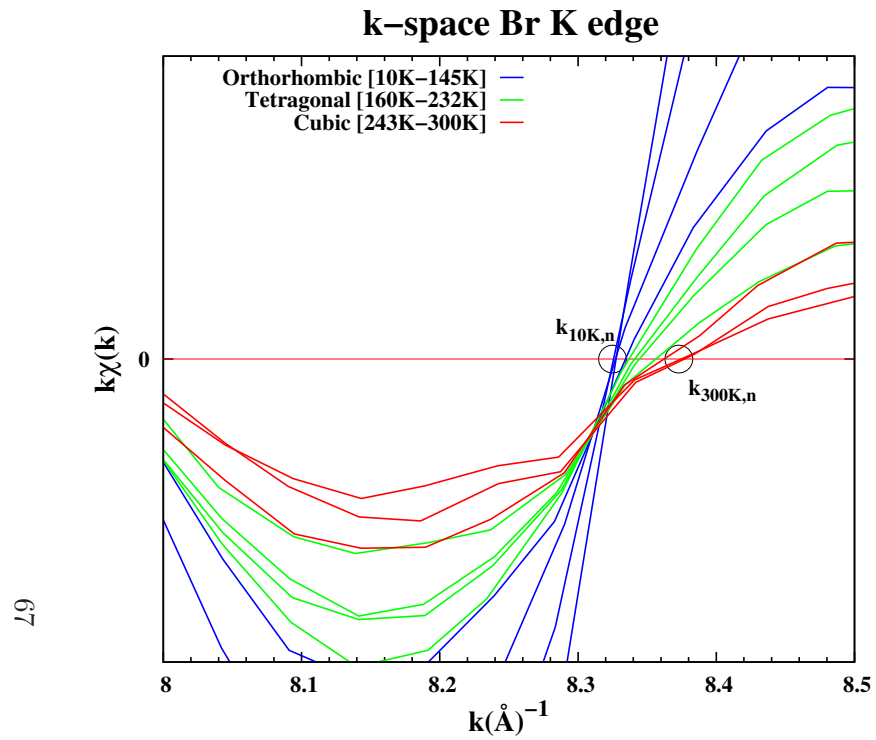


Figure 3.19: A blown-up example of how  $\Delta k$  is measured in back-transformed Br k-space data.

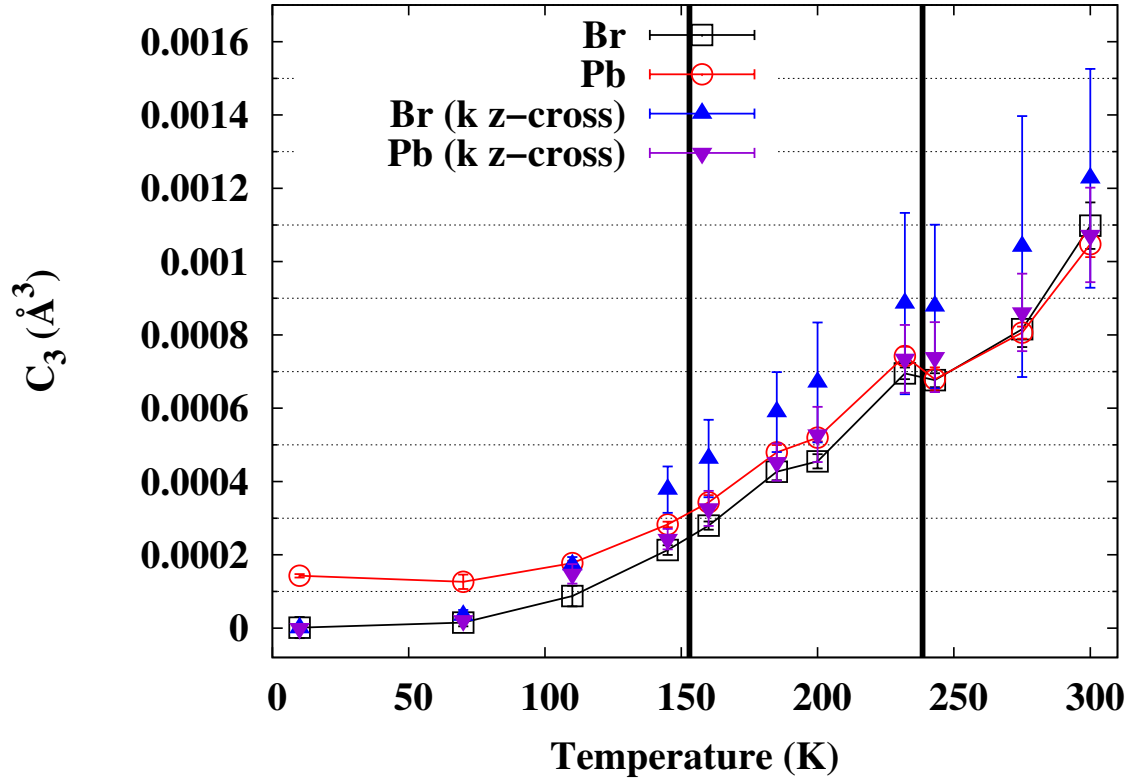


Figure 3.20: Asymmetric fit parameter  $C_3$  of the first neighbor for both edges in black squares and red triangles for the Br–Pb and Pb–Br peak respectively. This quantifies the anharmonic motion resulting in an asymmetric pair distribution, likely due to the transverse motion of Br at the octahedral corners. In blue and purple triangles is the  $C_3$  parameter extracted from the temperature dependence of zero-crossings in  $k$ -space. One can see how closely it follows the  $C_3$  from fitting.

As we further investigated the k-space data, we discovered that isosbestic points at which k-space data at all temperatures approximately converge. When considering points of convergence where  $\chi(k)$  is not zero, we must divide out the simulated backscattering amplitude,  $F_{eff}(k)$ . This is important because generally speaking, a balance of two parameters will lead to the observed invariability of  $\chi$  at certain  $k$ : the broadening ( $\sigma^2$ ), and phase shift ( $C_3$ ). We denote an isosbestic point in  $k$  as  $k_{b,n}$ , such that we can associate the relative phase shift from an isosbestic point's corresponding zero-crossing. Fig. 3.21 shows an example of an isosbestic point after scaling data by  $F_{eff}$ .

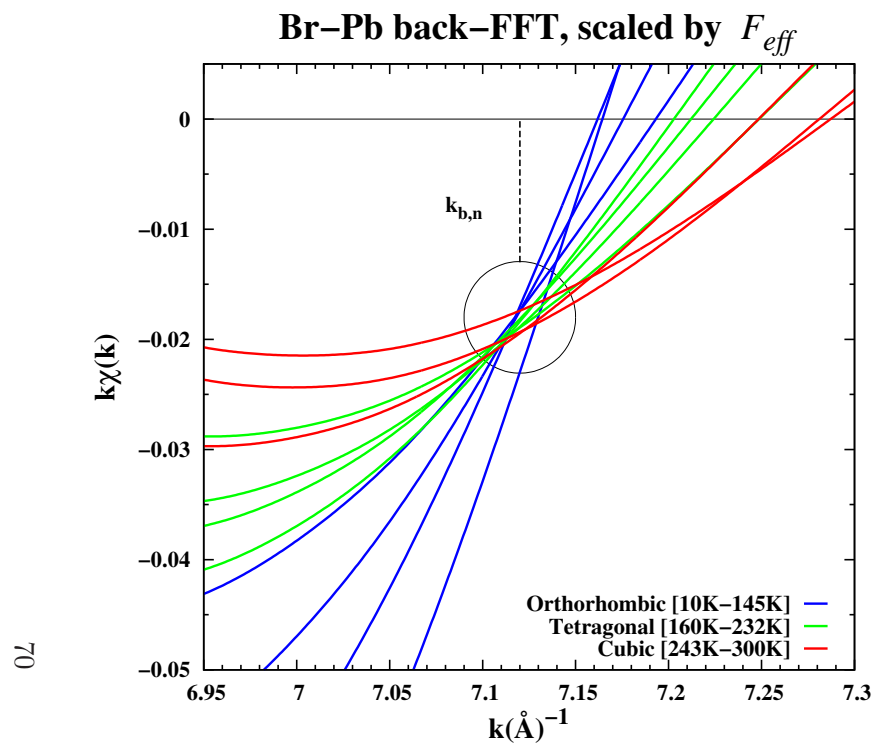


Figure 3.21: A blown-up example of isosbestic point in back fourier transformed Br data,  $k_{b,n}$ , and it's relative value compared to corresponding zero-crossings.



At an isosbestic point  $\frac{d\chi}{dT} = 0$ . We can follow with this principle, and attempt to derive the remaining pieces of  $\chi$ :

$$\frac{d}{dT} \left( e^{-2k_{b,n}^2 \sigma^2} \sin(2k_{b,n} r - \frac{4}{3} C_3 k^3 + \phi(k_{b,n})) \right) \quad (3.6)$$

Taking into account that the  $\sin(\Theta)$  term is small at a point  $k_{b,n}$ , we can invoke the approximation:

$$\sin(\Theta) \approx \frac{\Delta_{i,n}}{D_{i,n}} \pi \quad (3.7)$$

where  $\Delta_{i,n} = |k_{i,n} - k_{b,n}|$  and  $D_{i,n} = \frac{1}{2}(k_{i,n+1} - k_{i,n-1})$ . Deriving after using small angle approximations and neglecting the small contribution from  $\frac{dr}{dT}$ , we are lead to a succinct relationship between  $C_3$  and  $T$ :

$$\frac{dC_3}{dT} = \frac{3}{2k_{b,n}} \left( \frac{d\sigma^2}{dT} \frac{\Delta_{i,b}}{D_{i,n}} \pi \right) \quad (3.8)$$

In order to compare to the fit extracted  $C_3$ , we found it effective to numerically integrate the above data series,  $\frac{dC_3}{dT}$ , over temperature (using Simpson's rule). Then we set the initial isosbesticly extracted  $C_3$  at 70K to equal the corresponding  $C_3$  from the fit. The curves in Fig. 3.22 show decent agreement of curve shape and includes error bounds for the empirically determined uncertainty in  $k_{b,n}$ .

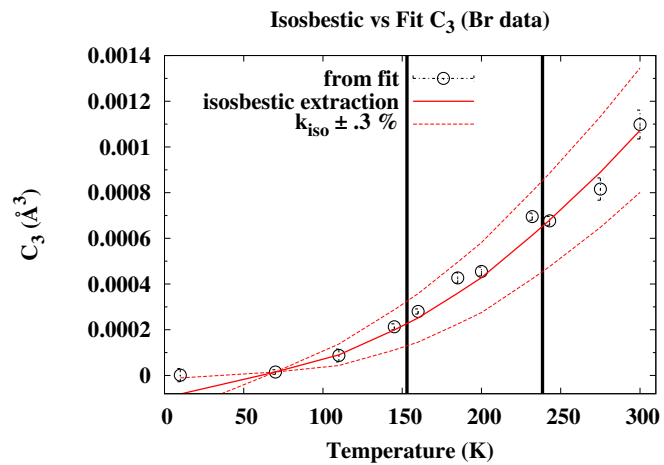
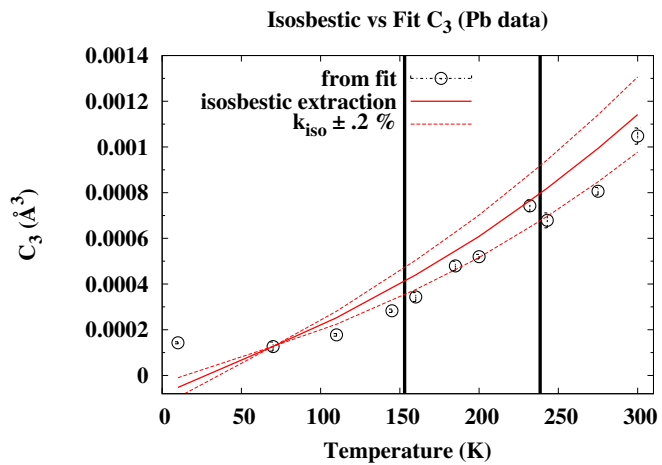


Figure 3.22: A comparison of isosbastically integrated  $C_3$  and  $C_3$  from fitting, with Pb results on the left, and Br results on the right. The dashed red curve shows error bounds when extracting  $k_{b,n}$  from an isosbestic region, and demonstrates the sensitivity of the integrated  $C_3$  when isosbestic regions are not point-like.

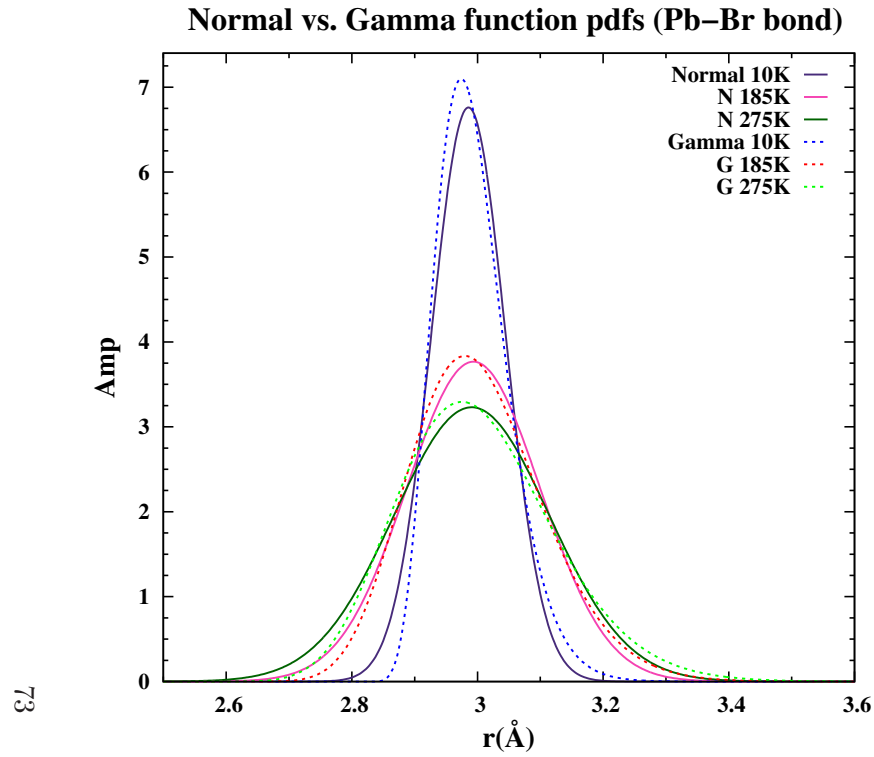


Figure 3.23: Symmetric distributions (solid lines) are plotted with their asymmetric counterparts (dashed lines) using  $r$  and  $\sigma^2$  values at several temperatures extracted from fitting. Asymmetric distributions plotted here are piecewise functions defined as :  $\frac{\alpha^{1+s}}{\Gamma[1+s]}(r-r_0)^s e^{-\alpha(r-r_0)} \Theta(r-r_0)$  [3]. With a positive  $C_3$ , the peaks of asymmetric distributions reside at lower  $r$  than symmetric distributions, but exhibit a high tail as  $r$  increases.

Quantifying the anharmonicity in the Br–Pb bond-pair is paramount. The transverse motion of Br that results in this asymmetric distribution may prove to be a key mechanism in understanding the structural phase transitions in most lead halide perovskites. In Fig. 3.23 the difference between a symmetric and asymmetric distribution is shown in  $r$ -space; transverse motion where a Br cannot get closer to Pb than when the Pb–Br–Pb complex of two neighboring octahedra is co-linear would result in a PDF with a sharp drop-off at the low  $r$  tail. At high temperature the bond pair distribution is softer as bondlength increases; this appears to require significant transverse motion of Br relative to the Pb–Br bond. When the bond is stretched the spring constant is weaker – and that is when it would be easiest to break – thus this may play a role in the degradation and decreased halide coordination of this family of materials at elevated temperatures. To consistently quantify anharmonicity three different ways for both the Pb and Br edge is a rigorous and delightful result. We hope to inspire other experimental XAS groups in the field to investigate their data beyond typical procedures.

## Chapter 4

# Calcium Fluorite doped with Ytterbium

This chapter is an adaptation and merging of the following two papers [79; 80]:

C. MacKeen, F. Bridges, M. Kozina, A. Mehta, M. F. Reid, J.-P. R. Wells, and Z. Barandiaran, “Evidence That the Anomalous Emission from  $\text{CaF}_2\text{:Yb}^{2+}$  Is Not Described by the Impurity Trapped Exciton Model”, *J.Phys.Chem.Lett.* 8, 3313 (2017).

C. MacKeen, F. Bridges, L. Seijo, Z. Barandiaran, M. Kozina, A. Mehta, M. F. Reid, and J.-P. R. Wells, “The Complexity of the  $\text{CaF}_2\text{:Yb}$  System: A Huge, Reversible, X-ray-Induced Valence Reduction”, *J.Phys.Chem.C* 121, 28435 (2017).

### 4.1 Overview

In a large number of lanthanide doped crystals there is a large Stokes shift of the fluorescence emission upon UV excitation, particularly for  $\text{Yb}^{2+}$  and  $\text{Eu}^{2+}$  ions[26]. The optical properties of  $\text{CaF}_2\text{:Yb}^{2+}$  were first reported about 50 years ago[81; 82], and the unusually large red-shift and bandwidth of the fluorescence emission were considered

anomalous. A model to describe such systems was developed in the 80's by McClure and others[24; 25; 26], in which the optical center is called an impurity trapped exciton (ITE). Dorenbos[26] provides a long list of potential ITE systems with anomalous emissions, mostly with Yb and Eu dopants.

Upon UV excitation (within this model), one of the  $4f^{14}$  electrons of  $\text{Yb}^{2+}$  is excited to the  $4f^{13}5d$  state; this state decays to the exciton state in which the excited electron forms a delocalized extended state on neighboring metal atoms[25]. The resulting  $\text{Yb}^{3+}$  ion plus the delocalized electron state forms the transient ITE state – a bound electron-hole pair. While in the ITE state, the cube of surrounding  $\text{F}^-$  atoms should collapse slightly (again a transient effect), leading to a decreased Yb-F bond distance - by  $\sim 0.2 \text{ \AA}$ , [24] which explains the bandwidth of the emission. The ITE model has been accepted in the literature for over 30 years [24; 25; 26; 83; 84; 85] and continues to be used in the current literature. [86; 87]

Recently, however, Barandiarán and Seijo [88] have examined the ITE hypothesis by means of *ab initio* relativistic quantum chemical calculations. The results for  $\text{Yb}^{2+}$  in  $\text{CaF}_2$  allow the authors to conclude that none of the electronic states of the  $\text{Yb}^{2+}$  active centers can be considered responsible for the anomalous emission; hence the need of direct experimental scrutiny of the ITE model.

Lanthanides are multivalent chemical systems whose luminescence activates numerous optical devices. Their multivalent nature sets a complex scenario that challenges widespread single-valent-ion models. In addition to probing the meta-stable states anomalous luminescence, we study the complexity inherent in the  $2+/3+$  mixed-

valence nature of Yb in  $\text{CaF}_2$ . We report x-ray absorption spectroscopy of  $\text{CaF}_2\text{:Yb}$  that shows a maximal, huge  $\text{Yb}^{3+}$  x-ray-induced valence reduction at 200 K for low Yb concentration (0.01 %) samples, which reverts to the initial state upon warming to 300 K. Although reduction doubles the number of  $\text{Yb}^{2+}$  ions, the anomalous emission that is normally observed at low temperatures completely disappears and never recovers. Surprisingly however, after annealing at 900 K, some anomalous emission is again observed below 150 K. Under x-ray exposure electrons are ejected from the  $\text{F}^-$  ions, including charge compensating interstitials,  $\text{F}_i^-$ . Removing an electron from  $\text{F}_i^-$  leaves a neutral atom which appears meta-stable. *Ab initio* calculations of the  $\text{F}_i^-$ -to- $\text{Yb}^{3+}$  electron transfer reveal there is a critical dopant-compensator distance below which reoxidation is spontaneous and above which it is not. This, together with temperature dependent  $\text{F}_i^0$  and  $\text{F}_i^-$  mobilities, and the interpretation of the anomalous emission as an  $\text{Yb}^{2+}$ -to- $\text{Yb}^{3+}$  electron transfer, provides a model for interpreting the complex experimental observations.

## 4.2 Shortcoming of Impurity Trapped Exciton Model

Yb substitutes for Ca in  $\text{CaF}_2\text{:Yb}$  and forms several defects. Clusters form at higher concentrations[89; 90], while the anomalous emission centers form at much lower concentrations. In the ITE model the number of excitons excited by UV should be proportional to the number of  $\text{Yb}^{2+}$  ions present. At the time the ITE model was first developed there was no way to measure the  $\text{Yb}^{2+}$  concentration in order to check

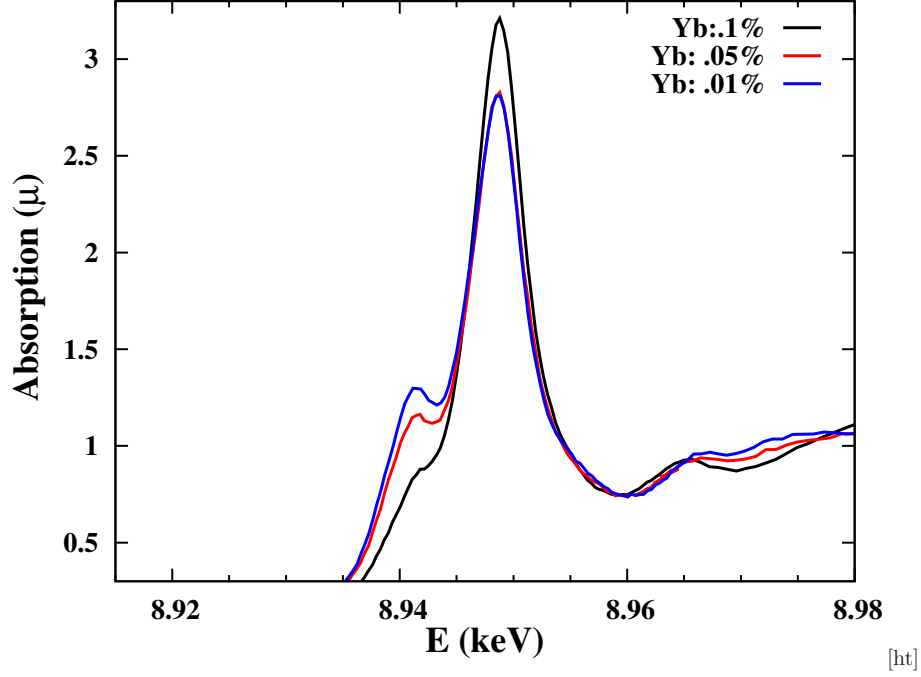


Figure 4.1: The normalized Yb  $L_{III}$  edge absorption coefficient,  $\mu$ , as a function of total Yb concentration (0.01, 0.05, and 0.1 % Yb) for fresh samples at 10 K. The  $Yb^{2+}$  peak is at 8942 eV while the  $Yb^{3+}$  peak at 8949 eV. The  $Yb^{3+}$  peak still dominates even at the lowest concentration, 0.01% Yb.

for a linear dependence of anomalous luminescence intensity. In fact only recently has this been possible for very low defect concentrations down to 0.01% Yb. Here we provide direct experimental evidence that the ITE model cannot explain anomalous luminescence in  $CaF_2:Yb$ ; first the anomalous luminescence intensity is not proportional to the  $Yb^{2+}$  concentration, and second, only a small fraction of  $Yb^{2+}$  ions are involved in anomalous emission.

Normalized Yb  $L_{III}$  absorption edges are plotted in Fig. 4.1 for three concentrations: 0.01, 0.05 and 0.1% Yb; the plots are normalized well above the edge. The  $L_{III}$



edge has two peaks separated by about 7 eV: the lower one (8942 eV) is associated with  $\text{Yb}^{2+}$  while the upper one (8949 eV) is for  $\text{Yb}^{3+}$ . For the higher concentration samples the  $\text{Yb}^{3+}$  peak dominates and only below  $\sim 0.05\%$  is there a separate, well defined  $\text{Yb}^{2+}$  peak; this peak is largest for the 0.01% Yb sample. Hughes-Currie *et al.* recently showed for higher Yb concentrations that the  $\text{Yb}^{2+}$  peak grows as the Yb concentration is decreased.[91] Here we extend such measurements down to lower concentrations.

A fit of the  $L_{\text{III}}$  edge for the 0.01% Yb sample is shown in Fig. 4.2. The XANES spectrum is fit to a sum of two pseudo-Voigt peaks plus a step function; these are plotted below the data. Similar fits were done for the other samples. In converting to fractional concentrations one needs the relative matrix elements for the 2+ and 3+ transitions; often these are assumed equal. However, Hughes-Currie *et al.*[91] used the ratio  $M^{2+}/M^{3+} = 0.656$  from Eu solutions[92]. In a separate experiment (??) we have determined this ratio for Yb to be 0.93 in  $\text{CaF}_2$ , and that value is used here. Once the fractions  $f(2+)$  and  $f(3+)$  of  $\text{Yb}^{2+}$  and  $\text{Yb}^{3+}$  are known, the estimated concentrations of the two valence states are approximately given by  $f(2+)n_o$  and  $f(3+)n_o$ , where  $n_o$  is the nominal concentration. The concentrations of  $\text{Yb}^{2+}$  and  $\text{Yb}^{3+}$  are plotted in Fig. 4.3 as a function of  $n_o$ . The  $\text{Yb}^{2+}$  concentration tends to saturate even near 0.05% Yb.

The anomalous emission spectra for these samples are plotted in Fig. 4.4. In order to obtain relative intensities, the geometry was kept the same (same orientation and sample thickness) and the incident UV power level was constant. The relative intensities extracted from these data are also plotted on Fig. 4.3; in contrast to the variation of the  $\text{Yb}^{2+}$  concentration, the anomalous emission intensity decreases as the

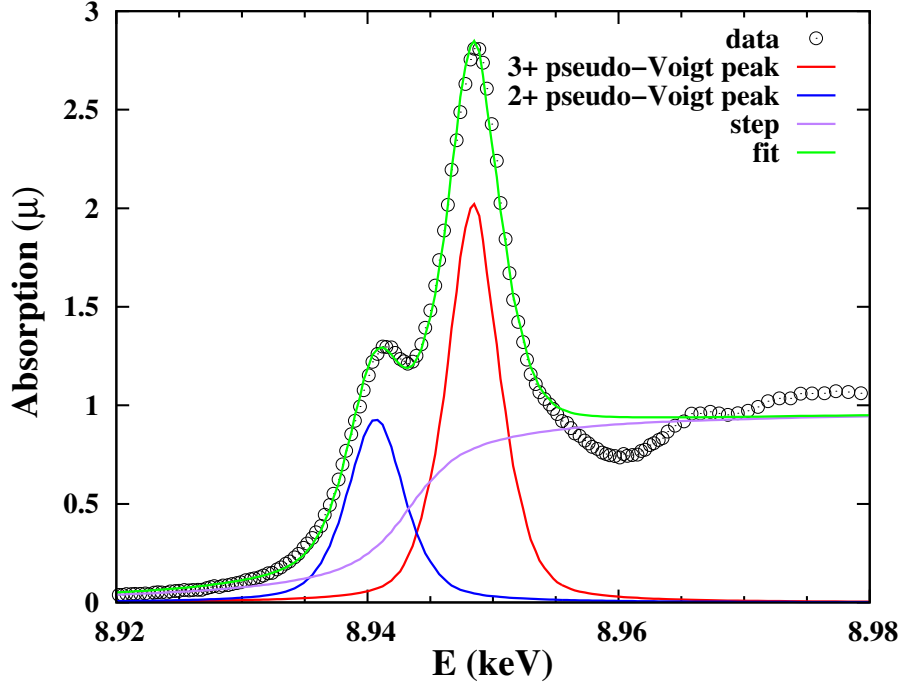


Figure 4.2: Fit of the  $L_{III}$  edge for the 0.01% Yb sample. The normalized data are shown as circles while the fit is shown as a green line. The blue and red pseudo-Voigt peaks show the contributions for  $Yb^{2+}$  and  $Yb^{3+}$  respectively; the main step function is shown as a purple line.

nominal concentration increases.

The results presented above are inconsistent with the accepted ITE model for anomalous luminescence from Yb centers in  $CaF_2$ . As the Yb concentration is reduced, from 0.1 to 0.01 % (Fig. 4.3), the number of  $Yb^{2+}$  ions decreases but the anomalous emission increases dramatically instead of decreasing; the inconsistency from 0.1 to 0.01 % Yb is nearly a factor of 90. Thus only a small fraction of the  $Yb^{2+}$  ions are involved.

A possible new model to describe the anomalous emission in  $CaF_2:Yb$  is that proposed by Barandiarán and Seijo,[88] according to which the anomalous emission

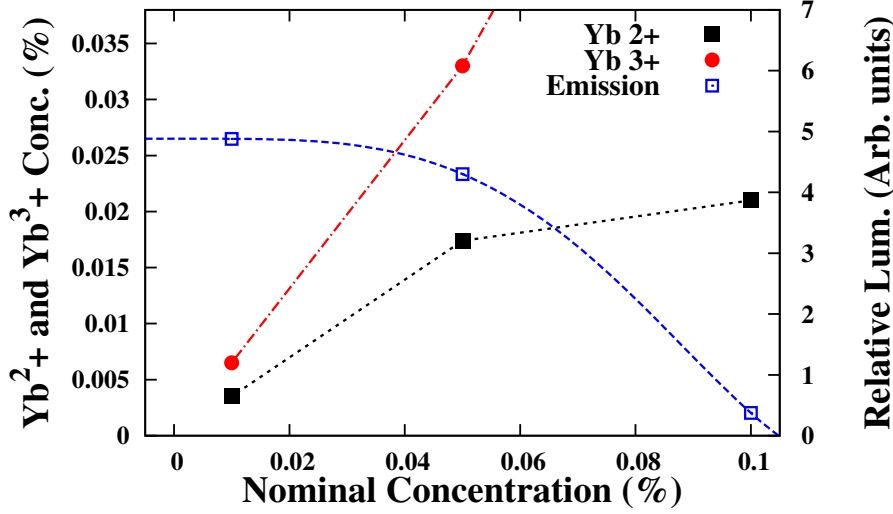


Figure 4.3: The estimated  $\text{Yb}^{2+}$  and  $\text{Yb}^{3+}$  concentrations and the relative anomalous emission intensity (see Fig. 4.4) as a function of the nominal concentration  $n_o$  (0.01–0.1% Yb) for fresh samples. It is clear that the emission intensity is not directly proportional to the concentration of  $\text{Yb}^{2+}$  ions.

is an intervalence charge transfer (IVCT) between  $\text{Yb}^{2+}$  and  $\text{Yb}^{3+}$  defects. The same interpretation has been used to understand that x-ray excitation triggers the anomalous emission of Yb in  $\text{CaF}_2$  but not in  $\text{SrF}_2$ . [93] According to the mechanism proposed for the UV excited anomalous emission, [88] only a fraction of the initially excited  $\text{Yb}^{2+}$  would ultimately lead to IVCT luminescence due to branchings towards the ground state and  $\text{Yb}^{3+}$  emissions. It also has been suggested (theoretically and experimentally) [88; 94] that electron transfer from a divalent ion should be most efficient towards a non-locally compensated (cubic) trivalent ion (e.g. from  $\text{Eu}^{2+}$  to  $\text{Sm}^{3+}$  [94]) This reduces the efficiency of the IVCT active pairs, even more so as Yb concentration grows. These results also raise questions about the many other centers with anomalous emissions [26] that are usually assumed to be described by the ITE model. The above results do

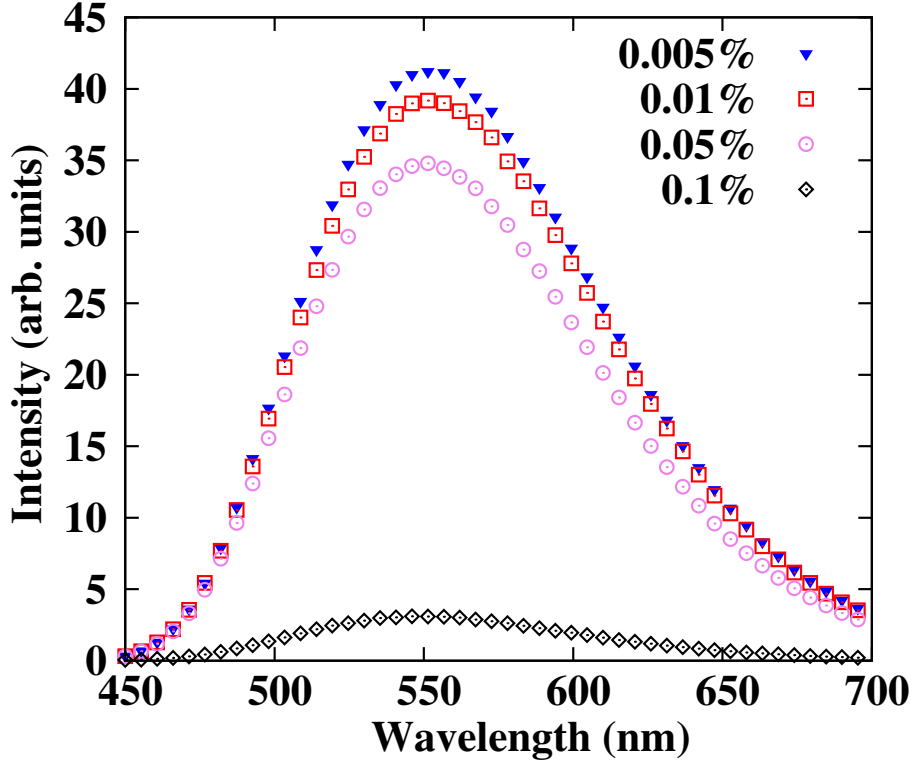


Figure 4.4: The anomalous emission spectra are plotted for the samples studied using XANES, keeping the geometry the same and the incident UV power level constant.

not invalidate the ITE model but rather point out the importance of measuring the concentration of the +2 ions in each sample and determining whether the anomalous emission intensity varies linearly with it. It may be that many of these systems, currently assumed to be described by the ITE model, do not have a linear relationship between emission intensity and Yb<sup>2+</sup> concentration; such cases may be better described by the IVCT model. Recent advances at synchrotrons in the last decade (higher x-ray intensity and better fluorescence detectors) now make it relatively straight forward to determine 2+/3+ ratios for rare earths at very low defect concentrations. In addition, since only a fraction of Yb<sup>2+</sup> ions are involved for CaF<sub>2</sub>:Yb, a new challenge arises in finding ways

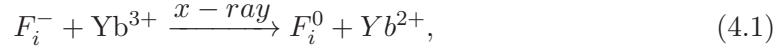
to probe different types of Yb sites and thus better test the IVCT model.

### 4.3 Role of Interstitial Fluorine Defects in Meta-stable Valence States

The interest in the trivalent lanthanide ions as solid-state laser activators that started in the sixties, rapidly expanded to the divalent lanthanides as it was shown that all ions from  $\text{Ce}^{3+}$  to  $\text{Yb}^{3+}$  could be partially reduced by  $\gamma$  rays when doped in suitable host crystals like  $\text{CaF}_2$ . [95] However, some drawbacks followed the initial efforts and Yb-doped  $\text{CaF}_2$  is an archetypical example: Whereas  $\text{CaF}_2:\text{Yb}^{3+}$  has become a very successful high-power diode-pumped IR laser near 1050 nm (broad band emission over 920-1100 nm), [96; 97; 98; 99]  $\text{CaF}_2:\text{Yb}^{2+}$  had to be ruled out as a laser because an anomalous emission (AE, a slow, extremely broad and red-shifted emission near 540 nm, previously associated with  $\text{Yb}^{2+}$ ) was found after UV and higher energy excitation. [100; 81; 99; 93] The physics behind the AE is not yet clear: A model to describe the AE in a variety of lanthanide doped crystals was developed in the 80's by McClure and others, [24; 25; 26] in which the optical center is thought to be an impurity trapped exciton (ITE) at the divalent lanthanide. However, *ab initio* calculations could not support the ITE hypothesis and showed that the AE can be identified with an  $\text{Yb}^{2+}/\text{Yb}^{3+}$  intervalence charge transfer (IVCT) luminescence instead. [88] The IVCT hypothesis is based on the  $2+/3+$  multivalent nature of Yb-doped  $\text{CaF}_2$  and draws a much more complex scenario for the AE than that of the ITE hypothesis.

In 4.2, the multivalent nature of Yb in  $\text{CaF}_2$  at low concentrations has been experimentally measured by extracting fractions of  $\text{Yb}^{2+}$ ,  $f(2+)$ , and  $\text{Yb}^{3+}$ ,  $f(3+)$ , from x-ray absorption near edge structure (XANES) analyses for different global Yb concentrations in  $\text{CaF}_2$ . [91; 101] The XANES experiments and corresponding UV-vis emission spectra have shown evidence that the ITE model of the AE breaks down in this system since the emission intensity is far from proportional to the  $\text{Yb}^{2+}$  concentration. [101] On the other hand, this trend is compatible with the IVCT luminescence interpretation if the  $\text{Yb}^{2+}$ -to- $\text{Yb}^{3+}$  electron transfer is more efficient when the  $\text{Yb}^{3+}$  centers are non-locally compensated, and hence cubic. [88; 94; 101]

In this work we study the complexity inherent in the multivalent nature of  $\text{CaF}_2\text{:Yb}$ . For concentrations above roughly 0.1%, most of the Yb is in a 3+ state which requires a charge compensating defect such as interstitial  $\text{F}_i^-$ , or  $\text{O}^{2-}$  (Our samples are grown in an O free environment with a slight excess of F, so no  $\text{O}^{2-}$  present). [102] There are several  $\text{Yb}^{3+}$  defects with different symmetries [90; 102; 103], depending on the type and location of these charge compensating defects. At lower concentrations ( $< 0.1\%$ ) a small fraction ( $< 30\%$ ) of Yb is in the  $\text{Yb}^{2+}$  state, and this fraction increases at lower Yb concentrations. The effects that x-ray exposure at different temperatures and subsequent thermal treatment have on the 2+/3+ valence conversion, the dopant local structures, and the Yb anomalous emission in dilute  $\text{CaF}_2\text{:Yb}$  single-crystals, are studied using a combination of XANES, x-ray absorption fine structure (EXAFS) and UV-vis absorption and emission spectra, plus *ab initio* calculations of the redox reaction:



whose relevance in x-ray induced reversible reduction of trivalent rare-earths was first proposed by Merz and Pershan. [104; 105] The results show a novel, huge and maximal reduction of Yb in  $CaF_2:0.01\%Yb$  samples from mostly 3+ to mostly 2+ after a long exposure at 200 K (from  $f(2+) = 0.3$  to  $f(2+) = 0.7$ ); however even after 200 minutes, the fraction  $f(2+)$  is still increasing slightly. Although the huge reduction is stable at low temperatures, reoxidation to the initial 2+/3+ fractions follows after warming to room temperature (hours) and rapidly (minutes) at 320 K. The ability to reversibly change the Yb valence from 3+ to 2+, provides a straightforward means of investigating changes in the local Yb–F bond lengths. As expected, the Yb–F bond is shorter when Yb is in the 3+ state, but there is little change in the second neighbor Yb–Ca distance. The AE of Yb that is observed in the as-grown samples is lost after the x-ray exposure and throughout the thermal reoxidation process, and, surprisingly, is only recovered after annealing at high temperature (900 K), even though annealing does not change the  $Yb^{2+}$  concentration nor the 2+/3+ fraction. The *ab initio* calculations reveal the existence of a critical distance between the dopant and the interstitial fluorine ions below which the  $F_i^0$ – $Yb^{2+}$  hole–electron recombine spontaneously and above which the  $F_i^0$ – $Yb^{2+}$  pair is metastable. This central feature, combined with temperature dependent  $F_i^0$  and  $F_i^-$  mobilities, provides a model for interpreting the complex experimental observations.

### 4.3.1 Calculations

The diabatic potential energy surfaces for  $F_i^- - Yb^{3+}$  and  $F_i^0 - Yb^{2+}$  pair states were computed using the results of independent embedded cluster calculations on cubic  $(F_iF_8)^{9-}$ ,  $(YbF_8)^{5-}$ ,  $(F_iF_8)^{8-}$ , and  $(YbF_8)^{6-}$  clusters in  $CaF_2$ ; the  $YbF_8$  clusters were calculated in Ref. [88]. The relativistic second-order Douglas-Kroll-Hess Hamiltonian [106; 107; 108] was used including all cluster electrons. Quantum mechanical *ab initio* embedding model potentials (AIMP) [109; 110] obtained for  $CaF_2$  [88] were used to represent the effects of all ions within a cube of  $7 \times 7 \times 7$  unit cells plus additional point charges [111] around the embedded clusters. The relativistic atomic natural orbital basis set (ANO-RCC) [112] F (14s9p4d3f2g) [5s4p3d] was used for all fluorines supplemented with Ca (20s15p) [1s1p] second-neighbor orthogonalization functions. [88] Multireference wave functions and energies were obtained in two steps of (i) complete active space self-consistent field (CASSCF), [113; 114; 115; 116; 117] and (ii) multi-state second-order perturbation method, (MS-CASPT2) calculations. [118; 119; 120; 121; 117] Spin-orbit coupling was included in the  $YbF_8$  clusters [88] and neglected in the  $F_iF_8$  clusters. More details are given in the Sec. 4.5.1. The suite of programs MOLCAS was used for all calculations. [122]



## 4.4 Results

### 4.4.1 XANES

In initial measurements on  $\text{CaF}_2\text{:Yb}$ , no obvious x-ray-induced valence change occurred in a few successive scans at 300 K during set-up of the fluorescence detector (See Experimental Section) or in scans at low temperatures below 80 K. A more careful evaluation later showed that small valence changes do occur at both 300 and 80 K after many scans, but the effects are small – a few percent – as observed earlier by Merz. [104] However in one run, multiple XANES scans were collected during cool-down and a large change in the edge was noted between about 250 and 150 K. Further investigation showed that a large valence reduction only occurs near 200 K and is extremely unusual. Reversible valence changes may occur when samples are damaged [123; 124]; also large increases in valence have been observed under high pressure[125], but not a valence decrease.

The normalized XANES at 200 K for 0.01% Yb are plotted in Fig. 4.5 for various x-ray exposure times (using multiple scans at the Yb  $\text{L}_{\text{III}}$  edge). Note that the “zero” minute scan is the start of these measurements but the sample already had some exposure and Yb is slightly reduced. Also note that the short time to scan the Yb XANES (3-4 min.) has little effect on the relative amplitudes of the 2+ and 3+ peaks. Once Yb has been mostly reduced to  $\text{Yb}^{2+}$  it is relatively stable at low temperatures for long periods of time – with small changes over 8 hours. In addition, a subsequent experiment showed that valence reduction is also achieved at 7940 eV, 1 keV below the

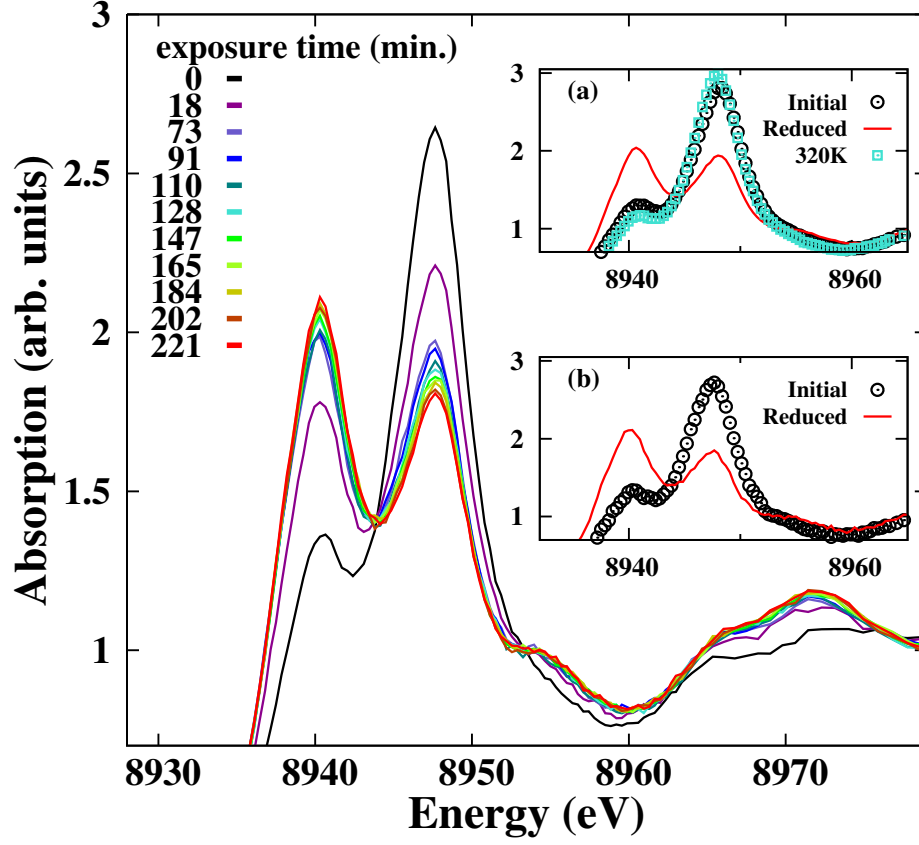


Figure 4.5: Evolution of Yb L<sub>III</sub> XANES spectra as a function of x-ray exposure time  $t$  for multiple scans at 200 K, for CaF<sub>2</sub>:Yb (.01%). At  $t = 0$ , the sample had some x-ray exposure and Yb was already slightly reduced. The 8942 eV peak is associated with Yb<sup>2+</sup> and the 8949 eV peak with Yb<sup>3+</sup>. Over  $\sim 3$  hrs, the valence changes from mostly 3+ to mostly 2+. Note also the changes in the EXAFS range above 8955 eV. Insets: a): XANES from a different experimental run; little x-ray exposure (open black circles), after x-ray exposure at 200 K ( $\sim 4$  hr - red) from multiple EXAFS scans at the Yb L<sub>III</sub>, and after heating to 320 K (green squares). The scan at 320 K has slightly less Yb<sup>2+</sup> than the initial scan. b): Similar changes when another fresh sample is exposed to x-rays at 7940 eV, 1 keV below the Yb L<sub>III</sub> edge. The same valence reduction occurs over a time period of 200 min. (red solid curve).

Yb L<sub>III</sub> edge (Fig. 4.5b) — i.e. no excitation of the Yb ions is required. Perhaps even more surprising is that this valence reduction is rapidly reversible (minutes) by heating to 320 K, — see Fig. 4.5a.

To determine the fractions ( $f(2+)$  and  $f(3+)$ ) of Yb<sup>2+</sup> and Yb<sup>3+</sup>, the XANES data were fit to a sum of two pseudo-Voigt peaks for the 2+ and 3+ lines plus a broadened step function for the main edge. From initial trials the average widths for both peaks and the step function were determined and then fixed in the final fits. No constraints on the integrated peak amplitudes for the two peaks were used. An example of a fit is shown in Fig. 4.6b and in more detail in Fig. 4.2. From the fit the areas under each peak were determined; initial fits showed that the sum of these two areas decreased slightly as  $f(2+)$  increased. Consequently, the matrix element for Yb<sup>2+</sup> is slightly smaller than for Yb<sup>3+</sup>, and an iterative fit described below was required to first determine the ratio of matrix elements and then extract  $f(2+)$ . We therefore used an iterative approach to obtain the fraction,  $f(2+)$ , of Yb<sup>2+</sup>. Since the change in total area is small we initially assumed that the matrix elements ( $p_i$ ) for both peaks were roughly equal and obtained the fraction  $f(2+)$  from  $I(2+)/[I(2+)+I(3+)]$  ( $I(2+)$  and  $I(3+)$  are the integrated intensities for the two peaks) to make a plot of total integrated intensity vs fraction of Yb<sup>2+</sup> (similar to that in Fig. 4.6). From a straight line plot through these data one can estimate the intensity change from pure Yb<sup>2+</sup> to pure Yb<sup>3+</sup> and hence the ratio of the matrix elements -  $R_{2-3} = p_{2+}/p_{3+}$ . If we define  $I'(2+) = I(2+)/R_{2-3}$ , then the fraction of Yb<sup>2+</sup> is given by  $I'(2+)/[I'(2+) + I(3+)]$ .

In Fig. 4.6a the sum of the integrated intensities is plotted as a function of

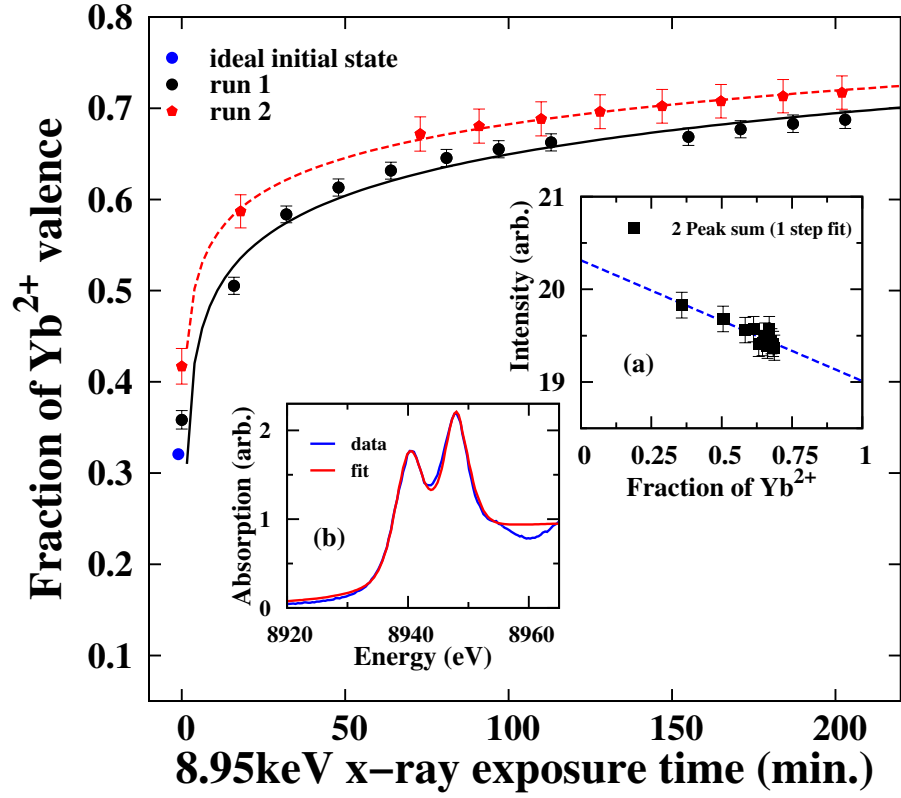


Figure 4.6: The fraction of  $\text{Yb}^{2+}$  ( $f(2+)$ ) as a function of x-ray exposure time at 200 K for .01% Yb;  $f(2+)$  changes from about  $\sim 0.3$  to 0.7, and varies roughly logarithmically with  $t$  (lines). Insets: a) Sum of the integrated areas for the two peaks as a function of  $\text{Yb}^{2+}$  fraction. This sum decreases slightly as the valence decreases from mostly  $3+$  to mostly  $2+$ . b) An example of a fit of the XANES to two pseudo-Voigt peaks plus a step function.

$f(2+)$  after the iterative procedure converged; extrapolating the straight line fit to pure  $\text{Yb}^{2+}$  and  $\text{Yb}^{3+}$  gives the relative ratio of the matrix elements  $p_i$  for  $\text{Yb}^{2+}$  and  $\text{Yb}^{3+}$ ;  $p_{2+}/p_{3+} \sim 0.93$ . This ratio was used in determining the fraction  $f(2+)$ , and is closer to 1.0 than the value,  $p_{2+}/p_{3+} = 0.65$ , used by Hughes-Currie *et al.*[126], based on results for  $\text{Eu}^{2+}$  and  $\text{Eu}^{3+}$  in solution[92]. It is not clear that solution results, for which the environment about the ion is quite different, are transferable to a solid.

In estimating errors for the two peaks in the XANES, the largest error was for the intensity  $I(2+)$  - about 2-3%. However we also found that the values of  $I(2+)$  and  $I(3+)$  are negatively correlated - i.e. if  $I(2+)$  is increased slightly,  $I(3+)$  decreases accordingly. To estimate the error on the sum,  $I(2+) + I(3+)$ , we varied  $I(2+)$  in small steps about its average value and calculated the sum in each case; the sum varies by less than 1% when the value of  $I(2+)$  deviated by 2-3%. Our resulting relative uncertainty on  $I(2+) + I(3+)$  is  $\sim 0.7\%$ . This relative uncertainty is further used when we propagate uncertainties to find the uncertainty on  $f(2+)$ . From the fits, the fractions  $f(2+)$  and  $f(3+)$  are extracted.

The fraction  $f(2+)$  is plotted as a function of time in Fig. 4.6 for two different experimental runs; it varies from roughly 0.3 to 0.7 for this sample. An important feature to note is that the region with reduced Yb valence is localized to the footprint region on the sample (1mmX7mm); if the sample is translated vertically 1 mm after valence reduction at 200K, the XANES is again the same as for the fresh sample. Also note that although the x-ray absorption length is quite long in  $\text{CaF}_2$  ( $\sim 40 \mu\text{m}$ ), the x-rays still do not penetrate through the  $\sim 1$  mm single crystal sample.

#### 4.4.2 EXAFS

The k-space data can be seen in Fig 4.7 and shows clear differences in the spectra, especially at low k. EXAFS  $r$ -space scans at the Yb L<sub>III</sub> edge, for data collected at 10 K, are shown in Fig. 4.8 for the two valence states. The data were reduced using RSXAP [23] and were Fourier Transformed (FT) to real-space using an FT window 3.5–10.0 Å<sup>-1</sup>, with a Gaussian window rounding of 0.3 Å<sup>-1</sup> (See [23]). These measurements probe the differences in local structure around Yb<sup>2+</sup> and Yb<sup>3+</sup> configurations, where Yb occupies a Ca site. In the CaF<sub>2</sub> structure there are 8 nearest neighbor F, 12 second neighbor Ca and 24 third neighbor F atoms about the Yb atoms. However the results for the first peak in Fig. 4.8 indicate a large increase in nearest neighbor Yb-F bond length for Yb<sup>2+</sup> (red; reduced sample) compared to Yb<sup>3+</sup> (black; fresh sample).

In order to investigate the large difference between the  $r$ -space EXAFS data before and after x-ray exposure, we fit the data[23] to a sum of theoretical EXAFS functions for the dominant scatter paths (calculated with FEFF7[127]) using the following model: two Yb-F peaks corresponding to pure Yb<sup>2+</sup> and Yb<sup>3+</sup> with  $r$ 's  $\sim$  2.40 and 2.25 Å; a Yb-Ca second neighbor peak near  $r = 3.867$  Å; a long third neighbor Yb-F peak near 4.53 Å, plus multi-scattering peaks in the range 3.5-4.5 Å.

The Yb EXAFS data are fit over the  $r$ -range 1.5-4.7 Å, to these three shells of neighbors but requires additional peaks. First, the data in 4.9 show clearly that the first neighbor peak Yb-F peak is at a shorter distance for the fresh sample (more Yb<sup>3+</sup>) compared to the reduced sample (more Yb<sup>2+</sup>); however, neither sample corresponds to

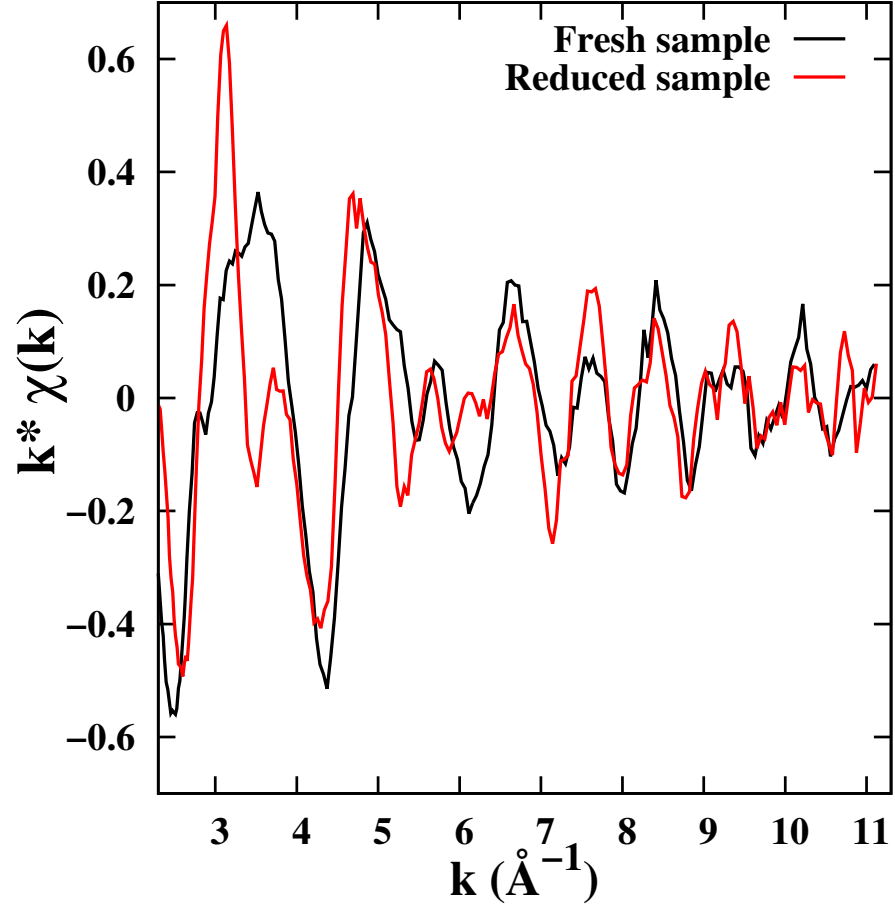


Figure 4.7: Examples of  $k$ -space data at the Yb  $L_{III}$  edge for the fresh sample, and after full valence reduction.

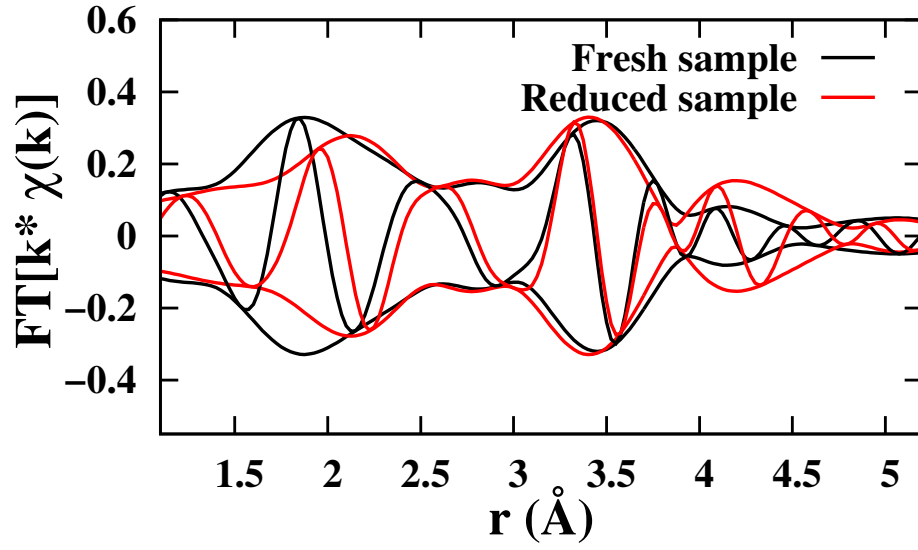


Figure 4.8: EXAFS  $r$ -space data at 10 K for a fresh sample, and after maximum valence reduction. Peaks in the EXAFS data correspond to shells of neighbors surrounding the Yb defect. The fast oscillatory function is the real part  $R$  of the Fourier transform (FT) while the amplitude functions are  $\pm\sqrt{R^2 + I^2}$ ;  $I$  is the imaginary part of the FT. There is a large increase in the distance ( $\sim 0.15$  Å) for the first peak near 1.9 Å, for the valence reduced sample (red trace), compared to the as-made sample (black). In contrast for the second, Yb-Ca peak, the pair distance changes very little upon valence reduction.



pure  $\text{Yb}^{2+}$  or  $\text{Yb}^{3+}$ , and two peaks  $\text{Yb}^{2+}\text{-F}$ ,  $\text{Yb}^{3+}\text{-F}$  are required. In addition three small multi-scattering (MS) peaks must be included at high  $r$ . Initial fits showed that the parameter  $S_0^2$  was close to 1.0 and it was fixed to this value in subsequent fits.

The fits for the fresh and fully reduced samples are shown in Fig. 4.9, and the fit parameters are tabulated in Table 4.1.

The fit for the first peak uses a sum of two identical standards, but at two different distances, to correspond to the  $\text{Yb}^{2+}\text{-F}$  and  $\text{Yb}^{3+}\text{-F}$  bonds; in the initial 2-peak fits of the Yb-F peak, the  $\text{Yb}^{3+}\text{-F}$  distance was obtained from the fresh sample while the  $\text{Yb}^{2+}\text{-F}$  distance was obtained from fits to the maximally reduced sample. In the final fits these two distances were fixed so we could calculate the fraction of each valence state using the ratio of the amplitude to that for Ca-F (8). In addition, starting with this fit, the constraints on the  $\text{Yb}^{2+}\text{-F}$  and  $\text{Yb}^{3+}\text{-F}$  bond lengths were released to check for stability;  $\Delta r < .01$  in all cases, implying a stable fit.

The ratio of amplitudes for the  $\text{Yb}^{2+}\text{-F}$  and  $\text{Yb}^{3+}\text{-F}$  pairs was allowed to vary but the sum of amplitudes was constrained to 8, the degeneracy of the nearest fluorine shell. The two fits can be found in Fig. 4.9; the corresponding table of fit parameters is given in Table 4.1.

The main results are that the closest Yb-F pair is contracted for  $\text{Yb}^{3+}$  and slightly expanded for  $\text{Yb}^{2+}$  relative to the Ca-F pair in the host material, with a total splitting of 0.15 Å, while the second neighbor pair (Yb-Ca) has almost the same distance for both valence states (difference  $\sim 0.02$  Å). Both results agree well with early estimations[24; 26] for the two valence states and with *ab initio* calculations [88] for

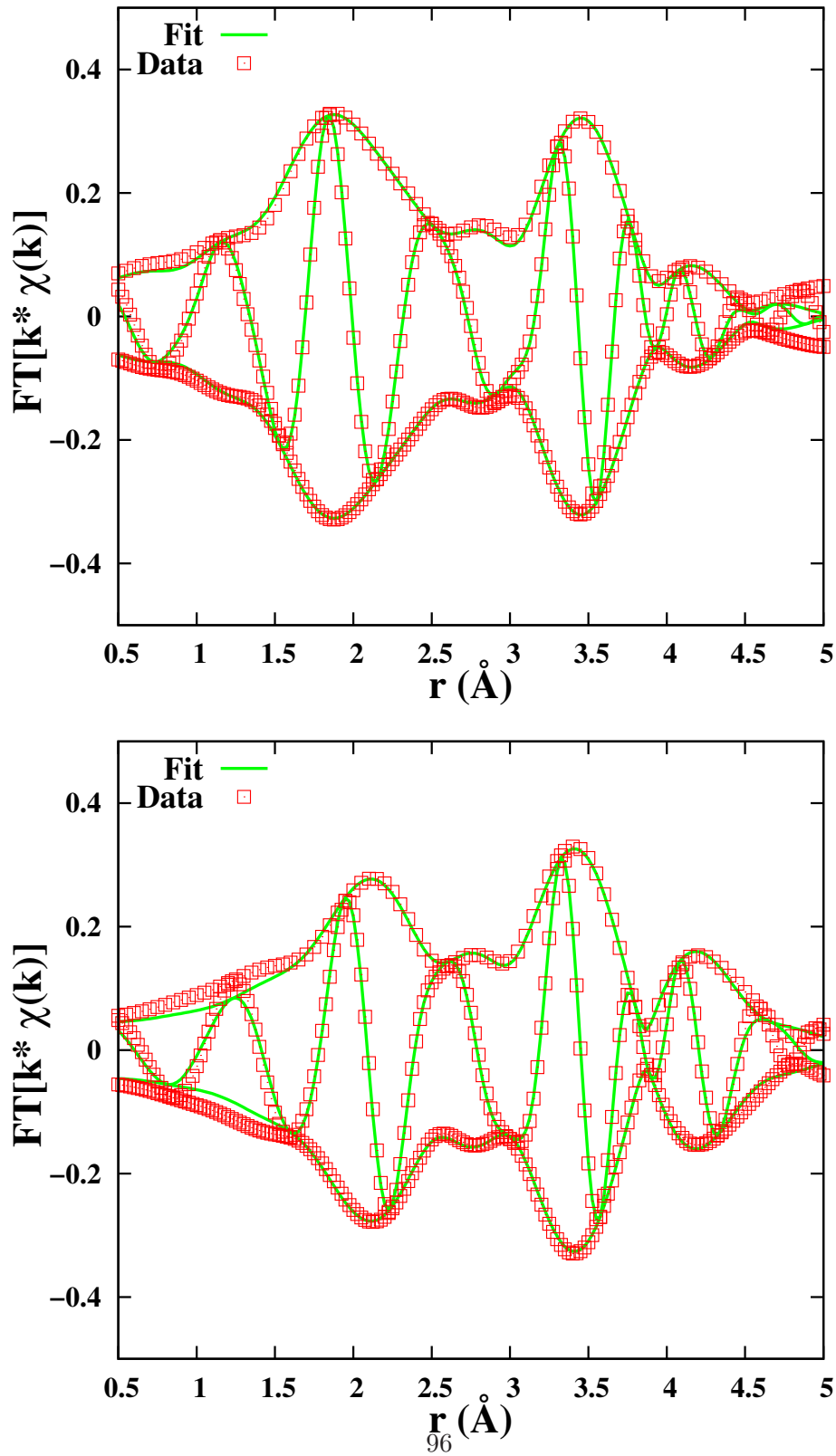


Figure 4.9: Fits of the real space data for the fresh sample (top) and the valence reduced sample (bottom) using the model discussed in the text. The Fourier transform window is  $3.5\text{-}10.0 \text{ \AA}^{-1}$ , with a  $0.3 \text{ \AA}^{-1}$  Gaussian rounding; the fitting range in  $r$ -space is  $1.5\text{-}4.7 \text{ \AA}$ .

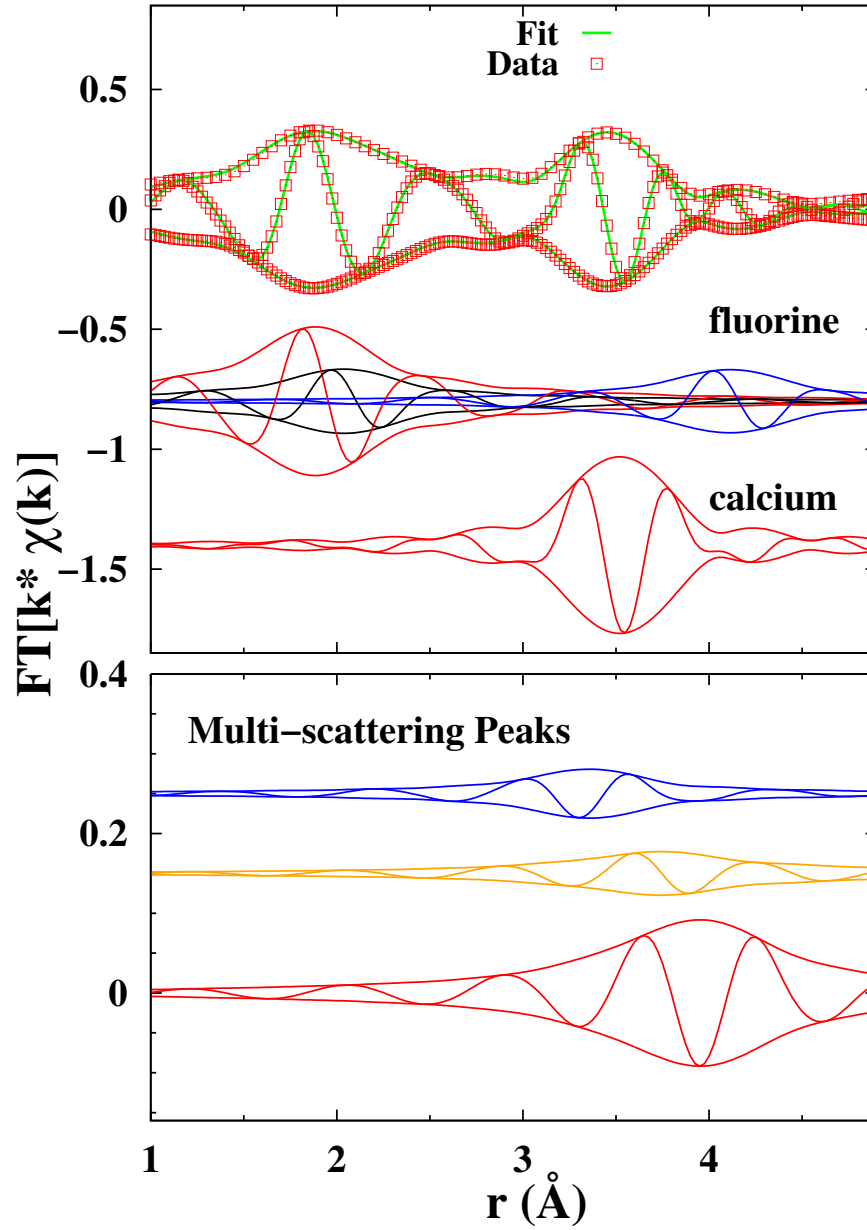


Figure 4.10: Top: full fit to fresh sample (green line) and data (red squares). The components for the fit are plotted individually below the total fit. The nearest neighbor F peak is fit using two Yb-F standards with different parameters (see Table 4.1); the larger near neighbor peak (red) corresponds to  $\text{Yb}^{3+}$  and has a shorter Yb-F bond length. At the bottom, the three multi-scattering (MS) peaks are offset and plotted on an expanded vertical scale (X 3.3); the lowest plot which peaks near 4  $\text{\AA}$  dominates the MS contributions and is nearly out of phase with the long Yb-F peak.

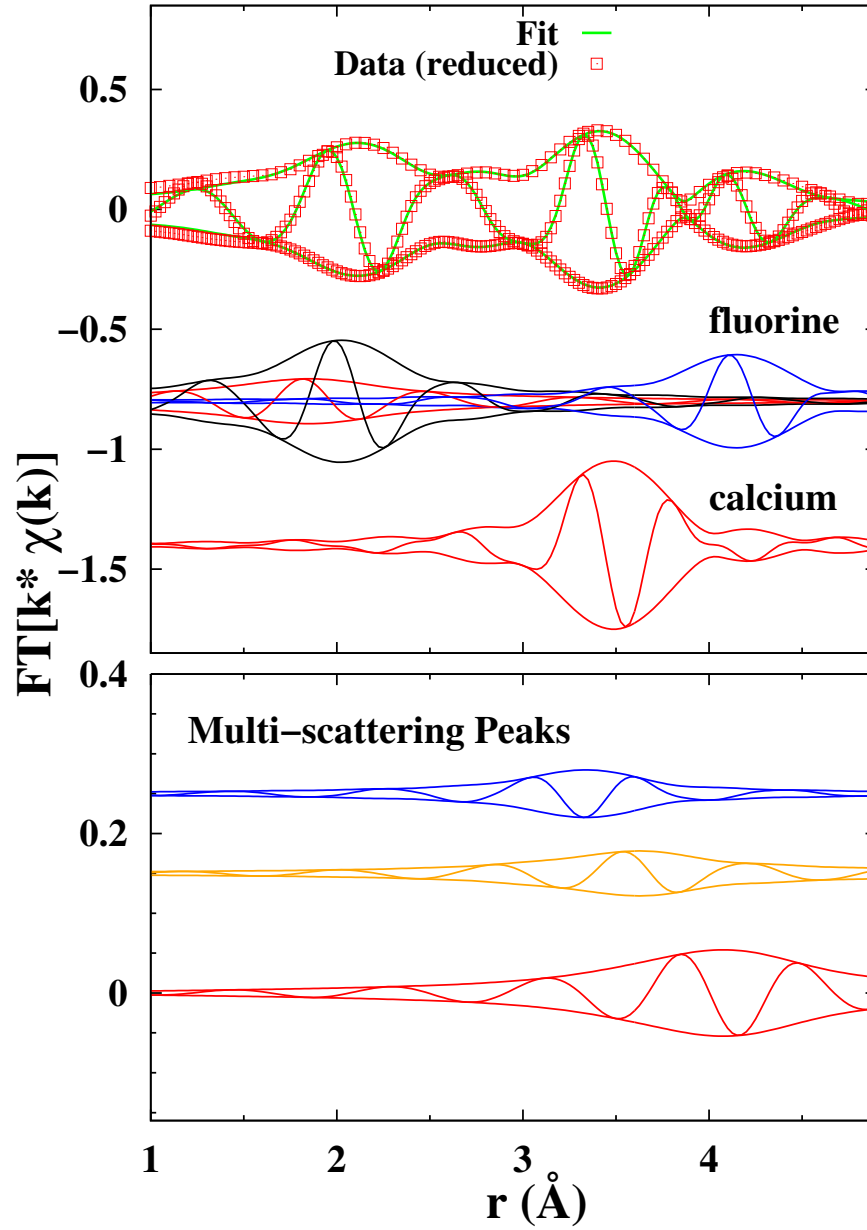


Figure 4.11: Top: full fit to the reduced sample (green line) and data (red squares). Components are plotted individually below the total fit. The main differences are the shift of the first peak to higher  $r$  (the larger near neighbor peak (black) corresponds to  $\text{Yb}^{2+}$ ) and the prominence of the second fluorine peak compared to the fresh sample fit. At the bottom, again on an expanded vertical scale (X 3.3), the small MS components are plotted. The farthest multi-scattering peak occurs at a higher  $r$  (peaks near  $4.15 \text{ \AA}$ ) compared to the fresh sample near  $4.0 \text{ \AA}$ , and is reduced in amplitude due to broadening.

which the bond lengths and their splitting are: 2.33 Å (Yb<sup>2+</sup>), 2.20 Å (Yb<sup>3+</sup>); and 0.13 Å respectively; the bond length of Yb<sup>2+</sup>-F becomes even closer to the EXAFS value if the representation of the second neighbors is improved: 2.37 Å. In addition, the third (Yb-F) neighbors are at the same distance as for CaF<sub>2</sub> when Yb is 2+, but for 3+, the further F atom is pulled in slightly, by  $\sim 0.04$  Å. A similar local distortion about a higher valence dopant was also observed in Zn doped LiNbO<sub>3</sub> [128]. From the EXAFS analysis, the fraction  $f(2+)$  in the as-made sample is about 0.30, while that for the strongly reduced sample is 0.70, very close to the fractions obtained from the XANES analysis above in Sec. 4.2, a remarkable and reassuring result.

In the fits typically 11- 13 parameters were varied depending on constraints used for the MS peaks.  $r$  and  $\sigma$  were varied for most peaks except for some MS peaks, plus the ratio of amplitudes for the Yb<sup>2+</sup>-F and Yb<sup>3+</sup>-F peaks. Using Stern's criteria[34] (FT range 3.5-10 Å<sup>-1</sup>; fit range, 1.5-4.7 Å) 2-4 degrees of freedom remain ; The results for  $r$  and  $\sigma$  for the Yb<sup>2+</sup>-F, Yb<sup>3+</sup>-F, and Yb-Ca peaks are weakly dependent on the MS peaks, but the latter are needed to get a good fit out to 4.7 Å. The uncertainties in Table 4.1 are derived from fitting real-space data from several scans of the fresh sample and the reduced sample, then calculating the standard deviation for each parameter; thus the uncertainties reflect the reproducibility of data.

The individual peaks are plotted in Fig. 4.10 and 4.11; the top of each figure shows the fit, while the middle plots shows the F and Ca neighbor peaks. The small MS peaks are plotted on an expanded scale (X 3.3) at the bottom of each figure.

Table 4.1: Results of the EXAFS fits for the fresh and valence reduced samples; Yb<sup>2+</sup>-F and Yb<sup>3+</sup>-F are for sites with valence 2+ and 3+ respectively. Fit range in  $r$ -space, 1.5-4.7 Å. The amplitude is the degeneracy for each shell, but is split for the first shell as a result of the two valence states.  $\sigma^2$  is the correlated Debye Waller factor where  $\sigma$  is the width of the pair distribution function. The errors show the reproducibility of the data in fits of multiple scans. Including systematic effects the errors for  $r$  are  $\sim 0.01$  Å for the first two neighbors, and up to .02 Å for further peaks. Due to the correlations between N and  $\sigma$ , systematic uncertainty is typically 10-15% for these parameters.  $S_0^2 = 1.0$ .

Pair	Fresh Sample			
	Amplitude	Host (Å)	Position (Å)	$\sigma^2$
Yb <sup>3+</sup> -F	5.6(1)	2.366	2.250(4)	0.0063(8)
Yb <sup>2+</sup> -F	2.4(1)	2.366	2.401(10)	0.0031(5)
Yb-Ca	12	3.863	3.890(2)	0.0037(2)
Yb-F	24	4.530	4.488(3)	0.0113(2)
	Reduced Sample			
	Amplitude	Host (Å)	Position(Å)	$\sigma^2$
Yb <sup>3+</sup> -F	2.4(3)	2.366	2.250(4)	0.0122(14)
Yb <sup>2+</sup> -F	5.6(3)	2.366	2.401(10)	0.0048(10)
Yb-Ca	12	3.863	3.874(5)	0.0031(4)
Yb-F	24	4.530	4.537(7)	0.0026(6)

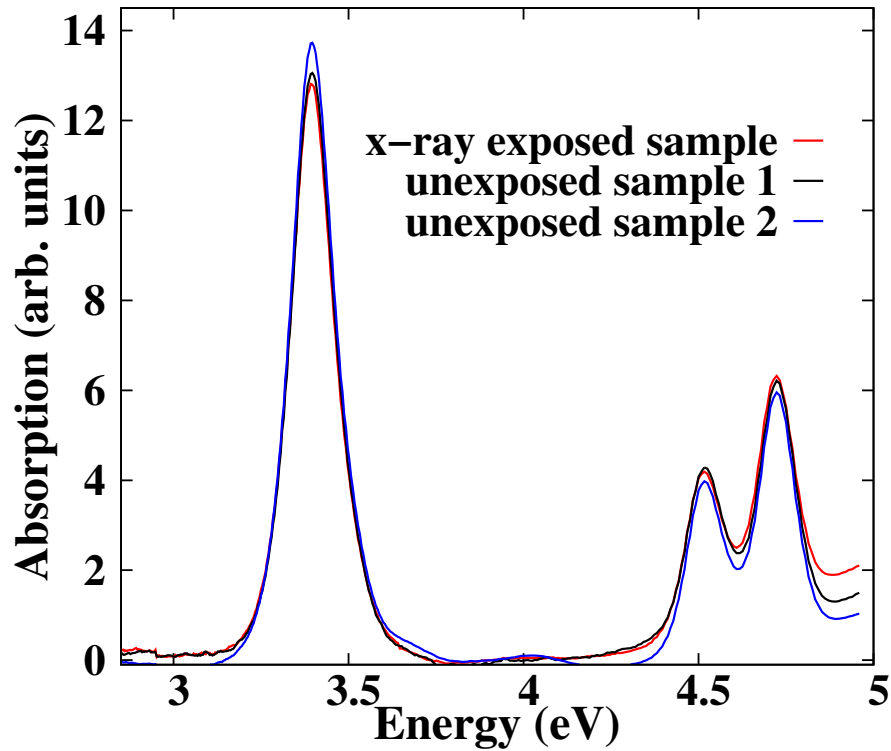


Figure 4.12: The normalized absorption spectra shows that the UV absorption centered at 3.4 eV (365 nm) remains relatively unchanged between the fresh samples and the x-ray exposed sample that no longer exhibits the anomalous luminescence.

#### 4.4.3 Anomalous Emission

Perhaps the most surprising result is that after extensive x-ray exposure plus heating to room temperature, no yellow-green anomalous emission was observed at 80 K in subsequent measurements, although the XANES were nearly identical to the unexposed sample, and the UV absorption did not change, see Fig. 4.12.

In a separate experiment (See Sec. 4.3) carried out 8 months after the last x-ray experiments, the emission spectra for two samples that had never been exposed to

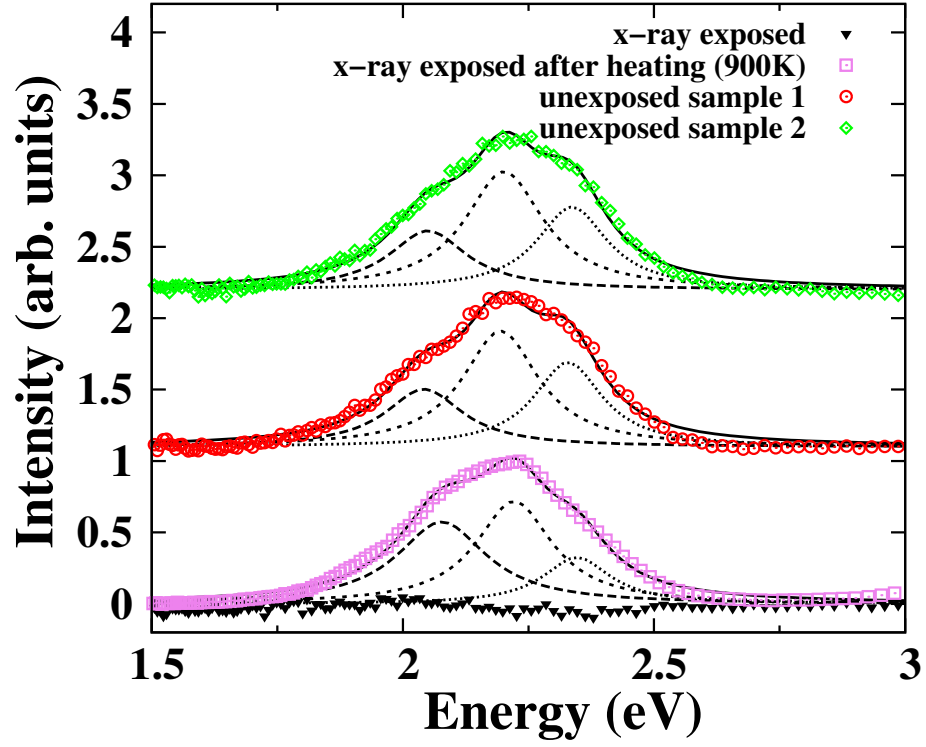


Figure 4.13: Normalized plots (80 K) of the yellow-green emission for two samples never exposed to x-rays (red circle; green diamond), the sample with extensive x-ray exposure (black, not normalized) and the x-ray exposed sample after annealing at 900 K (square purple symbols). The nearly flat (black) trace for the x-ray exposed sample has a remnant from the background subtraction. Each scan can be fit to a sum of three Lorentzians; importantly, the relative amplitudes of the components for the annealed sample are different.



x-rays were compared with that for the x-ray exposed sample. The results are plotted in Fig. 4.13; the anomalous emission spectra for the samples not exposed to x-rays were essentially identical, with a peak near 2.2 eV ( $\sim 560$  nm), but the x-ray exposed sample had no clear emission peak, only a remnant of the background subtraction remains. Upon annealing at 900 K (cooled slowly for  $\sim 2$  hours), the yellow green emission was again observed as shown by the square symbols on Fig. 4.13, but the shape of the spectrum has changed. Each scan can be fit to a sum of three Lorentzians as shown in Fig. 4.13; the relative weights of these three components are different for the annealed sample, suggesting a distribution of slightly different emission centers and likely different local environments.

## 4.5 Experimental methods

The  $\text{CaF}_2\text{:Yb}$  samples were grown as described in [91]. For the 0.1 and 0.05 % Yb samples, a small piece was powdered and mounted on scotch tape as described in [129]; the XANES and EXAFS were collected in fluorescence mode on beamline 4-1 at the Stanford Synchrotron Radiation Lightsource (SSRL) using a small Ge fluorescence detector (16 elements). For 0.01% Yb, a thin, polished, single crystal was used, together with a 100 element fluorescence detector on the high x-ray intensity beamline 11-2 at SSRL. Such a transparent sample was needed to also monitor induced anomalous emission. Because of Bragg reflections from the single crystal, some detector channels had large (Bragg) spikes at some energies in a scan and these channels had to be

removed. Since Bragg peaks are sensitive to the orientation of the single crystal, the appropriate channels had to be determined each time a sample was mounted. Typically 50-70 channels had no Bragg spikes and were used for the XANES (and EXAFS) data collection. EXAFS and XANES data in Sec. 4.3 of the Yb L<sub>III</sub> edge were collected on beamline 11-2 at SSRL using an Oxford helium flow cryostat, out to  $k = 11 \text{ \AA}^{-1}$ . The slits were  $1.0 \text{ mm} \times 5.0 \text{ mm}$ , providing an energy resolution of 1.3 eV. The anomalous emission experiments (Fig. 4.4) were carried out at the University of Canterbury NZ and the methods and apparatus are described in Refs. [85; 87].

The data were reduced and analyzed using RSXAP[23] which follows standard procedures; examples of the  $k$ -space data are shown in Fig. 4.7. These data were Fourier Transformed (FT) to real-space using an FT window  $3.5\text{--}10.0 \text{ \AA}^{-1}$ , with a Gaussian window rounding of  $0.3 \text{ \AA}^{-1}$ . UV excitation at SSRL used an LED source at 365 nm (near the top of the UV absorption peak); The UV source was not focused and provided a wide beam about 10 mm in diameter. The anomalous emission at SSRL was monitored using a Ocean Optics USB spectrometer.

#### 4.5.1 Theoretical Calculations and $F_i$ Dynamics

$\text{CaF}_2:\text{Yb}$

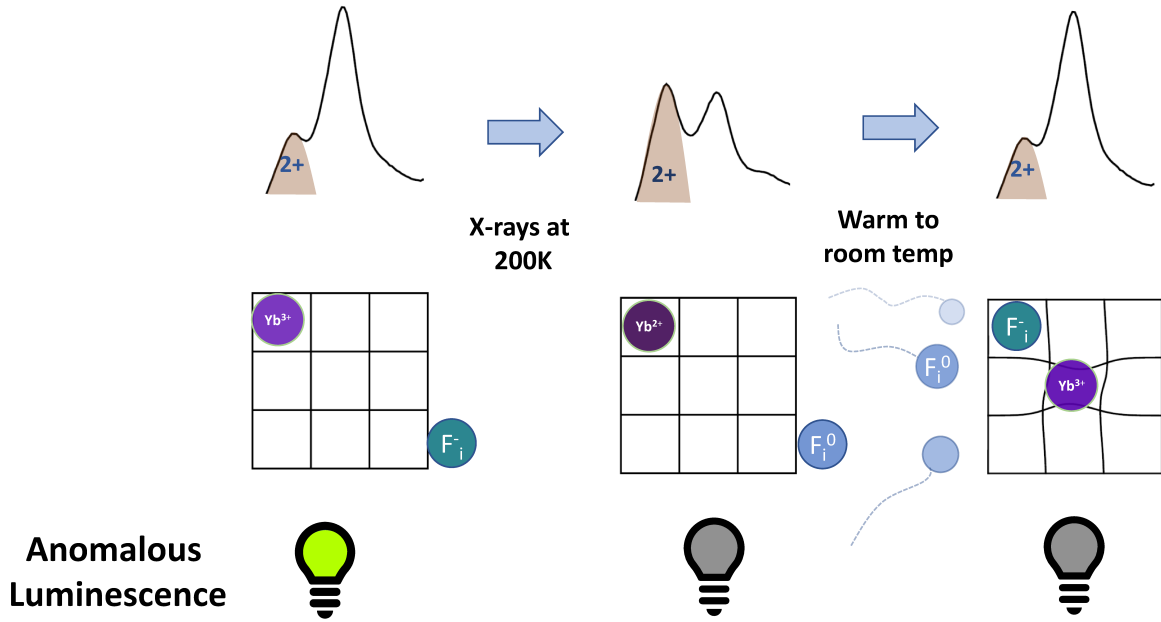


Figure 4.14: A diagram of different meta-stable states observed in  $\text{CaF}_2:\text{Yb}(.01\ \%)$ . As-made sample exhibits anomalous luminescence (AE) and most Yb in  $3+$  state with a non-local charge compensating  $F_i^-$ . X-ray exposure at 200K excites interstitial  $F^-$  resulting in recombination and an increased amount of  $\text{Yb}^{2+}$  while quenching AE. Warming to room temperature increases  $F_i^0$  mobility and locally compensated  $\text{Yb}^{3+}$  complexes emerge, but AE does not return.

To begin to understand this very complex behavior, *ab initio* calculations have been carried out by Zoila Barandiarán and Luis Seijo at the Departamento de Química, Instituto Universitario de Ciencia de Materiales Nicolás Cabrera, and Con-

densed Matter Physics Center (IFIMAC), Universidad Autónoma de Madrid, with charge-compensating interstitial F ions at various distances from an  $\text{Yb}^{3+}$  dopant. An overview schematic of the different metastable states can be found in Fig. 4.14 and the first few interstitial sites are illustrated in Fig. 4.15.

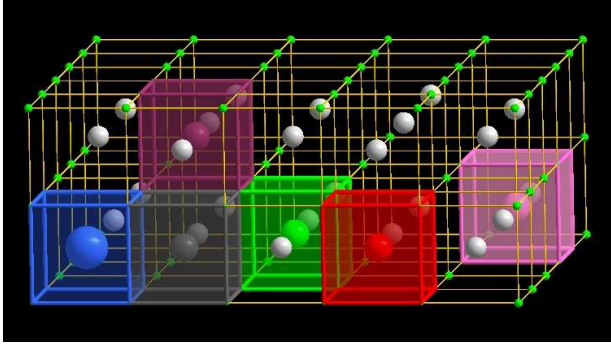


Figure 4.15: Partial representation of a fluorite crystal structure surrounding one Yb dopant ion in blue, located in the  $\text{YbF}_8$  cube that is shaded in blue. Some of the  $\text{Ca}^{2+}$  ions located at the center of every other cube are plotted in light grey; crystal fluoride ions in green are located at the vertices of all cubes. Five cubes around interstices are shaded in colors (dark grey, violet, green, red, and magenta); at their center an interstitial fluoride ion  $\text{F}_i^-$  is indicated in the same color. The distance from the Yb ion (in blue) and each of the interstitial fluorides plotted are:  $d_{\text{F}_i-\text{Yb}} = 2.73$  (dark grey), 4.73 (violet), 6.11 (green), 8.19 (red), and 13.7 Å (magenta). Each *ab initio* calculation comprises the  $\text{YbF}_8$  cluster and one of the five  $\text{F}_i\text{F}_8$  cubes embedded in the fluorite crystal. See text and Figs. 4.16 for details.

The results of these calculations are plotted in Fig. 4.16 for the electron transfer reaction between interstitial fluorine and ytterbium ions (Eq. 4.1). They have considered six interstitial sites around an  $\text{Yb}^{3+}$  ion (See Fig. 4.15) and calculated the energies at each of these different  $\text{F}_i\text{-Yb}$  distances ( $d_{\text{F}_i-\text{Yb}}$ ) using wave function-based embedded cluster methods of quantum chemistry.

The following can be deduced from them.

(A) The dopant-compensator distance determines the stability of the x-ray

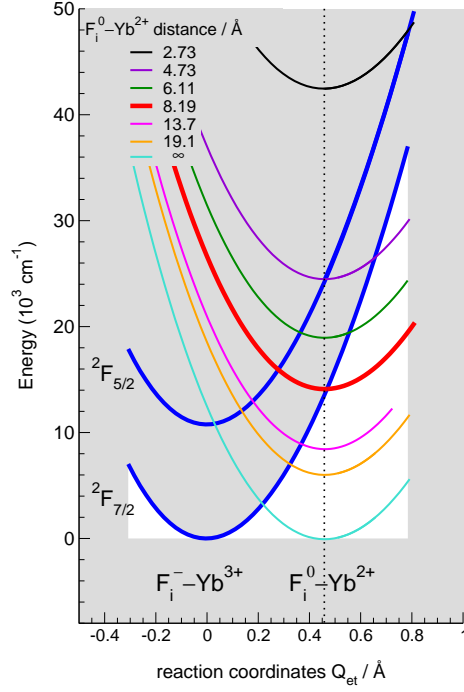
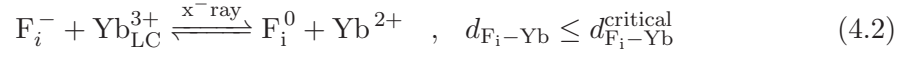


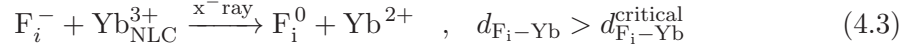
Figure 4.16: Diabatic configuration coordinate energy diagrams for  $F_i^-/Yb^{3+}$  electron transfer in  $CaF_2$  at different  $F_i-Yb$  distances are plotted together in this figure. The diagrams show the existence of a critical distance  $d_{F_i-Yb}^{critical} \simeq 8.19 \text{ \AA}$ . For  $d_{F_i-Yb} < d_{F_i-Yb}^{critical}$  the  $F_i^0-Yb^{2+}$  minima lie on the left and above the  $F_i^-Yb^{3+}$  ground state in the grey region, hence the hole-electron  $F_i^0-Yb^{2+}$  pair spontaneously recombines; for  $d_{F_i-Yb} > d_{F_i-Yb}^{critical}$  they lie on the right and below the  $F_i^-Yb^{3+}$  ground state curve, in the white region, hence the  $F_i^0-Yb^{2+}$  hole-electron pair state is metastable. Note that when  $F_i^0$  moves away from (or towards)  $Yb^{2+}$  after reduction, the energy curve of the  $F_i^0-Yb^{2+}$  hole-electron pair shifts down (or up). The  $F_i^0-Yb^{2+}$  ground state minima are connected with a vertical dotted line for comparisons. At very large separations the energy for the  $F_i^0-Yb^{2+}$  hole-electron pair is only slightly higher than that for the  $F_i^-Yb^{3+}$  ground state and is not seen on this scale.

induced reduction.

The diabatic configuration coordinate energy diagrams of Fig. 4.16 show there is a critical  $F_i$ -Yb distance ( $d_{F_i-Yb}^{critical} \simeq 8.19 \text{ \AA}$ ) up to which the backwards oxidation of Yb is spontaneous ( $F_i^0$ -Yb $^{2+}$  energy curves above the red line with energy minima are above the blue line for  $^2F_{7/2}$ ) and beyond which the x-ray induced reduction is metastable ( $F_i^0$ -Yb $^{2+}$  energy curves below the red line for which the energy minima are below the blue line for  $^2F_{7/2}$ ). Then, one can write for the locally compensated Yb $_{LC}^{3+}$ :



and for the non-locally compensated Yb $_{NLC}^{3+}$ :



This central message is compatible with the diabatic approximation; in other words, the message should hold even if the diabatic approximation were overcome.

This result is in agreement with extensive experimental data that suggest that only those rare-earth trivalent ions in cubic sites are reduced to the divalent state in CaF $_2$  doped crystals. [104]

(B) There is a temperature,  $T_{Red}$ , at which x-ray induced reduction is maximal.

In order to understand the effects of x-ray exposure at different temperatures on Yb $_{LC}^{3+}$  and Yb $_{NLC}^{3+}$  centers, we combine now the results of the *ab initio* calculations with the expected temperature dependent mobility of  $F_i^0$  holes through the crystal, inferred from experiments [104], [130], and references therein.

(i)  $\text{Yb}_{\text{LC}}^{3+}$  centers at temperatures below a threshold,  $T \leq T_{\text{Red}}$ : If, during the x-ray induced reduction process (forward reaction of Eq. 4.2), some  $\text{F}_i^0$  move away from  $\text{Yb}^{2+}$  surpassing the critical distance  $d_{\text{F}_i-\text{Yb}}^{\text{critical}}$ , their corresponding  $\text{F}_i^0-\text{Yb}^{2+}$  hole-electron pairs would be stabilized at an energy curve lower than the red one. However, those staying close to  $\text{Yb}^{2+}$  ions will re-oxidize back to  $\text{Yb}_{\text{LC}}^{3+}$ . Thus, the initial  $\text{Yb}_{\text{LC}}^{3+}$  centers would be partly reduced and partly reoxidized, leading to the following  $\text{Yb}^{3+}$  defects balance:

$$\{\text{Yb}_{\text{LC}}^{3+}\}_{T \leq T_{\text{Red}}} \xrightarrow{\text{x-ray}} \{\text{Yb}_{\text{LC}}^{3+} + \text{Yb}^{2+}\}_{T \leq T_{\text{Red}}} \quad (4.4)$$

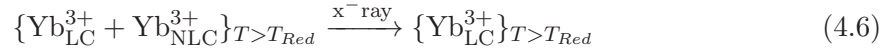
where the defect term on the left refers to the sample before x-ray exposure.

(ii)  $\text{Yb}_{\text{NLC}}^{3+}$  centers at temperatures below a threshold,  $T \leq T_{\text{Red}}$ : Correspondingly, if during the x-ray reduction of Eq. 3, some of the  $\text{F}_i^0$  move closer to the  $\text{Yb}^{2+}$  ions and reach the  $d_{\text{F}_i-\text{Yb}} \leq d_{\text{F}_i-\text{Yb}}^{\text{critical}}$  range, the energies of their corresponding  $\text{F}_i^0-\text{Yb}^{2+}$  pairs would be above the red energy curve, so that a spontaneous non-radiative electron-hole recombination would re-oxidize those divalent Yb ions to  $\text{Yb}_{\text{LC}}^{3+}$ . The remaining  $\text{Yb}^{2+}$  ions would not have any  $\text{F}_i^0$  sufficiently close, and would remain stable. Thus, the initially cubic  $\text{Yb}_{\text{NLC}}^{3+}$  centers would be partly reduced and partly distorted by local compensation:

$$\{\text{Yb}_{\text{NLC}}^{3+}\}_{T \leq T_{\text{Red}}} \xrightarrow{\text{x-ray}} \{\text{Yb}_{\text{LC}}^{3+} + \text{Yb}^{2+}\}_{T \leq T_{\text{Red}}} \quad (4.5)$$

Altogether, the outcomes of Eqs. 4.4 and 4.5 are: (a) an x-ray induced Yb reduction and (b) a decrease of cubic, non-locally compensated  $\text{Yb}^{3+}$  centers.

However, given that the  $F_i^0$  mobility increases with temperature, the net effects of Yb reduction and decrease of  $Yb_{NLC}^{3+}$  cubic centers should strengthen at first ( $T < T_{Red}$ ), reach a maximum at a given temperature ( $T = T_{Red}$ ), and diminish again as  $T$  increases further ( $T > T_{Red}$ ). The latter corresponds to temperatures where the  $F_i^0$  mobility is high enough so that  $F_i^0$  would always get close to some other  $Yb^{2+}$  center to recombine, thus making reoxidation to locally-compensated  $Yb_{LC}^{3+}$  most likely:



All this is consistent with the huge reduction observed in the XANES spectra from  $f(2+) = 0.3$  to  $f(2+) = 0.7$  for exposure at 200 K ( $T_{Red} = 200$  K) and the small changes in the XANES spectra upon exposures below 80 K ( $T < T_{Red}$ ) and at 300 K ( $T > T_{Red}$ ). This also explains the small reduction achieved at 77 K by Merz and Pershan ( $T < T_{Red}$ ). [104]

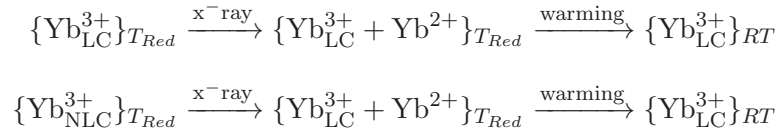
It should be noted that x-ray induced defects in  $CaF_2$  could make net x-ray induced ytterbium reduction even more unlikely at low temperatures: Görlich *et al.* [130] have suggested that x-ray exposure favors an increase in the concentration of Frenkel defects (anion vacancies plus interstitial fluoride ions) and ionization of interstitial and crystal fluoride ions, which are less mobile the lower the temperature is. This could affect the balance we have just discussed making the reoxidation of the  $Yb^{2+}$  produced by x-rays (Eq. 4.3) more likely in the presence of nearby meta-stable  $F_i^0$  or  $F^0$  centers.

(C) Both x-ray exposure and warming after x-ray exposure, enhance local compensation and quench Yb anomalous emission:



The decrease in the number of cubic centers by x-ray exposure, expressed in Eq. 4.5 for  $T = T_{Red}$  should result in quenching of Yb AE as long as the AE is interpreted as a radiative electron transfer between  $\text{Yb}^{2+}$  and a cubic, non-locally compensated  $\text{Yb}_{\text{NLC}}^{3+}$  center, i.e. as  $\text{Yb}^{2+}/\text{Yb}_{\text{NLC}}^{3+}$  IVCT luminescence. This is consistent with the experimental fact that the AE was no longer observed at low temperatures after x-ray exposure at 200 K even though the number of  $\text{Yb}^{2+}$  ions nearly doubled by the x-ray induced reduction (Fig. 4.13).

Besides, warming to room temperature (RT) after exposure at  $T_{Red}=200$  K should increase  $F_i^0$  mobility, favour their encounters with  $\text{Yb}^{2+}$  and reoxidation to locally compensated  $\text{Yb}_{\text{LC}}^{3+}$ :

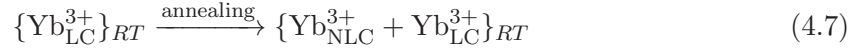


(Note this is basically the same scenario as discussed above for exposures at  $T > T_{Red}$ ; Eq. 4.6.) This means, again, that the AE should be quenched if it is an  $\text{Yb}^{2+}/\text{Yb}_{\text{NLC}}^{3+}$  IVCT luminescence. This is consistent with the facts that after warming to 320 K reoxidation was observed –from  $f(2+)=0.7$  back to 0.3– but the AE, observable in the initial unexposed sample, was not recovered.

(D) Annealing at high temperatures increases non-local compensation and recovers Yb anomalous emission:

It has been shown that annealing at 1000–1200°C followed by rapid quenching to room temperature induces full cubic non-local charge compensation of trivalent lan-

thanides in fluorite [131; 94] and fluorite-type crystals; [132] this symmetrizing effect is attenuated with smaller annealing temperatures and smaller cooling gradients, in which case conversion to cubic centers would be only partial: [131; 132]



Thus, the reappearance of some  $\text{Yb}_{\text{NLC}}^{3+}$  cubic centers should result in recovery of the  $\text{Yb}^{2+}/\text{Yb}_{\text{NLC}}^{3+}$  IVCT luminescence, in agreement with the experimentally observed recovery of the AE after annealing at 900 K ( $\sim 600^\circ\text{C}$ ) plus cooling to room temperature over  $\sim 2$  hours.

Obviously, the redistributions associated with the mobility of interstitial  $\text{F}_i^0$  and  $\text{F}_i^-$  centers along the whole process of exposure plus heating, mean that the final and initial  $\text{Yb}_{\text{LC}}^{3+}$  and  $\text{Yb}_{\text{NLC}}^{3+}$  distributions are not identical. This is consistent with the slight change in shape of the anomalous emission band recovered after annealing (Fig. 4.13).

(E) The x-ray induced reversible reduction of  $\text{Eu}^{3+}$  and  $\text{Yb}^{3+}$  should be very similar.

The energy difference between the  $\text{F}_i^- - \text{Yb}^{3+}$  and  $\text{F}_i^0 - \text{Yb}^{2+}$  ground state minima plotted in Fig. 4.16 for different  $d_{\text{F}_i - \text{Yb}}$  distances depends on (minus) the ionization potential of  $\text{Yb}^{2+}$  in  $\text{CaF}_2$ . [133; 134] The ionization potentials of  $\text{Yb}^{2+}$  and  $\text{Eu}^{2+}$  are known to differ only by  $\sim 1000 \text{ cm}^{-1}$ , [135; 136; 137] therefore, the  $\text{F}_i^-/\text{Yb}^{3+}$  and  $\text{F}_i^-/\text{Eu}^{3+}$  configuration coordinate energy diagrams should be basically the same, as in Fig. 4.16, and the maximal and huge reversible reduction observed in  $\text{CaF}_2:\text{Yb}$  should

be also expected for  $\text{CaF}_2\text{:Eu}$ .

## 4.6 Conclusion

Lanthanide doped materials are utilized for a variety of applications in industry and medicine. Due to their long lifetime emissions, the lanthanide activating ions are used for imaging protein complexes, and are also a strong candidate for imaging inside body tissue via up-conversion. In another application, Yb doped  $\text{CaF}_2$  shows great potential as a medium for short-pulse high energy lasing. This is in part a consequence of its broad emission band, and the ease of growing a large crystal; however  $\text{Yb}^{2+}$  impurities must be minimized. Further important applications are yet to be realized, and doing so depends on understanding the various properties of fluorescing lanthanide centers.

We have found strong evidence against the currently accepted Impurity Trapped Exciton (ITE) model for the anomalous luminescence observed in  $\text{CaF}_2\text{:Yb}$ , with relevance to many other similar systems. The ITE model predicts that under pulsed UV excitation, transient local structure changes should be induced around the Yb atoms. These changes would result in time dependent EXAFS (10 ms time scale) - which we can now probe - but no evidence for any local structure change induced by UV was found. That lead to the current study of the switching of anomalous luminescence with x-ray exposure. Carefully exploring the different metastable states of this rare-earth doped fluorite leads us to expect complexities in many similar systems that are exploited for

lasing applications. Are there other unforeseen uses of these subtle variety of states?

## Chapter 5

# Doped Lithium Niobate

This chapter is an adaptation and merging of the following two papers [138; 139]:

F. Bridges, C. MacKeen, and L. Kovacs, “No difference in local structure about a Zn dopant for congruent and stoichiometric  $\text{LiNbO}_3$ ”, *Phys.Rev. B* 94, 014101 (2016).

C. MacKeen, F. Bridges, L. Kovacs, and J. Castillo-Torres, “Substitution of Er, In, and Hf in  $\text{LiNbO}_3$ : Evidence for multiple defect distributions about dopant sites”, *Phys.Rev.Mater.* 2, 093602 (2018).

### 5.1 Lithium Niobate Doped with of Zinc

$\text{LiNbO}_3$  (LNO) has a range of very interesting behaviors,[140; 141; 142; 143] including in particular a number of important non-linear optical properties[144; 145; 146; 147] such as photorefraction and second harmonic generation, which lead to a range of applications. In addition, LNO materials can be grown in two different forms

- congruent LNO (cLNO, approximately  $\text{Li}_{0.95}\text{Nb}_{1.01}\text{O}_3$ ) and stoichiometric (sLNO), which can have significantly different properties[148; 146]; however the composition can vary between these two cases. The most common form is congruent LNO, which has excess Nb plus vacancies on the Li sites; it has been studied for decades and is used in a range of optical applications. In contrast stoichiometric LNO (sLNO) has only been synthesized relatively recently and its optical properties can differ significantly from cLNO as discussed in a recent review article[146]. For example, sLNO is more optical damage resistant (ODR) than cLNO, and the threshold concentration for divalent ions that enhance ODR is much lower — close to 0 mol%, in contrast to the threshold for cLNO,  $\sim 5$  mol%[146]. Also, Raman spectra are very different for the two types of crystals, and similarly for  $\text{OH}^-$  vibration modes from very dilute  $\text{OH}^-$  impurities. For the latter, a sharp narrow line is observed in sLNO, but a very broad band for cLNO. Finally, sLNO is much harder to dope with defect atoms than cLNO.

For harmonic generation, the photorefractive effect needs to be suppressed to reduce optical damage when high light intensity is used;[27; 28] this is achieved in LNO by adding dopants such as Mg, Zn, In, etc. Recently Hf at concentrations above 3 mol%[147] also greatly reduces the optical damage. For optical waveguide applications,  $\text{Ti}^{4+}$  is added - often via diffusion at high T (1100 °C, 50 hrs), to improve the performance[149; 150], while Fe[149; 150] and Bi[151; 152] at low concentrations improve the photorefractive index[145]. In the last decade there are also a large number of papers on co-doped LNO (2 or more dopants) in which the doubly or triply doped materials have improved properties. However for most systems, there is little direct

evidence as to the substitution site for a defect, and there is some evidence that there may be different configurations for a given dopant (different site occupations and/or different distributions of charge compensating defects) that lead to slightly different properties, as for  $\text{LiNbO}_3\text{:Ti}$ [149]. Here “defect” can refer to vacancies (e.g. a Li vacancy,  $V_{\text{Li}}$ ), a dopant atom on a metal site (e.g. In on a Li site,  $\text{In}_{\text{Li}}$ ), or anti-site defects (e.g. Nb on a Li site,  $\text{Nb}_{\text{Li}}$ ).

Consequently a very important characterization of doped LNO is the site occupation of a range of dopants with different valences in both sLNO and cLNO. Such information is needed for modeling how dopants modify the optical properties. In general the dopants used have a different valence from  $\text{Li}^+$  and  $\text{Nb}^{5+}$  and open questions remain as to which site(s) the dopant occupies, does the substitution site change with concentration or sample growth, and where the charge compensating defects are located. For congruent  $\text{LiNbO}_3$ , Xu *et al.* [30] have calculated defect energies for a range of dopants but did not consider Zn explicitly; for other 2+ dopants, they found the lowest energy in congruent material to be for substitution on the Li site with neighboring Li vacancies —  $\text{Zn}_{\text{Li}} + V_{\text{Li}}$ ; however they did not consider a threshold dopant concentration. For material close to stoichiometric compositions, impurities may go onto both Li and Nb sites, but including the effects of intrinsic defects they concluded that the concentration of impurities on the Nb site would be negligible for stoichiometric material. In contrast for stoichiometric LNO (sLNO) at low Zn concentrations, Araujo *et al.* [29] found the lowest energy with the self compensating defect being Zn on a Nb site: i.e.  $3\text{Zn}_{\text{Li}} + \text{Zn}_{\text{Nb}}$ . Thus it is important to investigate the local structure about a given

dopant atom in both types of crystals, and for different concentrations. Note also that the divalent Mg dopant is thought to change its environment above the photorefractive threshold, and this strongly depends on the stoichiometry. Below threshold Mg goes to the Li site, while above threshold it goes to the Nb site[153; 154; 155]. Xu *et al.* [30] arrived at a similar conclusion for Mg dopants from DFT calculations, with the dopant site depending on the chemical potential for Mg. In general Xu *et al.* [30] find that when the chemical potential corresponds to the stoichiometric material, the defect formation energies become positive, which leads to very low defect concentrations.

In an earlier study[128], we investigated the local structure in Zn doped congruent materials for a range of higher Zn concentrations using the EXAFS (extended x-ray absorption fine structure technique, at both the Zn and Nb K edges. The environment about Zn was nearly identical for all Zn concentrations with a small increase in local disorder for the higher concentration samples. Detailed fits found that a Li site substitution model fit very well, with a small contraction of the O neighbors (compared to a Li site) and a slight expansion of the Nb shells. The signature of substitution on a Nb site would be a large (6 neighbors) Zn-Nb peak near 3.76 Å; that was not observed although a small concentration of  $\text{Zn}_{\text{Nb}}$  could not be excluded. The environment about the Nb site (Nb EXAFS) was very consistent with diffraction experiments.

Here we report the EXAFS results at the Zn K edge for Zn doped stoichiometric material and show that the environment about Zn is essentially the same as that observed previously for congruent material, with slightly less local disorder.



### 5.1.1 Local environment about the Li and Nb sites

The local environments about the Li and Nb sites are shown in Fig. 5.1, based on the known crystal structure for  $\text{LiNbO}_3$  (space group  $R3c$ ). For the Li site in the undistorted crystal there are four Nb neighbors at  $\sim 3.06$  Å, and additional Nb neighbors at 3.36 and 3.88 Å. Around the Nb site, there are Li neighbors at  $\sim 3.06$ , 3.36 and 3.88 Å, with the first Nb neighbor at 3.77 Å; because Li is such a low Z element the M-Li contributions are tiny compared to M-Nb peaks. As a result there is a very large M-Nb peak in the EXAFS  $r$ -space data near 2.9 Å for substitution on the Li site but a much lower amplitude over the 2-3 Å range for defects on an Nb site; the largest peak for the Nb substitution site occurs near 3.6 Å. This provides a guide for setting up fits of the data. (See for example, Figs. 4 and 5 in Ref. [128]).

### 5.1.2 EXAFS data and analysis

The fluorescence  $k$ -space data at 10K for the Zn K edge are plotted in Fig. 5.2:top for the stoichiometric sample (0.7 mol% Zn; black solid line) and for the congruent sample (4.4 mol% Zn, (nominal 5 mol%); red dotted line) from our earlier study[128]. Because of the poorer signal-to-noise at high  $k$  for the low concentration sLNO sample, the useful  $k$ -range only extends up to  $\sim 13.2$  Å<sup>-1</sup>. We therefore fit the background above the edge over a shorter range and for comparison purposes, used the same parameters to re-fit the background for the old data for cLNO. The  $k$ -space plots in Fig. 5.2:top for the two crystalline forms (stoichiometric and congruent) are nearly identical. More details can be found in Sec. 5.2.4.

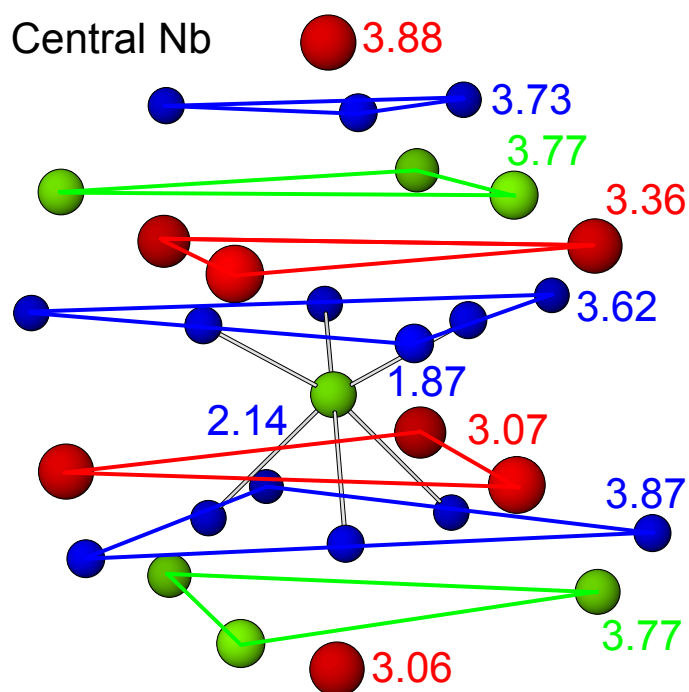
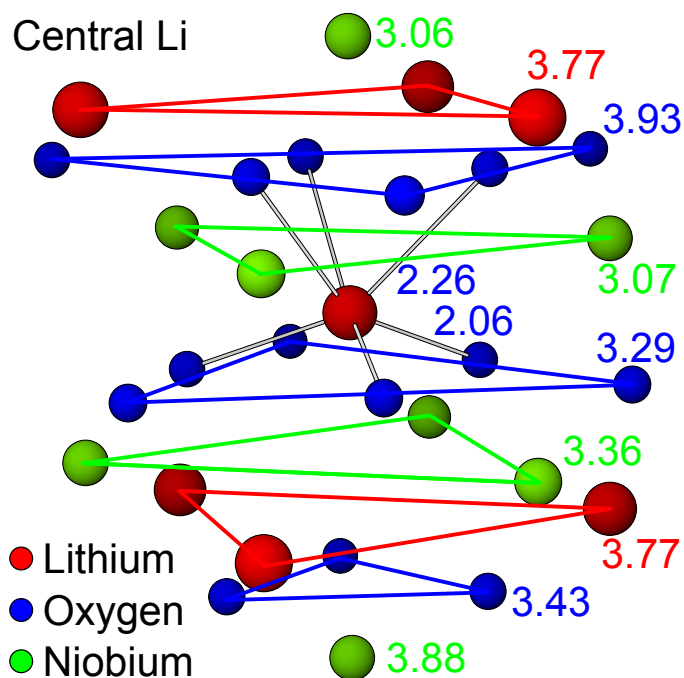


Figure 5.1: The environment about the Li (top) and Nb (bottom) sites in  $\text{LiNbO}_3$ . Bonds are shown for the nearest O atoms and the pair distances for the first few shells are indicated for each site.

The corresponding  $r$ -space data are shown in Fig. 5.2:bottom, using the Fourier transform (FT) range 3.8-13.2 Å<sup>-1</sup>. Because the  $k$ -space data in the top panel show a large oscillation from about 1-3.5 Å<sup>-1</sup>, much of which is in the XANES regime, the lower end of the FT window is therefore set at 3.8 Å<sup>-1</sup>. Note again that this is a slightly shorter FT range than in the earlier study. In the  $r$ -space data the amplitude of the Zn-O peaks (1.5-2 Å) are nearly unchanged for the two samples, while the amplitudes of the three Zn-Nb peaks for sLNO (near 2.75, 3.25, and 3.65 Å) are slightly ( $\sim 1\%$ ) larger. Other wise the position and shapes are nearly the same indicating essentially the same local environment.

The slight increase in amplitude for sLNO is to be expected since the Zn concentration is much lower and the average distortion in the lattice should be reduced. In particular, the Zn-Nb peak near 2.8 Å on the EXAFS plot, from four neighbors at  $\sim 3.05$  Å for a Li site occupation (Zn<sub>Li</sub>), remains large for the sLNO sample; it is too large for 25% of the total Zn to be on the Nb site, as Zn<sub>Nb</sub> has no Zn-Nb peak near this distance.

Because the two  $r$ -space traces in Fig. 5.2:bottom are nearly identical in shape, the sLNO data were fit in the same way as the cLNO data[128], assuming Zn is primarily on a Li site. In this fit the number of neighbors were fixed to the coordination numbers about the Li site as determined from diffraction[156; 157; 158]; the initial environment and pair-distances (from diffraction) are shown in Fig. 5.1. In the fits we varied the pair distances and the width,  $\sigma$ , of the (Gaussian) pair distribution function for each peak. Initially we used the following peaks (with actual distances): two Zn-O peaks near 2.06

and 2.26 Å; three Zn-Nb peaks near 3.06, 3.36 and 3.87 Å, and a longer Zn-O peak near 3.29 Å. From our earlier study the Zn-O peaks at 3.28 and 3.43 Å could not be resolved (and appeared to move together). Several weaker peaks are also included - a long Zn-O peak ( $r \sim 3.93$  Å), a weak Zn-Li peak ( $r \sim 3.76$  Å), and two weak multi-scattering (MS) peaks (Zn-O-Nb and Zn-O-O).

The  $r$ -space fit range for both samples was 1.3 - 4.3 Å and an example of a fit is shown in Fig. 5.3 for the sLNO sample; the individual peaks are shown below the fit and the weak peaks are shown in an expanded window at the bottom of the figure. Note that the two MS peaks are nearly out of phase (real part of FT) for most of the peak, and don't contribute much to the overall amplitude. The pair distances and  $\sigma^2$  values from the fit for the sLNO sample are tabulated in Table 5.1 for the main peaks, along with corresponding results for the new fit of the 4.4 mol% Zn, cLNO sample. For the latter the distances for the main peaks, obtained over the slightly different  $k$ -range are nearly identical (within 0.01 Å) to the earlier work[128]; the only significant difference is for the weak Zn-O3 peak (an average of 2 peaks) that is slightly shorter by 0.05 Å in these fits. There are also small differences in the values of  $\sigma^2$  between the new fit and the earlier results, but again the largest effects are for the weak Zn-O3 peak. A comparison between the cLNO and SLNO results in Table 5.1 show that the parameters for the two samples are nearly identical - the distances for the strong peaks agree to 0.01 Å or less and the  $\sigma^2$  values agree within 5 %; for the more distant Zn-O3 and Zn-Nb2 the differences are slightly larger. As observed previously the O shells shift slightly towards the Zn while the Nb atoms move slightly away.

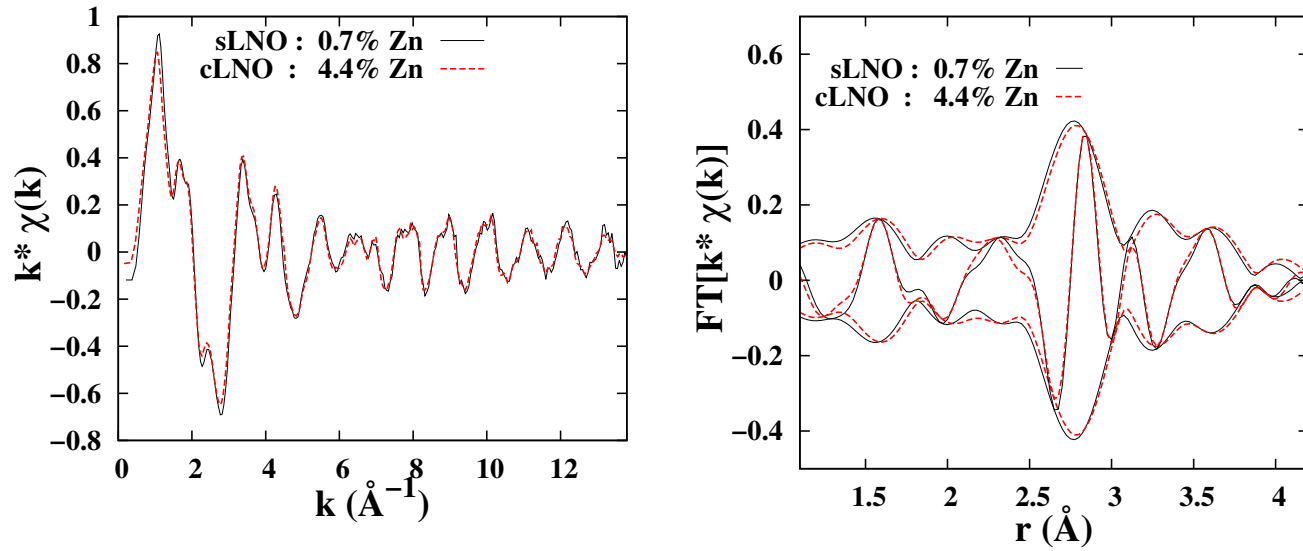


Figure 5.2: Left: the  $k$ -space data for sLNO (0.7 mol% Zn) and cLNO (4.4 mol% Zn) samples; sLNO black line, cLNO red dashed line, at 10K. The data for sLNO have more noise at high  $k$  because of the much lower Zn concentration, and this limits the Fourier transform (FT) range. Right: Plot of the corresponding fast FT (FFT) of the  $k$ -space data with an FT window 3.8-13.2  $\text{\AA}^{-1}$ ; the FT window is Gaussian rounded using a width, 0.2  $\text{\AA}^{-1}$ . There is a tiny difference between the data for sLNO and cLNO - the sLNO  $r$ -space plot has a slightly larger amplitude ( $\sim 1\%$ ) for all Zn-Nb peaks, consistent with a lower dopant concentration. For the  $r$ -space data (here and in later plots), the fast oscillating function is the real part,  $R$ , of the FFT while the amplitude is  $\pm\sqrt{R^2 + I^2}$  where  $I$  is the imaginary part of the FFT.

Table 5.1: Fit results for the Zn K edge data at 10K, for the sLNO (0.7 mol%) and cLNO (4.4 mol%; nominal 5 mol%) samples, plus distances from diffraction (Diff.). The Zn-O3 shell represents two longer Zn-O shells (three neighbors each at 3.28 and 3.43 Å; which collapse to a single peak with six O neighbors at an average distance near 3.25 Å. The second column gives corresponding pair distances about the Li site from diffraction for congruent LiNbO<sub>3</sub>. The errors for  $r$  are  $\pm 0.01$  Å for the major peaks and most relative errors for  $\sigma^2$  are  $\pm 0.0005$  Å<sup>2</sup>. However systematic errors in  $\sigma^2$  can be  $\sim 10$  %.

LiNbO <sub>3</sub>	Diff.	cLNO (4.4 mol%)		sLNO (0.7 mol%)	
Atom pair	$r$ (Å)	$r$ (Å)	$\sigma^2$ (Å <sup>2</sup> )	$r$ (Å)	$\sigma^2$ (Å <sup>2</sup> )
Zn-O1	2.06	2.01	0.0050	2.01	0.0049
Zn-O2	2.26	2.25	0.0083	2.24	0.0079
Zn-Nb1	3.06	3.13	0.0032	3.12	0.0028
Zn-O3	—	3.24	0.0037	3.24	0.0052
Zn-Nb2	3.36	3.38	0.0033	3.38	0.0033

The above fit, assuming only a Li substitution site, fits the data very well. To explore how much Zn might be on the Nb site, we allowed a small occupation on this site; Zn<sub>Nb</sub> would add a relatively large Zn-Nb peak near 3.4-3.5 Å in the EXAFS plot (actual distance  $\sim 3.76$  Å) because there are 6 Nb neighbors at this distance about the Nb site. Also, the Zn-Li peaks for this site are small and can be neglected compared to the Zn-Nb peak. In addition the amplitude (i.e. number of neighbors) of the large peaks near 2.8 and 3.3 Å on Fig. 5.3 for Zn<sub>Li</sub> must decrease by the fraction on the Nb site. The fit does not want a peak at the expected position for Zn<sub>Nb</sub> and rapidly becomes poor if a significant fraction of the Zn is on the Nb site; fits can be achieved with up to 6-7 % of the Zn on Nb, by varying  $\sigma$  and allowing a rather large increase in  $r$ . However the goodness-of-fit parameter only increases slightly; although there are more parameters, by using the Hamilton F-test,[?] this peak is not significant. Thus 6-7 % of the Zn is much too large an estimate for a Nb site occupation.

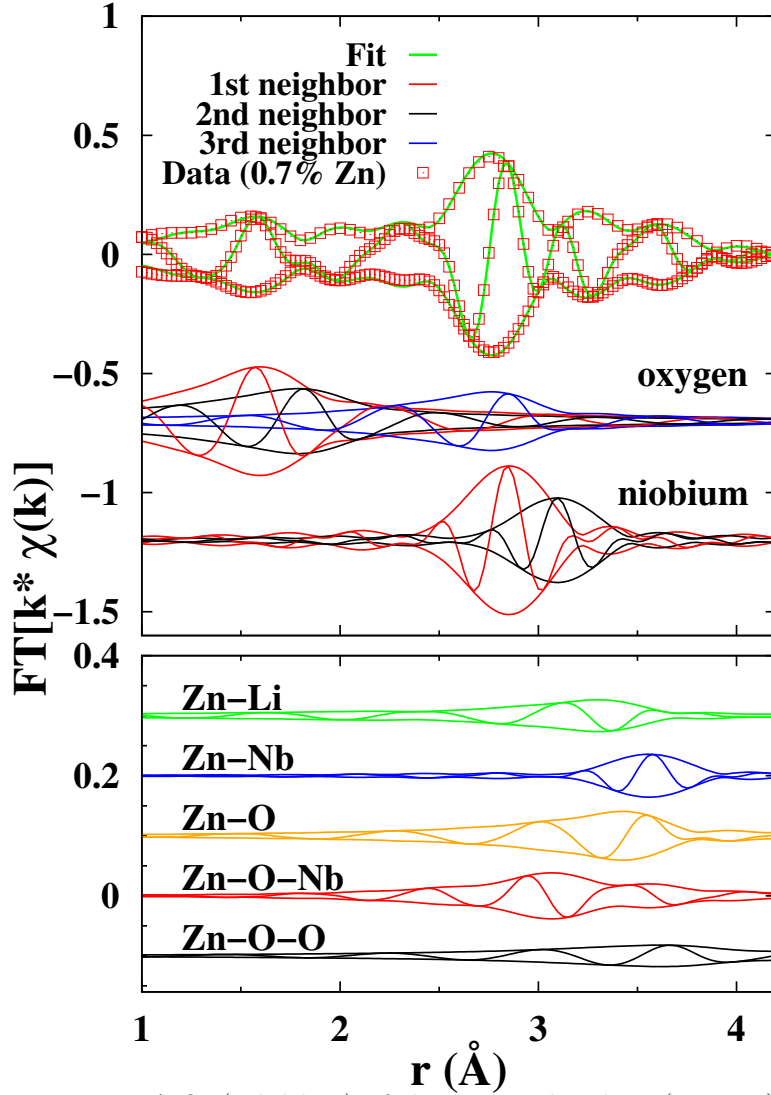


Figure 5.3: A fit (solid line) of the Zn K edge data (squares) for sLNO with 0.7 mol% Zn, to a sum of functions calculated using FEFF[4]; the  $r$ -space fit range was 1.3-4.3  $\text{\AA}$ , and the FT range was 3.8-13.2  $\text{\AA}^{-1}$ ; remaining degrees of freedom, 4. The fit is excellent over the entire fit range, particularly near 3.5  $\text{\AA}$  where a large Zn-Nb peak would exist if significant Zn were on the Nb site. The main individual peaks are plotted beneath the fit; the weak peaks for more distant neighbors – and also two MS peaks – are shown in an expanded view (zoomed by 2.5) in bottom panel.

An additional problem with this fit is that it requires a large increase in the Zn-Nb distance for this extra peak, by nearly 0.1 Å; then it overlaps another Zn-Nb peak ( $Zn_{Li}$ ) near  $\sim 3.87$  Å. Two unresolved peaks at nearly the same distance is not a reasonable model. From the fits to the  $Zn_{Li}$  site there is relatively little distortion about the defect for the distant neighbors beyond  $\sim 3.8$  Å – observed shifts in  $r$  are  $\leq 0.02$  Å for these long pair-distances. Also note that when divalent Zn replaces Li, the closest O atoms are pulled in slightly while the nearer metal atoms are pushed away. On the other hand, for divalent Zn on the Nb(+5) site the reverse might be expected – O atoms relax slightly away from Zn while metal atoms move slightly inward. In any case one would not expect a large increase in a metal-pair distance this far from the Zn atom on a Nb site. We therefore carried out a fit starting with the best fit parameters for the  $Zn_{Li}$  site fit, plus a small Zn-Nb peak for some Zn on Nb ( $r \sim 3.76$  Å), but constrained any shift in  $r$  to be  $\leq 0.02$  Å. This fit suppresses the amplitude of the Zn-Nb peak for the Nb site - the amplitude decreases and the width increases such that on the scale of Fig. 5.3 this peak has little amplitude. This fit sets an upper limit of 2 % of the total Zn on the Nb site.

We also re-analyzed the data for the congruent samples (4.4 and 6.0 mol% Zn) using the above model and obtained the same result - if shifts in  $r$  are constrained to be  $\leq 0.02$  Å, the fraction of Zn on a Nb site is less than 2 %.

The difficulty in adding a Zn-Nb peak for the  $Zn_{Nb}$  site, close to the expected position (3.76 Å) can be observed visually assuming a somewhat higher concentration on the Nb site – e.g. assume a 10 % occupancy. The Zn-Li peaks are all small and the



$r$ -space plot is dominated by the long Zn-Nb peak for this site. In Fig. 5.4 we focus on the region from 3-4 Å, and compare the full fit of the data in Fig. 5.3 (well modeled by a Li site occupation) to a sum of the small Zn-Nb peak corresponding to 10 %  $Zn_{Nb}$  plus 90 % of the fit to the  $Zn_{Li}$  site; this sum is shown as a red line. The main issue is the change in shape of the real part  $R$  of the transform near 3.4-3.5 Å on the EXAFS plot. The fit for a Li site (and the data) have a clear kink in  $R$  near 3.4 Å; but with 10 % occupation on the Nb site the kink completely disappears, the shape of  $R$  becomes more symmetric, and the overall peak in  $R$ , shifts down to about 3.5 Å.

Optical damage resistance is increased in LNO crystals when the concentration of a suitable dopant (e.g. Zn, Mg, In, etc.) exceeds the so called threshold value, which depends on the valence state of the dopant, the stoichiometry of the crystal, and likely the substitution site. The higher the Li/Nb ratio the lower the threshold concentration[146]. For stoichiometric samples the threshold is close to 0 mol% while for congruent materials it is  $\sim 5$  mol% for divalent defects. While it is generally accepted that most of the dopants occupy Li sites in LNO crystals, the incorporation mechanism of the dopant may change above the threshold concentration[153] and some of the dopant might also occupy Nb sites[29; 153; 30].

Both cLNO and sLNO crystals containing optical damage resistant ions above the threshold, reveal an IR absorption band due to the stretching vibration of hydroxyl ions which form complexes with a dopant (e.g Zn) occupying the Nb site[159]. However, integrated absorption values per hydroxyl ions determined for LNO crystals[160] show that only very small amounts of the dopants are involved in such complexes and most of

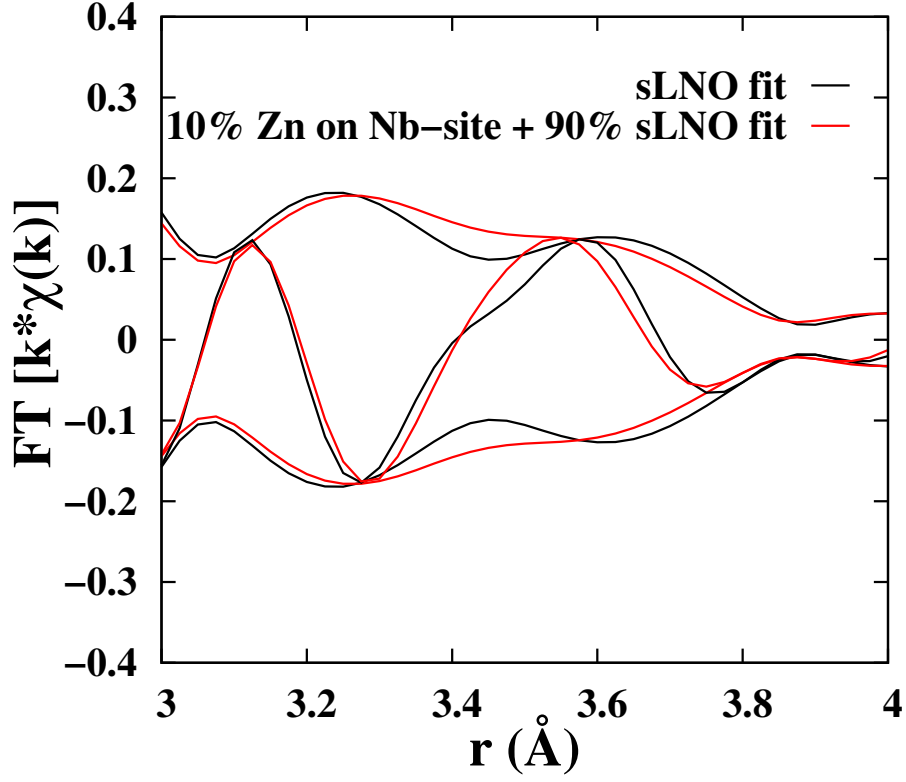


Figure 5.4: The effect on the EXAFS plot if a small Zn-Nb peak with an actual distance of 3.76  $\text{\AA}$ , corresponding to 10 % Zn on the Nb site, is added to 90 % of the fit to the Li site. This adds a peak near 3.4-3.5  $\text{\AA}$  on the EXAFS plot, and even for this small amount of Zn on Nb, the shape of the real part of the transform,  $R$ , is changed significantly.

the dopant may still occupy Li sites in agreement with the present EXAFS results. As noted earlier, Xu *et al.*[30] argue that as the chemical potential moves towards that for the stoichiometric composition, the formation energy for 2+ defects becomes positive and further increases in dopant concentrations will be small. Thus although there may be a change in the doping mechanism (from  $\text{Zn}_{\text{Li}} + 3 \text{V}_{\text{Li}}$  to  $\text{Zn}_{\text{Nb}} + 3 \text{Zn}_{\text{Li}}$ ) as the Zn concentration exceeds the threshold composition, the net fraction of  $\text{Zn}_{\text{Nb}}$  may remain small. The strongest constraint should come from the sLNO sample but one cannot easily estimate the effective threshold concentration for a given crystal. The lack of a significant fraction of  $\text{Zn}_{\text{Nb}}$  for sLNO may suggest that the self compensating doping model ( $\text{Zn}_{\text{Nb}} + 3 \text{Zn}_{\text{Li}}$ ) may be suppressed. For congruent material, to have  $\sim 10\%$  of the Zn as  $\text{Zn}_{\text{Nb}}$  (which would be easily observable in EXAFS) as a result of a transition to the self compensating doping model above threshold, the concentration in the crystal would need to be about 9 mol% (4 mol% above the threshold concentration for divalent defects); then  $\sim 1\%$  would be  $\text{Zn}_{\text{Nb}}$ .

To summarize we have determined the local environment about Zn in stoichiometric LNO, using a low Zn concentration, 0.7 mol%. The environment is nearly identical to that for congruent LNO, but with slightly less local disorder - which is expected for a dilute impurity. The types of neighbors about Zn and distances to them indicate a primary  $\text{Zn}_{\text{Li}}$  site as found in the earlier study of Zn-doped congruent LNO. Thus the dominant substitution mechanism is  $\text{Zn}_{\text{Li}} + 3 \text{V}_{\text{Li}}$ . However one must also include significant local distortions for the first few shells; on average, the O shells move towards Zn while the Nb shells move away. Such distortions will likely modify the en-

ergy calculations and there is likely a distribution of slightly different clusters about each Zn atom. Because of the positive defect formation energy for samples close to the stoichiometric composition[30] it is not clear that the Zn concentrations in sLNO can be increased sufficiently that a significant fraction of  $\text{Zn}_{\text{Nb}}$  ( $> 5\%$  of total Zn) are present.

## 5.2 $\text{Er}^{3+}$ , $\text{In}^{3+}$ , and $\text{Hf}^{4+}$ Dopants

In Sec. 5.1 we have shown that for Zn dopants, the primary substitution site is on Li – i.e.  $\text{Zn}_{\text{Li}}$ , for both cLNO and sLNO; at most a few percent of Zn is on an Nb site.[128; 161] Since Zn has a 2+ valence this requires Li vacancies for charge compensation. There are a few theoretical calculations for the solution energies of dopants on various sites, with various charge compensation models.[29; 5; 30; 153] For Zn, Araujo *et al.*[29] found that the self-compensating model with 75 % of Zn on a Li site and 25 % of Zn on a Nb site has the lowest solution energy for bound defects, which is inconsistent with the EXAFS analyzes. However these calculations were carried out for  $T = 0$  and 293 K, and assumed the dopant and associated charge compensator ions were in thermal equilibrium in stoichiometric material. Xu *et al.*[30] using DFT calculations note that the site occupation will depend on the chemical potential, and when it is close to that for congruent material, both 2+ and 3+ defects are on the Li site, with Li vacancies ( $V_{\text{Li}}$ ) for charge compensation – but they only considered a few dopants and did not consider Zn. In addition, if the chemical potential is close to that for stoichiometric material it's more complex - for  $\text{Fe}^{2+}$ , Fe substitutes on Li (slightly

lower energy) while  $\text{Mg}^{2+}$  has a lower energy for self compensation with Mg on both Li and Nb sites (75 % and 25 % respectively) as found by Araujo *et al.*.

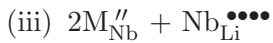
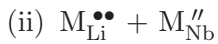
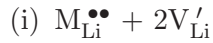
For 3+ defects such as  $\text{In}^{3+}$  or  $\text{Er}^{3+}$ , and 4+ defects such as  $\text{Hf}^{4+}$ , solution energies have also been calculated for bound defects. Xu *et al.*[30] considered three defect clusters (schemes (i), (ii), and (iii) in next section) and found that for 3+ defects ( $\text{Fe}^{3+}$   $\text{Nd}^{3+}$  and  $\text{Er}^{3+}$ ) in stoichiometric material, the self compensation configuration with 50% on each site has the lowest energy; while for congruent material, substitution is on the Li site. Araujo *et al.*[29; 5; 6] have also considered a number of substitution schemes for such defects which are summarized below.

The EXAFS experiments reported here investigate the substitution sites for univalent 3+ and 4+ dopants in both cLNO and sLNO. Co-doped samples and samples with multi-valent dopants are excluded at this point because the local structure could be more complex. In and Hf ions are both considered to be optical damage resistant (ODR) ions. Rare earth ions such as Er are incorporated into LNO to serve as laser activators[162] and for optical hole burning applications[163]. EPR experiments indicate that in co-doped samples (Er plus a threshold concentration of Mg or Zn), a broad, strong new resonance is observed that is attributed to Er on a Nb site.[164] This suggests that in stoichiometric samples Er dopants may also have a significant fraction of  $\text{Er}_{\text{Nb}}$ ; recently a low concentration (few percent) of  $\text{Er}_{\text{Nb}}$  in sLNO has been observed using  $\text{OH}^-$  vibrational spectroscopy.[165] In general it is assumed that when the concentration of  $\text{Nb}_{\text{Li}}$  antisite defects is low, as is the case for stoichiometric crystals, it promotes the occupation of the Nb site, and we have included two stoichiometric samples to see if

significant occupation of the Nb site occurs.

### 5.2.1 Substitution models for In and Er

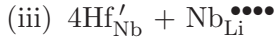
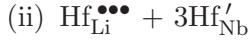
Araujo *et al.*[5; 29] considered four different schemes for  $\text{In}^{3+}$  and  $\text{Er}^{3+}$  substitution in sLNO; the three schemes with the lowest energies are listed below using KrögerVink notation;[166] here  $M = \text{In}$  or  $\text{Er}$ . The numbering of Araujo *et al.*[5; 29] and Xu *et al.*[30] are the same for schemes (i)-(iii). (Scheme (iv) has different compensating defects compared to (iii), but has a higher energy.) For calculations at 0 K, the solution energies for In are nearly identical for schemes (ii) and (iii) but scheme (ii) is lowest for calculations at 293 K. For In, scheme (i) has higher energies at 0 and 293 K, but has the largest decrease with increasing temperature. For Er, scheme (ii) has the lowest energy at 0 K, but scheme (iii) is lower at 293 K. All dopants are on the Li site for scheme (i) while 50% of dopants are on the Li site for scheme (ii); in scheme (iii) all the dopants are on the Nb site.



### 5.2.2 Substitution models for Hf

Recently Araujo *et al.*[6] have also calculated the solution energies for the  $\text{Hf}^{4+}$  defect in sLNO. Here they considered seven different schemes, but schemes (iii) to (vii)

have all Hf only on a Nb site, with different charge compensation defects. Scheme (i) which is the only defect model with all Hf on a Li site, has a very large defect solution energy; the schemes with the three lowest energies are tabulated below. At both 0 and 293 K, scheme (vi) has the lowest energies, while scheme (ii) is second lowest – however, the energies for these three models differ by less than a factor of 2. For the self-compensating scheme (ii), 25% of Hf are on the Li site; 75% on Nb site.



### 5.2.3 Ionic radii

An important aspect to consider in discussing the occupation sites for the dopants is the ionic radius of the dopant and how it compares to the host cations. We list a few relevant ionic radii in Table 5.2 for 6-fold coordinations. These radii together with that of  $\text{O}^{2-}$  can be used to estimate the average M-O distances for the first O-shell about the dopant. Note that the average Li-O and Nb-O distances in the first O-shell in the host material agree well with this empirical approach (e.g. bond lengths for Li-O are 2.06 and 2.26 Å; average = 2.16 Å. Sum of ionic radii for  $\text{Li}^+$  and  $\text{O}^{2-}$  is 2.14 Å.) Using the ionic radii and ignoring corrections for octahedral distortions[7], we can roughly predict the expected M-O distances for the first shell about the dopant: In – 2.18 Å; Er – 2.27 Å; Hf – 2.09 Å. All dopants have larger ionic radii than Nb, with

Atom	Valence	Radius (Å)
Li	1+	0.76
Nb	5+	0.64
Zn	2+	0.74
In	3+	0.80
Er	3+	0.89
Hf	4+	0.71
O	2-	1.38

Table 5.2: Ionic radii tabulated by Shannon[7] for different dopants and host cations with 6-fold coordination. The  $O^{2-}$  ionic radius corresponds to an oxygen in 4-fold coordination with it's neighbors. The much larger radius of  $Er^{3+}$  compared to other ions results in the larger positive shifts in bond length for Er-O bonds.

	cLNO	sLNO
In	0.7	
In	2.8	
Er	2.3	
Er		0.55
Hf		0.57

Table 5.3: Summary of dopants studied and type of host crystal (sLNO or cLNO) with measured concentrations given in mol %.

Hf the closest in size (only 0.07 Å larger). Thus from ionic radii considerations alone, occupation of the Nb site appears less likely for In and Er. Substituting a larger ion for a smaller one will introduce significant distortions.

#### 5.2.4 EXAFS data and analysis

The  $k^2\chi(k)$  data were fast Fourier Transformed (FT) into  $r$ -space and are plotted in Figs. 5.6 - 5.7. The 0.7 and 2.8 mol% In  $r$ -space data (In K edge) are compared at 10 K in Fig. 5.6 using an FT range of 4.1 - 14.7 Å<sup>-1</sup>; the two traces are nearly identical indicating no significant change between these concentrations. Similar



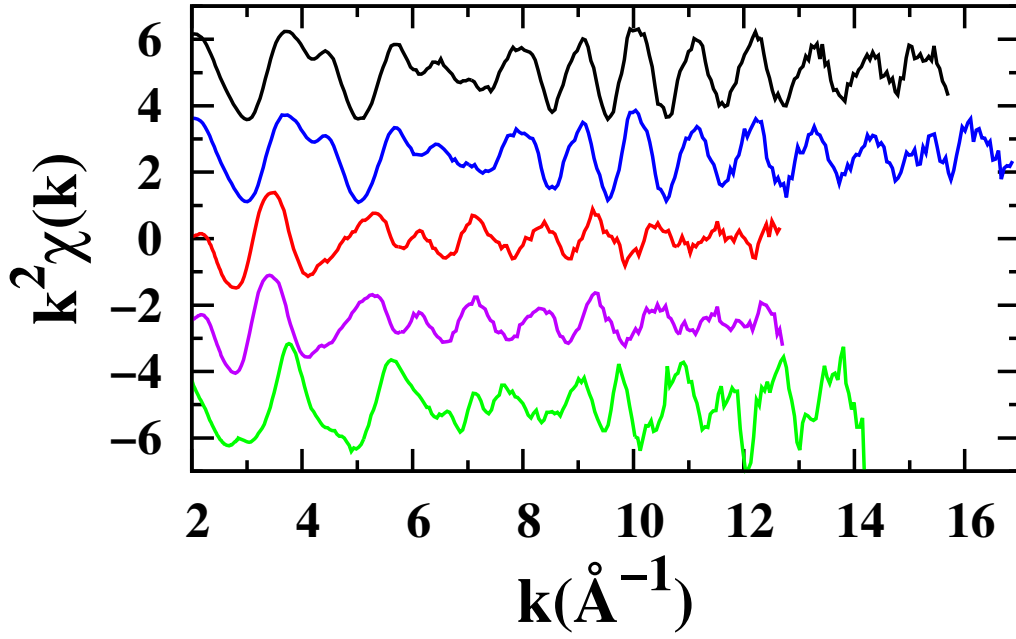


Figure 5.5:  $k^2\chi(k)$  vs  $k$  from top to bottom: at the In K edge, black - cLNO, 0.7 mol% In, blue - 2.8 mol% In; at the Er  $L_{\text{III}}$  edge, red - sLNO, 0.55 mol% Er, purple - cLNO, 2.3 mol% Er; and at the Hf  $L_{\text{III}}$  edge, green - sLNO, 0.57 mol% Hf. The plots are displaced vertically for clarity.

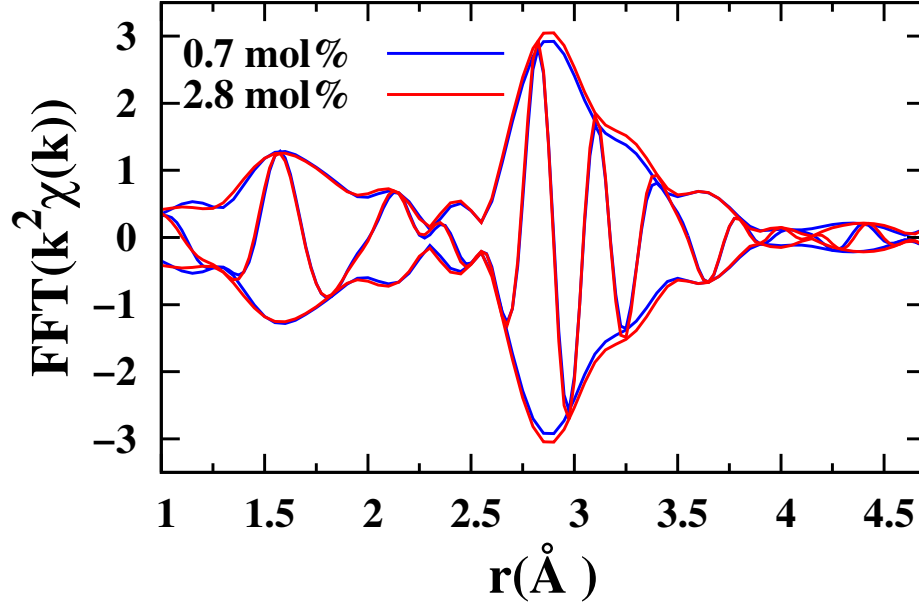


Figure 5.6: Comparison of the  $r$ -space data [FT  $k^2\chi$ ] for 0.7 mol% and 2.8 mol% In doped cLNO at 10 K. The FT range is 4.1 - 14.7  $\text{\AA}^{-1}$ . The differences between the two traces are very small, with the largest deviations in the 2.75-3.25  $\text{\AA}$  range. In this and subsequent  $r$ -space plots the fast oscillation is the real part  $R$  of the FT while the envelop function is  $\pm\sqrt{R^2 + I^2}$  where  $I$  is the imaginary part of the FT.

data at 300 K (not plotted) show similar functions, but with a decreased amplitude from thermal broadening. The very large amplitude peak near 2.9  $\text{\AA}$  in the EXAFS plot, is a signature of substitution on a Li site, but the peak position on the EXAFS plot is shifted to lower  $r$  by a well known phase shift; this is typically 0.2  $\text{\AA}$  for heavy backscattering atoms but larger for O atoms  $\sim 0.4 \text{\AA}$ .

Similar  $r$ -space data for the Er substituted sample (Er L<sub>III</sub>) are shown in the top panel of Fig. 5.7 for a shorter FT range 4.1-11.5  $\text{\AA}^{-1}$ . The traces for the stoichiometric material (0.55 mol% Er) and congruent material (2.3 mol% Er) are quite similar and overlap well for the short Er-O peaks (near 1.7  $\text{\AA}$  on plot) and also near 4  $\text{\AA}$ .

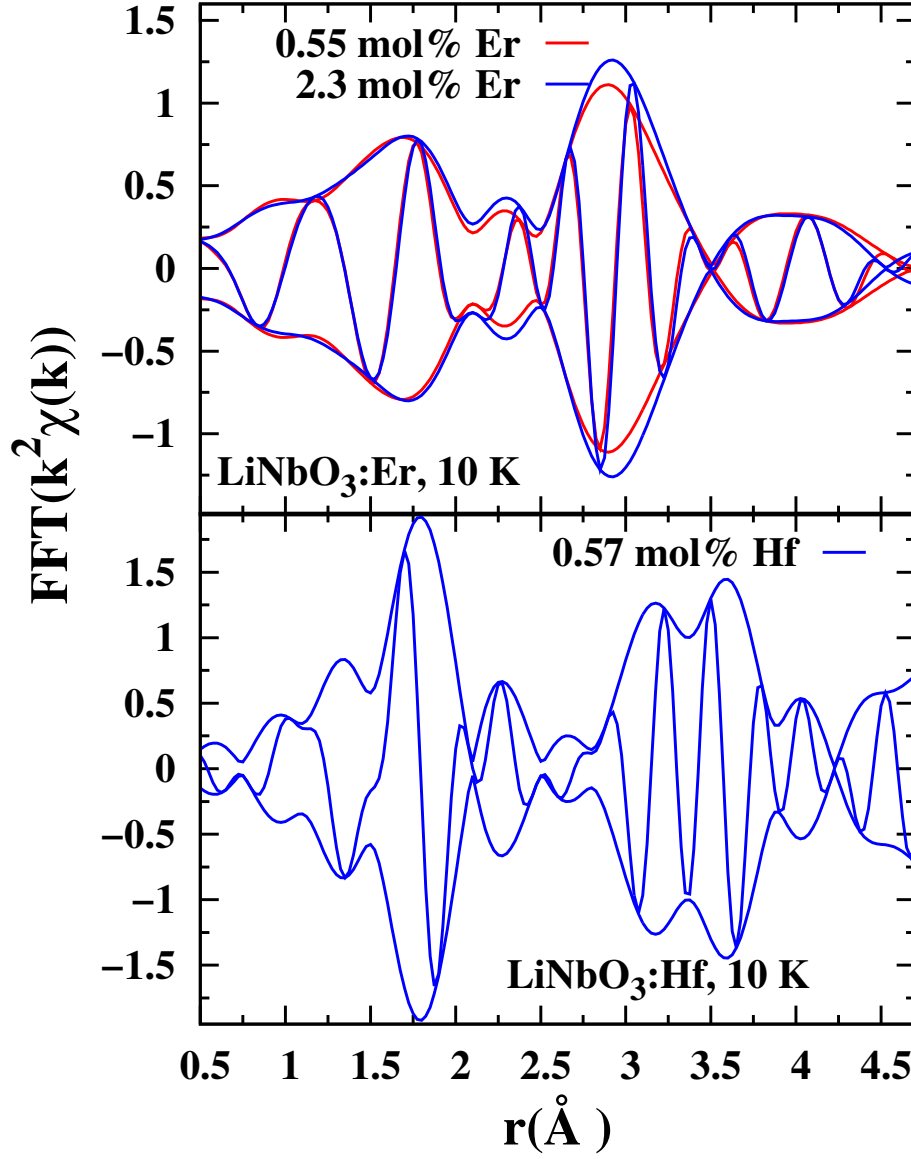


Figure 5.7: Top: Comparison of  $r$ -space data at 10 K for 0.55 mol% Er in sLNO (red) and 2.3 mol% Er in cLNO (blue). The largest change is at the Er-Nb peak near 2.9 Å which is smaller in the sLNO sample, suggesting possibly less Er on the Li site for sLNO. The FT range is 4.1 - 11.5 Å<sup>-1</sup>. Bottom:  $r$ -space data at 10 K for 0.57 mol% Hf in sLNO (blue). Note the smaller amplitude near 2.9 Å, and the larger peak near 3.6 Å compared to the Er (or In) data, indicating some Hf is on an Nb site. FT range is 3.8-12.7 Å<sup>-1</sup>.

However, there is a noticeable difference near 2.9 Å, where the largest peak is observed; it is attributed to an Er-Nb peak with Er on a Li site. Whether the number of Er-Nb bonds changes between samples (from a small change in defect site occupations) or the peak is broadened from disorder, requires detailed fits.

The  $r$ -space plot for Hf substituted sLNO is shown in the lower panel of Fig. 5.7 and is quite different from either the Zn, In, or Er  $L_{III}$  edge EXAFS data; FT range 3.8-12.7 Å<sup>-1</sup>. The most striking differences are the larger amplitude near 3.6 Å (actual distance  $\sim$  3.8 Å), where an Hf-Nb peak should occur for substitution on a Nb site, and the low amplitude near 2.9 Å, where the Hf-Nb peak would occur for substitution on an undistorted Li site. Surprisingly the Hf-O peak near 1.75 Å, is also larger for the Hf data. The significant difference in amplitude over the 3 to 4 Å range suggests that a significant fraction of the Hf occupies an Nb site.

### 5.2.5 Fits of data

The data are fit in  $r$ -space to a sum of peaks corresponding to different shells of neighbors about the dopant. Theoretical EXAFS functions for each peak were calculated using FEFF7[127]. For the In and Er dopants, the large peak near 2.9 Å corresponds to a M-Nb peak, when a large fraction of metal (M) dopants is on the Li site; for Hf the lack of a strong peak near 2.9 Å and the large peak near 3.6 Å indicates some substitution occurs on the Nb site. For each type of site there are also some weak M-Li pairs, and at longer distances some weak multi-scattering peaks, but most of these are negligible. The fits at each edge and the significant results are discussed below.

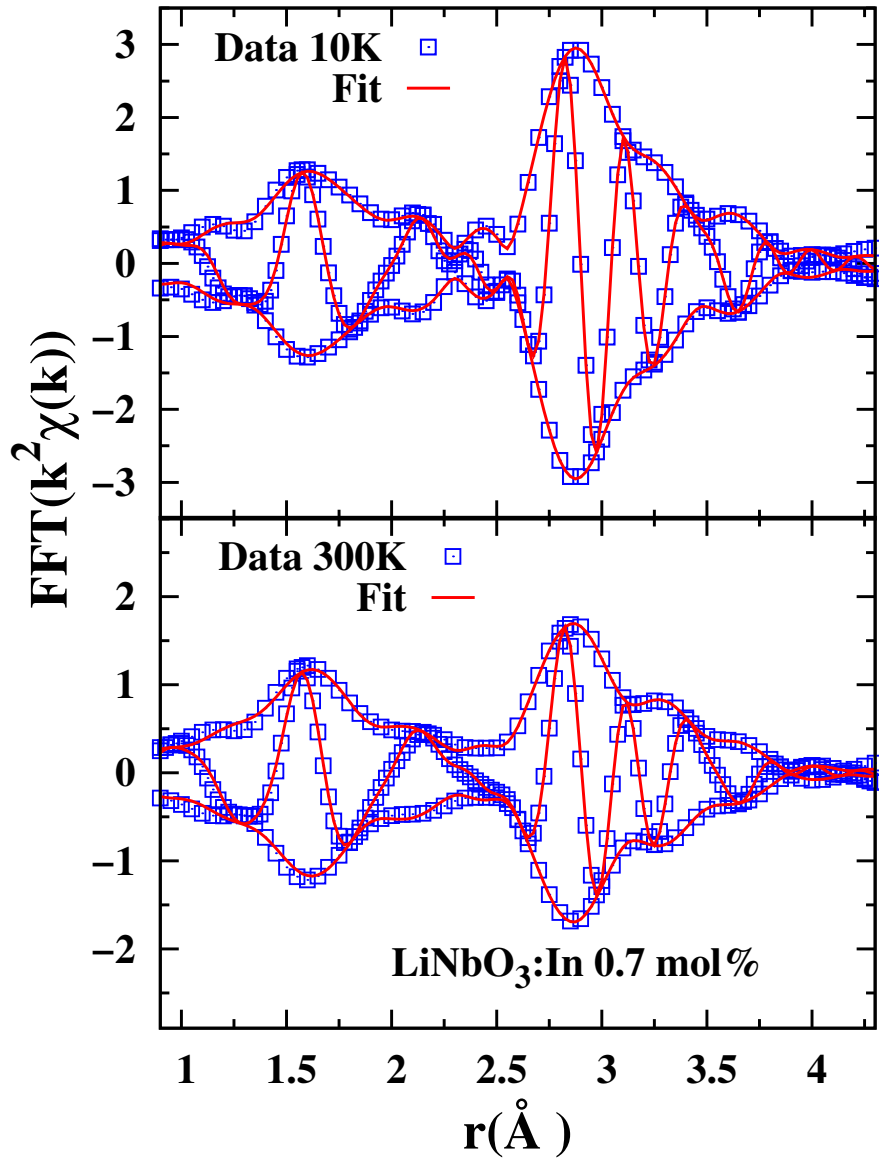


Figure 5.8: Fits of the  $r$ -space data  $[\text{FT } k^2\chi]$  for 0.7 mol% In doped  $\text{LiNbO}_3$  at 10 and 300K (data - blue squares; fit - red lines); see text for model. The amplitude at 300K is significantly reduced from thermal vibrations for the In-Nb peaks above 2.5 Å. The FT range is 4.1-14.7 Å<sup>-1</sup>, while the fit range is 1.2-3.9 Å;  $S_0^2 = 1.0$ .

For the In doped samples the same model fits the data sets for both 0.7 mol% and 2.8 mol% In samples. There are two short In-O bonds, with longer In-O peaks near 3.3 and 3.9 Å. Note that for an undistorted Li site there are two intermediate Li-O distances at 3.29 and 3.43 Å, but these could not be resolved in the Zn data (two peaks moved together) and were fit with an average peak near 3.29 Å[161]; a similar result is found here. The expected In-Nb pair distances are near 3.06, 3.36 and 3.87 Å. Overall, the In-O pairs have slightly shorter distances on average while the In-Nb pair distances are slightly increased (see Table 5.4), as found earlier for the Zn substituted samples in Sec. 5.1. This model fits very well up to 3.5 Å, but above 3.5 Å, the fit amplitude is too low. Various models were tested, including increasing the Nb-site occupation of the In dopant. This approach did not work well.

The In-Nb shells for an undistorted lattice would be near 3.06, 3.36 and 3.87 Å. To improve the fitting for  $r > 3.5$  Å where the fit amplitude was too low, several approaches were tried. First, using multi-scattering peaks or the weak In-Li peak does not significantly improve the fit because the amplitudes of these peaks is low –these small peaks were not included in the final fits. To increase the amplitude significantly for this  $r$ -range, requires a heavy backscattering atom at a distance close to 3.8-3.9 Å, either In or Nb. Increasing for example, the number of neighbors for the In-Nb peak ( $r \sim 3.9$  Å) from 1 to 2, does improve the fit but is inconsistent with the LNO structure. One possibility for a peak near this distance is to consider a significant fraction of In on an Nb site (as proposed in self compensating models) for which there would be an In-Nb peak, expected near 3.6 Å in the EXAFS plot. However the amplitude of this

Table 5.4: Fit parameters for fits of the In data. The In-O3 peak near 3.3 Å is a sum of two peaks at nominally 3.29 and 3.43 Å in pure LiNbO<sub>3</sub> (only the average - 3.36 Å is listed below, under diffraction. The In-In peak assumes that In-In pairs form in Li sites 3.77 Å apart.)

	Diff.	In 0.7 mol%, cLNO		In 2.8 mol%, cLNO	
Atom pair	$r$ (Å)	$r$ (Å)	$\sigma^2$ (Å <sup>2</sup> )	$r$ (Å)	$\sigma^2$ (Å <sup>2</sup> )
In-O1	2.06	2.08	0.0020	2.07	0.0019
In-O2	2.26	2.22	0.0043	2.22	0.0039
In-Nb1	3.06	3.21	0.0025	3.21	0.0024
In-O3	3.36	3.31	0.0056	3.30	0.0046
In-Nb2	3.36	3.47	0.0032	3.47	0.0032
In-In	3.77	3.85	0.0020	3.86	0.0020

peak is coupled to that of the largest peak (In-Nb) near 2.9 Å. If a fraction  $f$  of the In were on the Nb site, then the fraction on the Li site would decrease to  $1-f$ , and that would decrease the number of neighbors for the peak at 2.9 Å. Including this constraint on the amplitudes leads to a small fraction on Nb  $< 5$  %.

There is another way, however, to get more amplitude above 3.5 Å. Since In substitutes mainly on a Li site we also considered the possibility of pairs of In atoms on closest Li sites,  $\sim 3.8$  Å apart. This would add an In-In peak with one neighbor at a distance near 3.8 Å, and did improve the fit. This would add an In-In peak with one neighbor at a distance near 3.8 Å. Surprisingly, this gave a better fit than adding an extra (one neighbor) In-Nb peak at roughly the same distance. Although strongly suggestive that In-In pairs do form it is not conclusive as the amplitude near 3.6 Å is small. In the final fits 16 parameters were varied with 5 degrees of freedom remaining.[34] Plots of the fits for 0.7 mol% In at both 10 and 300K are shown in Fig. 5.8 and the results at 10 K are summarized in Table 5.4; the fraction of In on an Nb site is  $< 5$  %.

For the Er substituted samples, the peak near 2.9 Å is smaller compared to the In data, suggesting that some of the Er might be on an Nb site. This complicates the analysis because then there are distinct peaks for each site, and the FT range is limited compared to In – see Fig. 5.5. Again we use two peaks for the first O shell and used the same model for Er on a Li site as used for In. The region from 3.8-4.5 Å has a sum of many Er-O peaks and is roughly modeled by a large amplitude Er-O peak; this served well and did not introduce an excess of parameters. Initially we found that a fit including only Li site occupation results in a reasonable fit, but wanted to investigate if the fit would improve if some of the Er were on a Nb site. For this, we employed a parameter  $f_1$  as the fraction on a Li site, with  $(1-f_1)$  on the Nb site. An Er-Nb peak was added at 3.77 Å, plus a Nb site Er-O peak at 3.62 Å.

Initially we considered shifting the beginning of the FT range to lower  $k$  –  $k_{\min} \sim 3.5 \text{ Å}^{-1}$ ; however, when using a lower bound for  $k_{\min}$ , it is possible to include a small contribution from the XANES. This was checked by fitting to  $k\chi(k)$ ,  $k^2\chi(k)$ , and  $k^3\chi(k)$ ; in such fits the parameters should not change significantly for different  $k$ -weightings. However, since  $k^2$  and  $k^3$  weighting suppress the low  $k$  data, if some XANES is included it will mainly affect the  $k\chi(k)$  data. Such tests showed that  $k_{\min} = 3.5 \text{ Å}^{-1}$  is too low and lead to a minimum value of  $k_{\min} = 4.1 \text{ Å}^{-1}$ .

The fits used the same Li-site model as used for In above. To test for Er on an Nb site, an Er-Nb peak (near 3.77 Å) and an Er-O (near 3.62 Å) were added. In addition because of the large amplitude in the EXAFS data from 3.8-4.5 Å, a large Er-O peak was added. From 4.26-4.62 Å (actual distances) there are 12 different O neighbors



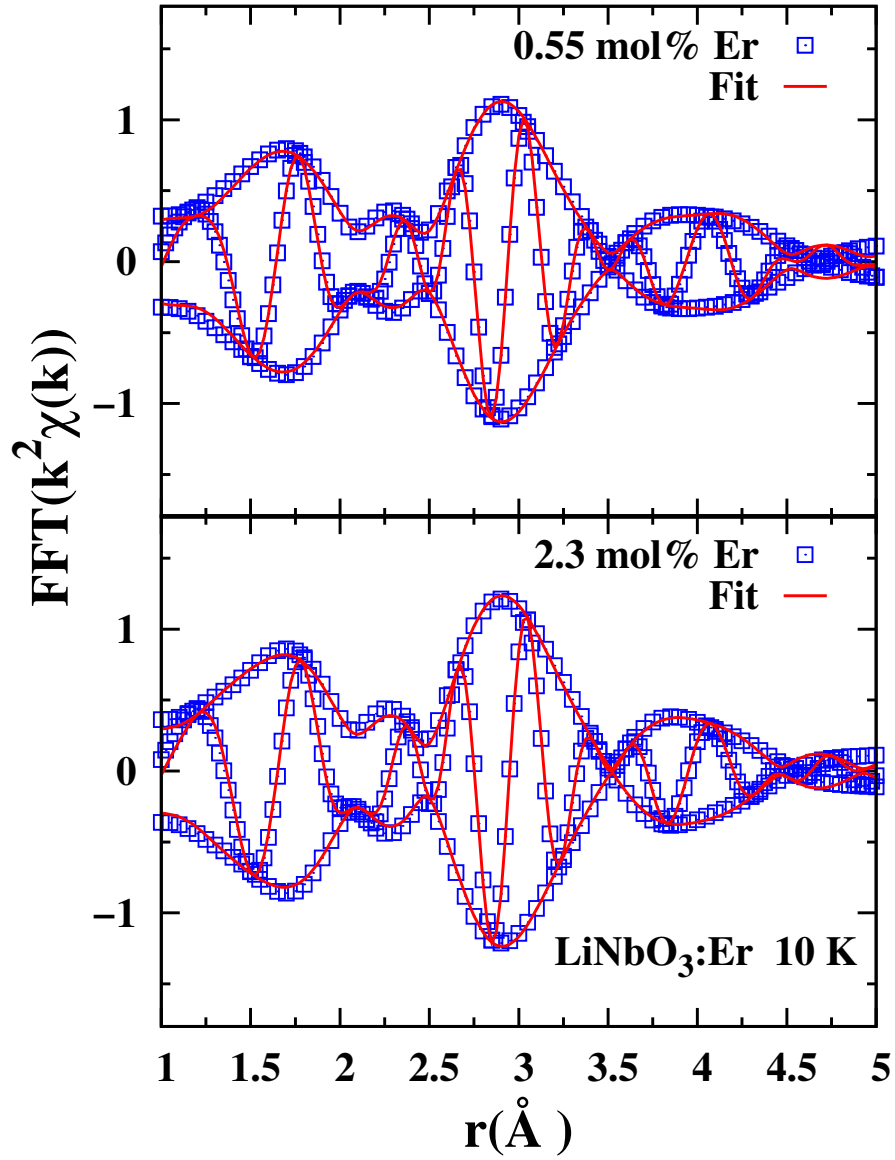


Figure 5.9: Fits of the 0.55 mol% Er (sLNO) and 2.3 mol% Er (cLNO) at 10 K (data - blue squares; fit - red line). A good fit is achieved up to  $\sim 4.5$  Å; see text for model and Table 5.5 for main parameters. The FT range is  $4.1\text{-}11.5$  Å<sup>-1</sup> and fit range is  $1.1\text{-}4.6$  Å.

for the LNO structure; depending on how these peaks shift they can add constructively or destructively. The shape of the peak in  $r$ -space near 3.9 Å is that of an Er-O peak; to model this aggregate contribution we added a large Er-O peak, at a distance near 4.5 Å. This modeled the high- $r$  data extremely well and allowed a determination of parameters for peaks below 3.8 Å, including most importantly the fraction,  $f_1$ , of Er on the Li-site.

Using the FT range 4.1-11.5 Å<sup>-1</sup> the Er L<sub>III</sub> data could be fit well to a Li-site model. For the checks of some Nb site occupation with Er-Nb and Er-O peaks (for an Nb site occupation) included, too many parameters are required[34] without additional constraints. To carry out this test some of the positions for the weaker peaks were fixed so that at least one degree of freedom remained. This still did not greatly improve the fit and by the criteria of the Hamilton F-test[? ], these additional peaks are not significant. Such fits place an upper limit of  $\sim 14$  % Nb occupation.

The overall result is that with a  $k$ -window that excludes a significant XANES contribution, we find that Er data is fit well with a lithium-site only model (some uncertainty between scans), with large positive shifts in pair distances due to the large ionic radius of Er. Since the fits including Nb site peaks were of similar quality (but with more parameters) to those for the Li site alone, we estimate that the Nb site occupation is  $\sim 5$ -10%, with a maximum upper bound of  $\sim 14$  %; this higher uncertainty of Nb site occupation compared to In is in part a result of the shorter FT range. We also tested whether the inclusion of an Er-Er peak (that would arise from clustering on two Li sites), would improve the fits. Based on the Hamilton F-test[? ] this peak was not significant and was not included in later fits. In the final fits using  $k^2$  weighting, a fit

Table 5.5: Table of significant fit parameters. Due to the relatively large ionic radius of Er, all significant peaks have a positive shift in bond length. Note the Er-O3 peak is a sum of peaks at 3.29 and 3.43 Å in undistorted crystal; average distance 3.36 Å. The difference between the stoichiometric and congruent sample is negligible.

Diff.		Er 0.55 mol%, sLNO		Er 2.3 mol%, cLNO	
Atom pair	$r$ (Å)	$r$ (Å)	$\sigma^2$ (Å <sup>2</sup> )	$r$ (Å)	$\sigma^2$ (Å <sup>2</sup> )
Er-O1	2.06	2.15	0.0030	2.15	0.0025
Er-O2	2.26	2.33	0.0056	2.34	0.0041
Er-Nb1	3.06	3.28	0.0035	3.29	0.0021
Er-O3	3.36	3.59	0.0052	3.56	0.0061
Er-Nb2	3.36	3.39	0.0057	3.43	0.0050

range of 1.1-4.6 Å, and an FT range 4.1-11.5 Å<sup>-1</sup>, 16 parameters were varied and 2 degrees of freedom remain. These fits for data at 10 K for the sLNO and cLNO samples are shown in Fig. 5.9 and the parameters are tabulated in Table 5.5.

The Hf  $r$ -space data, plotted in Fig. 5.7, show an interesting double-peak feature around 3.5 Å that is quite different from the corresponding data for other dopants, and suggests a mixture of Li and Nb site substitution. A similar model to that used for Er is applied for Hf – but starting with the fractions on the two sites more comparable. For the restricted range, 2.6-4.0 Å, on the EXAFS plot; the dominant Hf-Nb peaks are: two peaks for a Li site substitution (4 neighbors at 3.07 Å and 3 neighbors at 3.36 Å (actual distances)), and one peak for a Nb site substitution (6 neighbors at 3.77 Å). Although there are (weaker) Hf-O and multiscattering peaks in this range, an approximate fit can be achieved using only these peaks. The amplitudes of the peaks are constrained using the number of neighbors in each shell about Li and Nb, plus the fraction  $f_2$  (varying from 0 to 1), which represents the fraction of Hf on the Nb site;

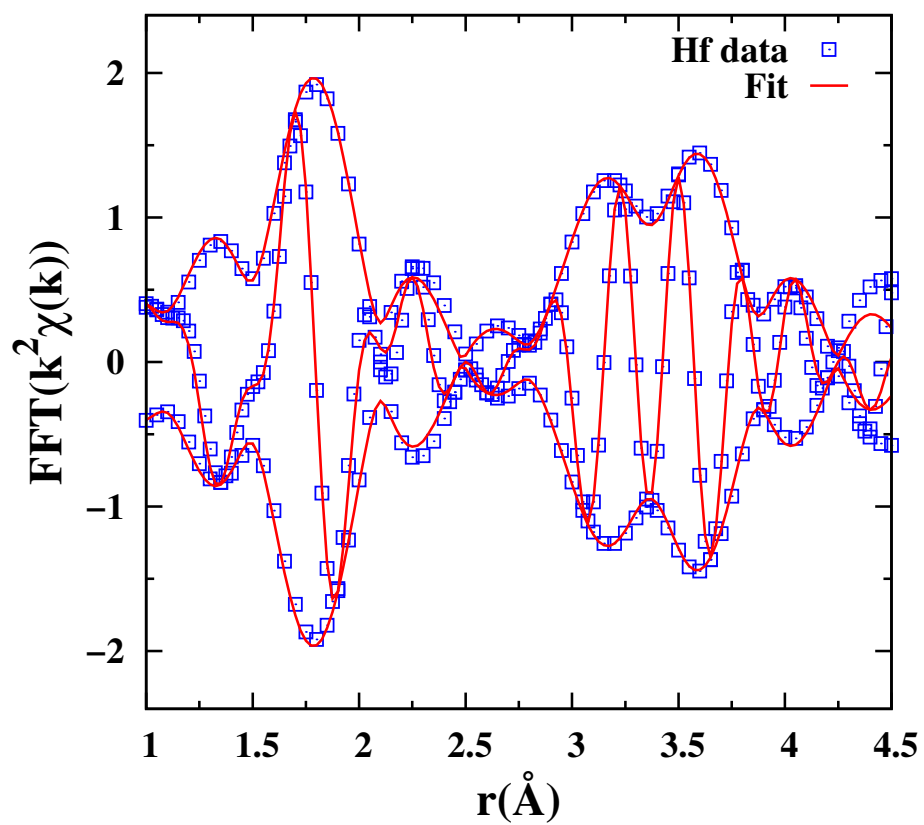


Figure 5.10: Fits of the 0.57 mol% Hf (sLNO) at 10 K (data - blue squares; fit - red line). A good fit is achieved up to 4.5 Å; see text for model and Table 5.6 for main parameters. The FT range is 3.8-12.7 Å<sup>-1</sup> with a Gaussian rounding of the FT window by 0.2 Å<sup>-1</sup>; the fit range is 1.0-4.2 Å.

Table 5.6: Fit parameters for the Hf L<sub>III</sub> edge data. The subscript on the pair indicates the substitution site, except for Hf-O2; this peak is the sum of three peaks at distances 2.06 and 2.26 Å from the Li site and 2.14 Å from the Nb site; average distance 2.15 Å (for 50 % occupation of each site). The average Li site Hf-O3 distance in the undistorted lattice is 3.36 Å, the average of 3.29 and 3.43 Å. Similarly the Nb site average Hf-O4 distance is 3.673 Å, the average of 3.620 and 3.73 Å. For this particular fit the fraction of Hf on an Nb site was 53%; however because of interference, the fit is sensitive to the initial parameters - in particular, the values for  $\sigma^2$  and the substitution site fraction are correlated. From many different fits the occupation is  $50 \pm 10\%$  on each site. The errors for  $\sigma^2$  are also large  $\sim 10\%$ .

Atom pair	Diff.	Hf 0.57 mol%, sLNO	
	$r$ (Å)	$r$ (Å)	$\sigma^2$ (Å <sup>2</sup> )
(Hf-O1) <sub>Nb</sub>	1.87	1.89(1)	0.0028
Hf-O2	2.15	2.08(1)	0.0013
(Hf-Nb) <sub>Li</sub>	3.07	3.13(1)	0.0043
(Hf-O3) <sub>Li</sub>	3.36	3.09(2)	0.0021
(Hf-Nb2) <sub>Li</sub>	3.36	3.54(2)	0.0013
(Hf-Nb3) <sub>Nb</sub>	3.77	3.75(2)	0.0015
(Hf-O4) <sub>Nb</sub>	3.67	3.72(4)	0.021

i.e.  $A_i = N_i f_2$  when Hf substitutes on Nb ( $N_i$  is the number of neighbors in the  $i^{\text{th}}$  shell about Nb), and  $A_i = N_i(1-f_2)$  for Hf on a Li site. For this restricted fit  $f_2 \sim 0.55$  and the position of the Hf-Nb peak for a Nb site substitution, shifted very little from that for the host distance. In contrast the Hf-Nb distances for the Li site substitutions increased considerably. In a full fit the positions of the Nb neighbors do not shift much from this restricted fit and the parameters are tabulated in Table 5.6. An example of the full fit which includes some longer multi-scattering (MS) peaks is shown in Fig. 5.10. From many different fits with O and MS peaks included, the fraction  $f_2$  is about  $50 \pm 10\%$ ; thus our result is that half of the Hf occupies the Li site and half occupies the Nb site.

### 5.2.6 Discussion

The important results from the detailed fits of the EXAFS data are: 1)  $\text{In}^{3+}$  substitutes primarily on the Li site and the results are nearly identical for two concentrations of cLNO (0.7 and 2.8 mol%); this result is very similar to that for the  $\text{Zn}^{2+}$  defect.[161] 2) Similarly for  $\text{Er}^{3+}$ , almost all Er is on the Li site ( $\sim 90\%$ ); the fraction on the Nb site for the sLNO sample (0.55 mol% Er) is consistently slightly larger (about 5%) than for cLNO sample (2.3 mol% Er) when the  $f_1$  parameter is allowed to vary in the fit. 3) The  $\text{Hf}^{4+}$  ion (0.57 mol% in sLNO) substitutes roughly half on a Li site and half on a Nb site. This is the first clear evidence for significant dopant occupation of the Nb site for any dopant we have studied, and to our knowledge no other EXAFS study has observed a large dopant fraction on Nb. 4) There is a significant difference in the magnitude and extent of local distortions about different types of dopant at comparable concentrations. The extent of disorder is very important as it leads to broadened optical and EPR linewidths and also changes the photo-conductivity. These results are inconsistent with a purely self-compensating scheme for each dopant (see scheme (ii) in section 5.2.1) and therefore require one and usually more nearby charge compensating defects; the most likely are Li vacancies,  $\text{V}_{\text{Li}}$ , but some  $\text{Nb}_{\text{Li}}$  may still exist, particularly for Hf. Since there are many nearby Li sites within a 6 Å radius about a Li site, a large number of possible distributions exist. What distributions form at high temperatures and are they in thermal equilibrium or meta-stable in nature?

The extent of local disorder deserved further discussion as it may broaden

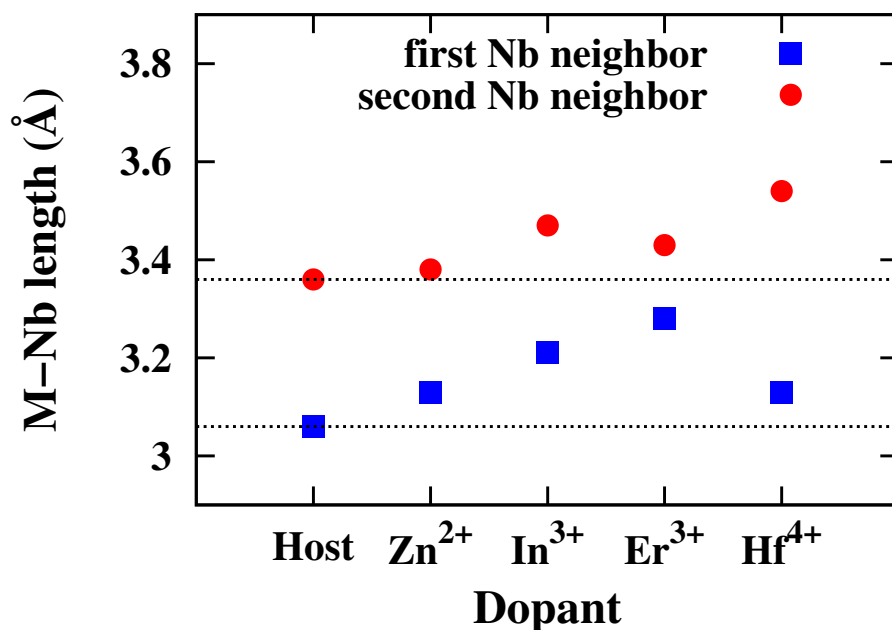


Figure 5.11: M-Nb distances for the first two Nb neighbors about the Li site vs type of dopant on the Li site. The dotted horizontal lines are the Li-Nb distances at 3.06 and 3.36 Å for the undistorted lattice. The M-Nb pair distances increase with valence (and also the dopant ionic radius) except for the Hf dopant.

optical linewidths in some applications. First we compare the average M-O distances in the first oxygen shell with the predictions from ionic radii (see Table 5.2). The measured average In-O bond length is 2.15 Å, only 0.03 Å smaller than predicted from ionic radii; similarly, the Er-O average bond length is 2.24 Å, again about 0.03 Å shorter than predicted from ionic radii. For Hf the difference is larger, but here Hf has a large occupation on both the Li and Nb sites. Including occupation fractions, the average weighted Hf-O distance is 2.03 Å, 0.06 Å shorter than that predicted from ionic radii. However the trend for the M-O bondlengths clearly agrees well with the ionic radii of the dopant cations.

Less well understood is that the ionic size and dopant valence also play a role in the displacements of the first few shells of Nb further neighbors about the Li site and hence the extent of disorder introduced into the lattice by different dopants.

The first two M-Nb pair distances are plotted in Fig. 5.11 vs type of dopant. Both distances increase as the dopant ionic radius increases from Zn to Er; however the shift is larger for the closest Nb atoms. Since in Fig. 5.1:top, the 3.06 Å Nb atoms are above the central Li while the 3.36 Å Nb atoms are below, it might be inferred that a difference in shifts of these two pair distances might indicate that the dopant atom is also slightly displaced from the Li site in LNO along the c-axis as proposed by Baumann *et al.*[167] However, one cannot easily distinguish between a displacement of the central atom and displacements of neighboring shells of atoms. We return to this aspect later when discussing some x-ray standing wave measurements. Also it is very unlikely that any dopants are on some other interstitial site; for a random site with low order, the peaks in the EXAFS would be strongly suppressed by the disorder, which is not observed. For the interstitial sites along the c-axis, the Nb neighbors would be closer than for the Li site - with one Nb neighbor very close at 1.94 Å. Such close Nb neighbors would be inconsistent with the data.

For Hf the situation is more complex; first note (Table 5.6) that for the fraction of Hf on an Nb site, the changes in pair distances compared to the host, are very small  $\leq 0.02$  Å. Much larger changes are observed for the fraction of Hf on a Li site; however, the displacement of the closest Nb neighbor is smaller ( $\sim 0.06$  Å) than for the second Nb neighbor ( $\sim 0.18$  Å). For the closest Nb neighbor, this may be a competition between the



small ionic radius for Hf (which would tend to shorten the distance) and the increased coulomb repulsion when  $\text{Hf}^{4+}$  replaces  $\text{Li}^+$  (which would lengthen it).

Three other EXAFS studies have investigated the local structure about several dopants in LNO, including the Er and Hf defects - but only collected data at room temperature.[168; 169; 170] The first EXAFS studies were done before the FEFF codes,[171; 172] that enabled detailed fits over several shells of neighbors, were readily available. In contrast, in our study, with good data out to much higher values of  $k$ , a detailed investigation of the 2nd and 3rd Nb neighbor environments is possible; this region in real-space is where the strongest fingerprint for Li or Nb site occupation resides, and our result contradicts some studies done with older analysis packages.

Prieto *et al.*[168; 169] indicated that they used the old theoretical phase and amplitude functions from McKale *et al.*[173] and reported that Hf substitutes on the Li site, but the room temperature data are very noisy. They find a broadened Hf-O peak (2.07 Å) for cLNO close to the average Hf-O distance we observe (2.03 Å), but for Hf-Nb, the dominant contribution they report is six Nb neighbors at 3.30 Å, with little evidence for a peak near 3.77 Å that would be indicative of some Nb substitution. A coordination number of six neighbors is not consistent with the Li site environment, unless for their shorter  $k$ -range, several Hf-Nb peaks could not be resolved, and are treated as a single peak. Note that their room temperature data do not show the double peak structure we observe between 3 and 4 Å for  $T = 10$  K; see Fig. 5.10. In a later study,[170] they use an early version of FEFF (FEFF3)[174] to calculate the EXAFS functions for neighbors about Hf, but used the same data[168]; the fit results for  $\text{LiNbO}_3\text{:Hf}$  are similar with

small shifts in the neighbor positions.

Zaldo and Prieto[169] also report that Er substitutes on the Li site for cLNO, for dopant concentrations within the range 0.5 to 1 mol%. Unfortunately, no data are shown but the fit results are tabulated. For Er, they report a very short Er-O distance (2.0 Å), even shorter than the average Li-O distance in pure LNO (2.16 Å), although the ionic radius of  $\text{Er}^{3+}$  is significantly larger than  $\text{Li}^+$ . The second Er-Nb peak is surprisingly long. Also the values of  $\sigma^2$  they report are very large (roughly a factor of 10 larger than reported here for 10K) indicating that the EXAFS are highly damped, and the local structure very disordered.

For  $\text{In}^{3+}$  and  $\text{Er}^{3+}$  substitutions, other types of probes generally agree with the primarily Li site substitution reported here, although the fraction of dopant on the Nb site is usually not provided. Kong *et al.*[175] propose that  $\text{In}^{3+}$  occupies Li sites for concentrations up to about 3 mol% based on  $\text{OH}^-$  IR spectroscopy, but for higher concentrations - near 5 mol% - some In moves onto the Nb site. Similarly Hauer *et al.* using Perturbed Angular Correlations (PAC)[176], find In on the Li site.

Rebouta *et al.*[177] have carried out PIXE/channeling experiments on Er doped cLNO and find a significant fraction of the Er is on a Li site. but suggest that at least 50 % of the Er is not on either the Li or Nb site, but instead on some interstitial site. However, interstitial sites have much closer Nb neighbors than do the Li and Nb lattice sites, and because of the large back-scattering from heavy Nb neighbors, this would provide a strong signature – a short M-Nb distance; that is not observed. In addition more disorder is expected around an interstitial site. Part of the difference with their

work might be attributed to a higher Er concentration (about 4 mol%) in their cLNO sample.

Gog *et al.*[178] and Baumann *et al.*[167] have used x-ray standing waves to investigate Er diffused into a cLNO crystal, in a region close to the crystal surface. They report substitution near the Li site but suggest that Er is displaced from the usual Li position by 0.46 Å along the c-axis with no distortion of the host lattice; on Fig. 5.1:top, this would be a -0.46 Å downward displacement of  $\text{Er}_{\text{Li}}$ . Although the local environment about Er is distorted the largest distortions we observe are < 0.23 Å; in addition all the Er-Nb pair distances increase which is not consistent with a simple downward displacement of Er, i.e. a large displacement of Er along the c-axis would make some Er-Nb pair distances longer and others shorter. Note also that for the nearest O atoms above and below  $\text{Er}_{\text{Li}}$ , the  $\text{Er}_{\text{Li}}$ -O distances both increase by comparable amounts (attributed to the much larger ionic radius for Er) which would be inconsistent with the above model with no distortion of the host lattice; if  $\text{Er}_{\text{Li}}$  is displaced, the first O shell follows it.

An important aspect for all compensated defects is that there must be many, slightly different local site distributions, consistent with the discussion above. This had been deduced explicitly from high resolution optical spectroscopy for the  $\text{Er}^{3+}$  ions, where many very sharp lines have been observed,[179; 180] and from EPR spectra where many lines are also observed.[181] In both cases, these complex spectra have been attributed to slightly different arrangements of the nearby charge compensating Li vacancies, but also from pairs or other clusters.[179] The EPR results have been

interpreted in terms of a statistical distribution of  $V_{Li}$  on nearby Li sites.[181] So far however the specific local distributions of other defects have not yet been determined. Also note that the relatively small size of  $\sigma^2$  for all atom-pairs in the EXAFS analysis (Table 5.4, 5.5, and 5.6) means that the environments about each dopant are very nearly the same i.e. well ordered; any variations in the arrangements of  $V_{Li}$  compensators do not provide much variation in the local disorder, even when it is distorted.

For Hf, Hammoum *et al.*[182] used Raman spectroscopy to study a doped cLNO crystal. They argue that at low concentrations, Hf replaces the  $Nb_{Li}$  antisite defects, while at high concentrations above  $\sim 4.5$  mol%, Nb sites also become occupied. Their results are qualitative as no occupation fractions are given. It is likely that their high concentration samples are more comparable to the sLNO samples studied here, as then all the  $Nb_{Li}$  antisites are likely filled. Kovács *et al.*[159] also find that above a threshold concentration a small fraction of Hf occupies the Nb site.

Marques *et al.*[183] use a combination of Rutherford back scattering and channeling (RBS/C) and PAC to investigate the substitution site(s) in a near-stoichiometric crystal with 1 mol% Hf, and a cLNO crystal with  $\sim 6$  mol% Hf. They also found Hf substitutes on both sites, with more Hf on the Nb site for the near stoichiometric sample but more on the Li site for the cLNO sample. Qualitatively, the site fractions are similar to our results; however they report that there are two different  $Hf_{Nb}$  sites with one of them displaced by 0.1 Å. This would introduce considerable disorder about the  $Hf_{Nb}$  sites. A striking aspect of the EXAFS results is that for the fraction of Hf on a Nb site, distortions of the first O and Nb shells are very small ( $\sim 0.02$  Å) and the disorder ( $\sigma^2$ )

is also small.

These EXAFS results do not agree as well with some calculations using pair potentials[29; 5; 6] – see introduction for a brief summary of such results. For In, the EXAFS are consistent with scheme (i), in which all  $\text{In}^{3+}$  are on a Li site in cLNO; this also agrees with the DFT calculations for 3+ ions,[30] assuming that the chemical potential is close to that for cLNO. Using pair potentials however, the lowest solution energy scheme is the self compensating model (ii);[5] if these theoretical results[5] at 0 and 293 K are extrapolated to high temperatures, scheme (i), with all In on a Li site, eventually becomes the lowest solution energy – see Fig. 5.12:Top.

For Er, the EXAFS results suggest a similar scheme to In [scheme (i) – 90 % on Li]. The major difference between trivalent In and Er is the ionic radius, where Er is considerably larger. In the DFT calculations[30] Er is on a Li site (scheme (i)) for a chemical potential close to cLNO while it is self-compensated (scheme (ii)) if the chemical potential is close to that for stoichiometric material, but the disparity in ionic radius between Er and Nb implies a bias for scheme (i). We find no significant difference in local structure between Er-doped cLNO and sLNO. Even though Er and In share a similar doping scheme the local environment around the impurity differs, as is evident in the larger M-Nb bond-length shifts in LNO:Er and in the increased amount of disorder observed in the k-space data in Fig. 5.5; we believe this is due to the difference in ionic radii. Subtle differences in the defect complex (impurity atom plus surrounding charge compensating defects) are significant when trying to carefully control optoelectronic response in engineered devices.

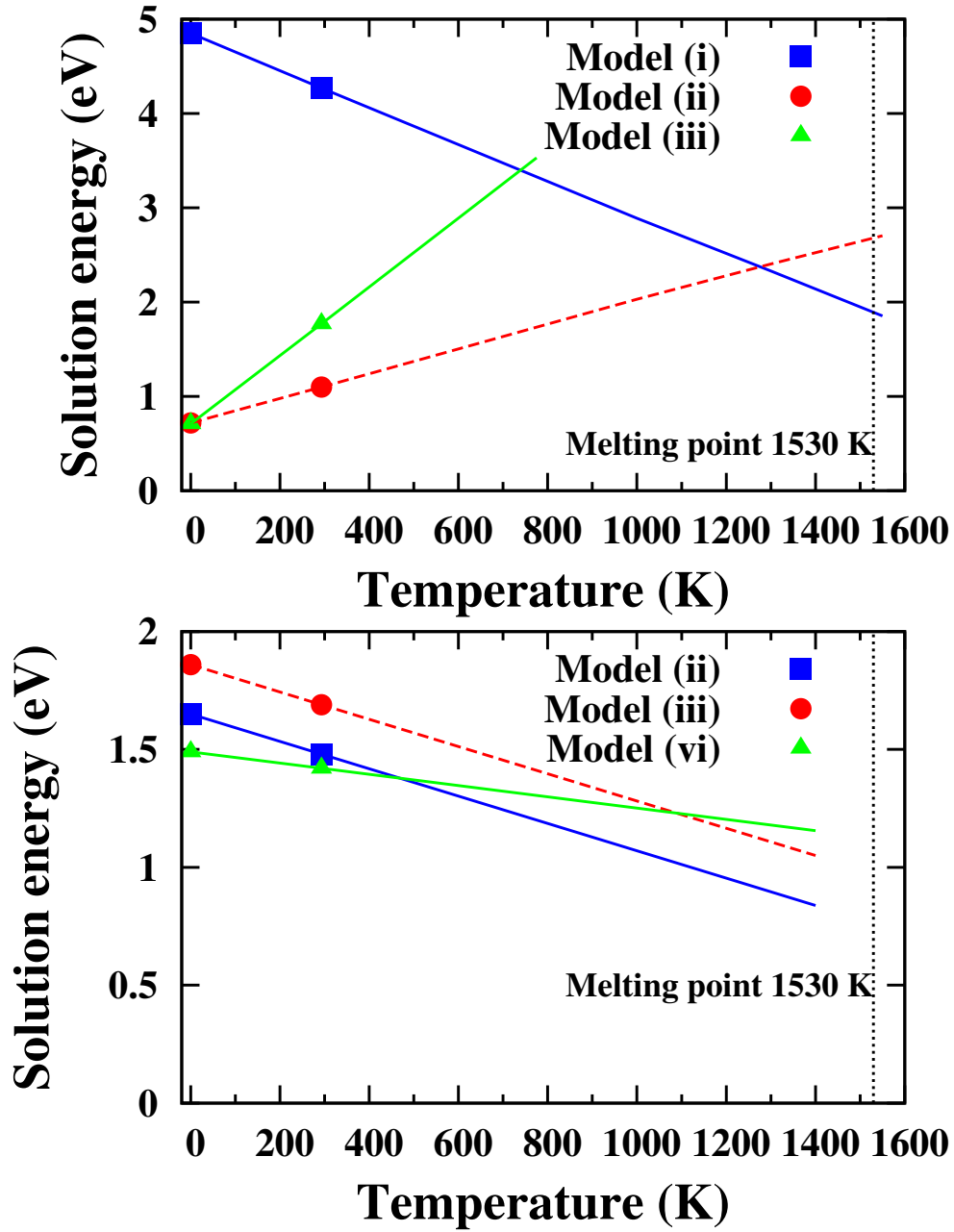


Figure 5.12: Top: Plot of the solution energies of In dopants for models (i), (ii) , and (iii) of Ref. [5] as a function of T to show extrapolations to higher T. These extrapolations suggest that the lowest energy model may change when the defect is frozen in at high temperatures, thus motivating defect calculations at much higher temperatures. Bottom: Similar extrapolations for the three lowest energies for Hf dopants[6]. Although scheme (vi) is lowest below room temperature, scheme (ii) is lower at high T.

For a low concentration Hf dopant in sLNO, the EXAFS results indicate an approximate 50-50 occupation of the Li and Nb sites. For this dopant, calculations[6] using pair potentials at 293 K indicate that scheme (vi) [all Hf on Nb] has the lowest solution energy, but only slightly lower than scheme (ii) [25 % Hf on Li] as shown in Fig. 5.12:Bottom. However, to have the 50-50 occupation on the two sites means there must also be a significant contribution from scheme (i), with all Hf on a Li site. Why the fraction of Hf on a Li site must be large is not clear as scheme (i) has a large solution energy.

These results raise several issues about the assumptions on which the calculations are based. First the samples are grown at very high temperatures (melting point about 1530 K) and as solidification takes place, are the dopant atoms uniformly distributed? At these high temperatures is there a different preference for the substitution site? Second as the crystal cools slowly, are the locations of the heavy atoms (including the dopants), quenched in, or is diffusion sufficient to allow for equilibrium to be achieved? Alternatively, are the room temperature samples in a meta stable state? Light Li ions diffuse easily[184] at 250 °C and consequently  $V_{Li}$  can easily provide charge compensation for a wide range of temperatures. Since there are many nearby locations for  $V_{Li}$  charge compensators, a large number of slightly different dopant-compensator complexes are possible as observed for  $Er^{3+}$ , [179; 181] and likely exist for all other dopants. In contrast, heavy atoms diffuse much more slowly – for example even the relatively light Ti atom takes 50 hrs at  $\sim 1370$  K to diffuse a few micron.[149] Much heavier atoms such as Nb may be frozen in place at temperatures just below the melting

point.

For the large fraction of dopants on the Li site, Li vacancies ( $V'_{\text{Li}}$ ) are needed for charge compensation. The vector between the dopant and  $V'_{\text{Li}}$  defines an axis for this complex defect, with one  $V'_{\text{Li}}$  vacancy (axes for dopants with more than one  $V'_{\text{Li}}$  vacancy can also be defined, but more complicated). This raises a challenging experimental question: can the orientation of these defect axes be controlled and thus optimize the optical properties of the system? In the 70's, F. Lüty and co-workers studied a range of compact defects for which the principal defect axis could be rotated using polarized light. For example the axis of the  $F_A$  center (an F center adjacent to a  $\text{Na}^+$  impurity in KCl, with the defect axis along one of the  $[100]$  axes) is easily rotated even at low temperatures,[185] and under appropriate conditions most of the  $F_A$  centers can be aligned along a specific  $[100]$  axis.

The dopant- $V'_{\text{Li}}$  defects are even more complex in that the distance between the dopant and Li vacancy can also vary significantly. Dierolf and Sandmann[180] observed several different emission lines for Er ions in LNO, and were able to associate them with different arrangements of the two Li vacancies required for charge compensation. The distribution of  $V'_{\text{Li}}$  could also be changed by annealing for 5 hr at 250 C; but at room temperature the vacancy distributions were meta stable. A similar situation occurs for  $\text{CaF}_2:\text{Yb}$  where interstitial  $F_i^-$  defects provide charge compensation for  $\text{Yb}^{3+}$  dopants. In this system as discussed in Ch. 4 we recently observed several meta-stable defect configurations[80] that could be changed by a combination of x-ray exposure and annealing. In that case, the changing optical properties appear to depend on the sepa-



ration between the Yb and  $F_i^-$  defects, and for one configuration an anomalous optical emission was quenched[80].

It appears that meta-stable configurations of the dopant-compensator defect clearly exist for doped  $\text{LiNbO}_3$ . These ideas likely can be applied to a wide range of doped materials with complex defects both compact defects involving say a neighboring pair of atoms as for the  $F_A$  center[185] or for extended defects for which a dopant and charge compensating defect may be well separated, as found for  $\text{CaF}_2\text{:Yb}$ , see Ch. 4. Although the orientation of compact defects with a well defined axis have been studied extensively – e.g. the  $F_A$  center[185] or isovalent off-center defects[186; 187] – systems with aliovalent dopants, such as the dopants in LNO discussed here, the  $\text{CaF}_2\text{:Yb}$  system[80], and dopants in ferroelectrics,[188] are more challenging as the related charge compensating defect can be several lattice spacings away.

If means are found to control the location of the charge compensating Li vacancies in LNO - both separation between dopant and vacancies, and/or the orientation of the axes from the dopant to the vacancies in LNO - it would provide new ways of optimizing the optical behavior of this unusual material.

## 5.3 Experimental details

### 5.3.1 Zinc

EXAFS data were collected at the Zn K edge in fluorescence mode, for Zn doped stoichiometric  $\text{LiNbO}_3$ , using beam line 4-1 at the Stanford Synchrotron Radi-

ation Lightsource (SSRL). Data were collected at 10 K in an Oxford helium cryostat, using a 220 monochromator, with a slit size of 0.5 mm; energy resolution was 0.9 eV. Harmonic content was reduced by detuning the monochromator 50 % at 9800 eV. For the earlier work on cLNO, the energy resolution was 1.9 eV using a 111 monochromator[128].

The stoichiometric  $\text{LiNbO}_3$  crystal doped with nominally 1 mol% ZnO was grown using the high temperature top seeded solution growth method with  $\text{K}_2\text{O}$  flux[146]. The Zn concentration in a different piece of sample, cut from the middle part of the crystal, was about 0.66 mol% as determined by atomic absorption spectrometry (AAS). The crystal was above the photorefractive damage threshold, checked by measuring the IR absorption spectrum of hydroxyl ions always present in as-grown LNO crystals[159]. A Zn concentration was also estimated from the Zn and Nb edge step heights for the EXAFS sample - 0.74 mol%. Considering the samples were from different parts of the boule, these results are consistent; we'll use the average concentration 0.7 mol%. We also remeasured concentrations in the earlier samples[128] as there was an error in converting x-ray step heights to relative concentrations; the correct concentrations are: 4.4 mol% (nom. 5 mol%); 5.3 mol% (nom. 7 mol%); 6.0 mol% (nom. 9 mol%); we use these in the later comparisons.

For the EXAFS experiments, a small amount of material was powdered and mounted on tape; the resulting particle sizes were  $\leq 5 \mu\text{m}$ . Four layers of tape were loaded into the cryostat for the x-ray measurements. Details about the EXAFS technique are provided in our earlier study[128] – the procedures for the sLNO study are nearly identical to that work.

### 5.3.2 In, Er, Hf

In-doped  $\text{LiNbO}_3$  crystals were purchased from Impex High Tech, Germany, with nominal (melt) In concentrations of 1 and 4 mol%. The actual In concentrations, measured from the ratio of the In and Nb edge step heights[189; 161], are 0.7 and 2.8 mol%. The Er- and Hf-doped crystals were grown at the Wigner Research Centre in Budapest. A cLNO crystal doped with 6 mol% Er was grown from melt by the Czochralski method. The other Er- and the Hf-doped sLNO crystal were grown from solution using the high temperature top seeded solution growth method[190]. For the Er doped  $\text{LiNbO}_3$  crystals the defect concentration is  $0.55 \pm 0.11$  mol% in sLNO[165] and  $2.3 \pm 0.15$  mol% in cLNO; the latter was measured using the inductively coupled plasma optical emission spectrometry (ICP-OES) method. Finally, the Hf concentration in sLNO is  $0.57 \pm 0.02$  mol%, using the inductively coupled plasma mass spectrometry (ICP-MS) method. For each material, powdered samples for EXAFS measurements were prepared as described in Ref. [128]; a summary of samples and concentrations is given in Table 5.3.

EXAFS data were collected at the In K edge in fluorescence mode, for 0.7 and 2.8 mol% In doped congruent  $\text{LiNbO}_3$ , using beamline 4-1 at the Stanford Synchrotron Radiation Lightsource (SSRL). Data were collected at 10 and 300 K in an Oxford helium cryostat, using a 220 monochromator; a slit size of 0.3 mm provided an energy resolution of 4.0 eV. Harmonic content was reduced by detuning the monochromator 50 % at 28,100 eV.

Data for the Er doped samples were collected at the Er L<sub>III</sub> edge in fluorescence mode on beamline 4-1 at 10 K; a 220 monochromator was used with a vertical slit size of 0.6 mm, giving an energy resolution of 0.8 eV. Harmonic content was reduced by detuning the monochromator 50 % at 8600 eV. Finally 10 K data at the Hf L<sub>III</sub> edge for sLNO:Hf were collected in fluorescence mode using the focused beamline 9-3, with vertical slit size of 0.2 mm.

The EXAFS data were reduced and the  $k$ -space functions obtained at each edge using the program RSXAP[23], which uses standard techniques to remove the backgrounds, below and above the edge. Examples of the  $k$ -space data ( $k^2$  weighting) for each edge are shown in Fig. 5.5.

# Bibliography

- [1] A. Wakamiya, M. Endo, T. Sasamori, N. Tokitoh, Y. Ogomi, S. Hayase, and Y. Murata, *Chem. Lett.* **43**, 711 (2014).
- [2] F. Hao, C. C. Stoumpos, Z. Liu, R. P. H. Chang, and M. G. Kanatzidis, *J. Am Chem* **136**, 16411–16419 (2014).
- [3] D. S. Yang, D. R. Fazzini, T. I. Morrison, L. Tröger, and G. Bunker, *Journal of Non-Crystalline Solids* **210**, 275 (1997).
- [4] A. L. Ankudinov, B. Ravel, J. J. Rehr, and S. D. Conradson, *Phys. Rev. B* **58**, 7565 (1998).
- [5] R. M. Araujo, M. E. G. Valerio, and R. A. Jackson, *J. Phys. Condes. Matt.* **20**, 035201 (2008).
- [6] R. M. Araujo, M. E. G. Valerio, and R. A. Jackson, *Crystals* **8**, 123 (2018).
- [7] R. D. Shannon, *Acta Crystallogr. A* **32**, 7519 (1976).
- [8] T. Leijtens, G. E. Eperon, A. J. Barker, G. Grancini, W. Zhang, J. M. Ball, A. R. S. Kandada, H. J. Snaith, and A. Petrozza, *Energy Environ. Sci.* **9**, 3472 (2016).
- [9] A. Ashkin, G. D. Boyd, J. M. Dziedzic, R. G. Smith, A. A. Ballman, J. J. Levinstein, and K. Nassau, *Applied Physics Letters* **9**, 72 (1966).
- [10] J. Zhang, Y. Chen, F. Lu, W. Lu, W. Dang, X. Chen, and Y. Xia, *Applied optics* **46**, 7792 (2007).
- [11] W. Yang, J. Noh, N. Jeon, Y. Kim, S. Ryu, J. Seo, and S. Seok, *Science* **348**, 1234 (2015).
- [12] T. Brenner, D. Egger, L. Kronik, G. Hodes, and D. Cahen, *Nat.Rev.Mat* **1**, (2016).
- [13] Y. Rakita, O. Bar-Eli, E. Meirzadeh, H. Kaslasi, Y. Peleg, G. Hodes, and I. Lubomirsky, *PNAS* **114**, E5504 (2017).
- [14] D. Cahen and I. Lubomirsky, *Acc.Chem.Res.* **50**, 573 (2017).

- [15] M. Sendner, P. Nayak, and D. e. a. Egger, Mater.Horiz. **3**, (2016).
- [16] A. Beecher, O. Semonin, J. Skelton, J. Frost, M. Terban, H. Zhai, A. Alatas, J. Owen, and A. B. S. Walsh, ACS energy Letters **1**, 880 (2016).
- [17] J. Choi, X. Yang, Z. Norman, S. Billinge, and J. Owen, Nano Lett. **14**, (2014).
- [18] A. Posglitch and D. Weber, J.Chem.Phys. **87**, (1987).
- [19] C. Stoumpos, C. Malliakas, and M. Kanatzidis, Inorganic Chem. **52**, 9019 (2013).
- [20] P. S. Whitfield, N. Herron, W. E. Guise, K. Page, Y. Q. Cheng, I. Milas, and M. K. Crawford, Scientific Reports **6**, 35685 (2016).
- [21] E. Mosconi, C. Quarti, T. Ivanovska, G. Ruani, and F. Angelis, Phys.Chem. **16**, (2014).
- [22] O. Yaffe and Y. e. a. Guo, Phys.Rev.Lett. **118**, (2017).
- [23] C. H. Booth, *R-Space X-ray Absorption Package*, 2010, 2010, <http://lise.lbl.gov/R SXAP/>.
- [24] D. S. McClure and C. Pédrini, Phys. Rev. B **32**, 8465 (1985).
- [25] B. Moine, B. Courtois, and C. Pédrini, J. Phys. France **50**, 2105 (1989).
- [26] P. Dorenbos, J. Phys.: Condens. Matter **15**, 2645 (2003).
- [27] X. Zhen, Q. Li, and Y. Xu, Cryst. Res. Technol. **41**, 276 (2006).
- [28] U. Schlarb and K. Betzler, Phys. Rev. B **50**, 751 (1994).
- [29] R. M. Araujo, K. Lengyel, R. A. Jackson, L. Kovacs, and M. E. G. Valerio, J. Phys. Condes. Matt. **19**, 46211 (2007).
- [30] H. Xu, A. Chernatynskiy, D. Lee, S. B. Sinnott, V. Gopalan, V. Dierolf, and S. R. Phillpot, Phys. Rev. B **82**, 184109/ (2010).
- [31] P. Eisenberger and G. S. Brown, Solid State Commun. **29**, 418 (1979).
- [32] G. Bunker, Nuclear Instruments and Methods **207**, 437 (1983).
- [33] F. Bridges, G. G. Li, and X. Wang, Nucl. Inst & Meth. in Phys. **A320**, 548 (1992).
- [34] E. A. Stern, Phys. Rev. B **48**, 9825 (1993).
- [35] A. Sharenko, C. Mackeen, L. Jewell, F. Bridges, and M. F. Toney, Chemistry of Materials **29**, 1315 (2017).
- [36] N.-g. Park, Today **18**, 65 (2015).

- [37] J. Berry, T. Buonassisi, D. A. Egger, G. Hodes, L. Kronik, Y.-l. Loo, I. Lubomirsky, S. R. Marder, Y. Mastai, and J. S. Miller, *Adv. Mater.* 2015 **27**, 5102 .
- [38] *National Renewable Energy Laboratory Efficiency Chart* (PUBLISHER, ADDRESS, 2016).
- [39] S. D. Stranks, P. K. Nayak, W. Zhang, T. Stergiopoulos, and H. J. Snaith, *Cells Angew. Chem Int. Ed* **54**, 3240 (2015).
- [40] A. Sharenko and M. F. Toney, *J. Am. Chem. Soc* **138**, 463 (2016).
- [41] Q. Wang, Y. Shao, Q. Dong, Z. Xiao, Y. Yuan, and J. Huang, *Environ. Sci.* **7**, 2359 (2014).
- [42] K. Yan, M. Long, T. Zhang, Z. Wei, H. Chen, S. Yang, and J. Xu, *J. Am. Chem. Soc.* **137**, 4460 (2015).
- [43] W. Zhang, M. Saliba, D. T. Moore, S. K. Pathak, M. T. H"orantner, T. Stergiopoulos, S. D. Stranks, G. E. Eperon, J. A. Alexander-Webber, and A. Abate, *Nat. Commun.* **6**, 6142 (2015).
- [44] G. E. Eperon, S. D. Stranks, C. Menelaou, M. B. Johnston, L. M. Herz, and H. J. Snaith, *Environ. Sci.* **7**, 982 (2014).
- [45] J. H. Heo, D. H. Song, H. J. Han, S. Y. Kim, J. H. Kim, D. Kim, H. W. Shin, T. K. Ahn, C. Wolf, and T.-w. Lee, *Adv. Mater.* **27**, 3424 3430 (2015).
- [46] S. H. Im, J.-h. Heo, H. J. Han, D. Kim, and T. Ahn, *Energy Enivorn. Sci* **8**, 1602 (2015).
- [47] D. P. McMeekin, G. Sadoughi, W. Rehman, G. E. Eperon, M. Saliba, M. T. H"orantner, A. Haghighirad, N. Sakai, L. Korte, and B. A. Rech, *Science* **351**, 151 (2016).
- [48] R. A. Kerner, L. Zhao, Z. Xiao, and B. P. Rand, *J. Mater. Chem* **4**, 8308 (2016).
- [49] K. G. Stamplecoskie, J. S. Manser, and P. V. Kamat, *Energy Environ. Sci* **8**, 208 (2015).
- [50] B.-k. Teo, *Exafs: Basic Principles and Data Analysis* (Springer: Dordrecht, The Netherlands, ADDRESS, 1986).
- [51] J. J. Rehr and R. C. Albers, *Rev. Mod. Phys.* **72**, 621 (2000).
- [52] A. Meents, S. Gutmann, A. Wagner, and C. Schulze-Bries, *Proc. Natl. Acad. Sci. U. S. A.* **107**, 1094 (2010).

- [53] G. Meitzner, J. Gardea-Torresdey, J. Parsons, S. L. Scott, and E. W. Deguns, *Microchem. J* **81**, 61 (2005).
- [54] P. Frank, M. Benfatto, M. Qayyam, B. Hedman, Hodgson, and K. O., *J. Chem. Phys.* **142**, 084310 (2015).
- [55] T. Keiber, F. Bridges, R. E. Baumbach, and M. B. Maple, *Phys. Rev. B* **86**, 174106 (2012).
- [56] A. L. Ankudinov and J. J. Rehr, *Phys. Rev B: Condens. Matter Mater* **56**, R1712 (1997).
- [57] L. Downward, C. H. Booth, W. W. Lukens, and F. Bridges, *AIP Conference Proceedings* **882**, 129 (2007).
- [58] I. Persson, K. Lyczko, D. Lundberg, L. Eriksson, and A. Placzek, *Inorg. Chem.* **50**, 1058 (2011).
- [59] Y. Guo, K. Shoyama, W. Sato, Y. Matsuo, K. Inoue, K. Harano, C. Liu, H. Tanaka, and E. Nakamura, *J. Am. Chem. Soc.* **137**, 15907 (2015).
- [60] J. A. McLeod, Z. Wu, B. Sun, and L. Liu, *Nanoscale* **8**, 6361 (2016).
- [61] J. S. Manser, B. Reid, and P. V. Kamat, *J. Phys. Chem.* **119**, 17065 (2015).
- [62] F. Huang, Y. Dkhissi, W. Huang, M. Xiao, I. Benesperi, S. Rubanov, Y. Zhu, X. Lin, L. Jiang, and Y. Zhou, *Nano Energy* **10**, 10 (2014).
- [63] Y. Deng, E. Peng, Y. Shao, Z. Xiao, Q. Dong, and J. Huang, *Energy Environ. Sci.* **8**, 1544 (2015).
- [64] M. Xiao, F. Huang, W. Huang, Y. Dkhissi, Y. Zhu, J. Etheridge, A. Gray-Weale, U. Bach, Y.-b. Cheng, and L. A. Spiccia, *Angew Chem* **126**, 10056 (2014).
- [65] W. Ostwald, *Z. Phys. Chem.* **22**, 289 (1897).
- [66] Y. Tidhar, E. Edri, H. Weissman, D. Zohar, G. Hodes, D. Cahen, B. Rybtchinski, and S. Kirmayer, *J. Am. Chem. Soc.* **136**, 13249 (2014).
- [67] C. M. M. Soe, C. C. Stoumpos, B. Harutyunyan, E. F. Manley, L. X. Chen, M. J. Bedzyk, T. J. Marks, and M. G. Kanatzidis, *ChemSusChem* **9**, 2656 (2016).
- [68] G. Li, T. Zhang, and Y. Zhao, *J. Mater. Chem.* **3**, 19674 (2015).
- [69] C.-c. Chueh, C.-y. Liao, F. Zuo, S. T. Williams, P.-w. Liang, and A. K.-y. Jen, *J. Mater. Chem* **3**, 9058 (2015).
- [70] C. Zuo and L. Ding, *Nanoscale* **6**, 9935 (2014).



- [71] S. J. Yoon, K. G. Stamplecoskie, and P. V. Kamat, *J. Phys. Chem Lett* **7**, 1368 (2016).
- [72] M. Hambsch, Q. Lin, A. Armin, P. L. Burn, and P. Meredith, *J. Mater. Chem.* **4**, 13830 (2016).
- [73] W. Qiu, T. Merckx, C. Jaysankar, M. Masse de la Huerta, L. Rakocevic, W. Zhang, U. W. Paetzold, R. Gehlhaar, L. Froyen, and e. a. Poortmans, *J, Energy Environ. Sci.* **9**, 484 (2016).
- [74] J. H. Heo, D. H. Song, and S. H. Im, *Advanced Materials* **26**, 8179 (2014).
- [75] E. Edri, S. Kirmayer, D. Cahen, and G. Hodes, *The Journal of Physical Chemistry Letters* **4**, 897 (2013).
- [76] J. Huang, S. Xiang, J. Yu, and C.-Z. Li, *Energy Environ. Sci.* (2019).
- [77] T. D. McFarlane, C. S. De Castro, P. J. Holliman, and M. L. Davies, *Chem. Commun.* **55**, 35 (2019).
- [78] M. Baranowski, J. M. Urban, N. Zhang, A. Surrente, D. K. Maude, Z. Andaji-Garmaroudi, S. D. Stranks, and P. Plochocka, *The Journal of Physical Chemistry C* **122**, 17473 (2018).
- [79] C. MacKeen, F. Bridges, M. Kozina, A. Mehta, M. F. Reid, J.-P. R. Wells, and Z. Barandiarán, *J. Phys. Chem. Lett.* **8**, 3313 (2017).
- [80] C. MacKeen, F. Bridges, L. Seijo, Z. Barandiarán, M. Kozina, A. Mehta, M. F. Reid, and J.-P. R. Wells, *J. Phys. Chem. C* **121**, 28435 (2017).
- [81] A. A. Kaplyanskii and P. P. Feofilov, *Opt. Spectrosc.* **13**, 129 (1962).
- [82] E. G. Reut, *Opt. Spectrosk.* **40**, 99 (1976).
- [83] E. van der Kolk, P. Dorenbos, J. T. M. de Haas and C. W. E. van Eijk, *Phys. Rev. B* **71**, 045121 (2005).
- [84] C. Pédrini, *Phys. Status Solidi A* **202**, 185 (2005).
- [85] M. F. Reid, P. S. Senanayake, J.-P. R. Wells, G. Berden, A. Meijerink, A. J. Salkeld, C.-K. Duan, and R. J. Reeves, *Phys. Rev. B* **84**, 113110 (2011).
- [86] P. S. Senanayake, J. P. R. Wells, M. F. Reid, G. Berden, A. Meijerink and R. J. Reeves, *J. Lumin.* **133**, 81 (2013).
- [87] R. B. Hughes-Currie, A. J. Salkeld, K. V. Ivanovskikh, M. F. Reid, J.-P. R. Wells, and R. J. Reeves, *J. Lumin.* **158**, 197 (2015).
- [88] Z. Barandiarán and L. Seijo, *J. Chem. Phys.* **141**, 234704 (2014).

- [89] C. R. A. Catlow, A. V. Chadwick, G. N. Greaves, and L. M. Moroney, *Nature* **312**, 601 (1984).
- [90] V. Petit, P. Camy, J.-L. Doualan, X. Portier, and R. Moncorgé, *Phys. Rev. B* **78**, 085131 (2008).
- [91] R. B. Hughes-Currie, K. V. Ivanovskikh, J.-P. R. Wells, M. F. Reid, and R. A. Gordon, *J. Phys.: Condens. Matter* **28**, 135502 (2016).
- [92] M. R. Antonio, L. Soderholm, and I. Song, *J. Appl. Electrochem.* **27**, 784 (1997).
- [93] R. B. Hughes-Currie, K. V. Ivanovskikh, J.-P. R. Wells, M. F. Reid, R. A. Gordon, L. Seijo, and Z. Barandiarán, *J. Phys. Chem. Lett.* **8**, 1175 (2017).
- [94] B. Welber, *J. Chem. Phys.* **42**, 4262 (1965).
- [95] D. S. McClure and Z. Kiss, *J. Chem. Phys.* **39**, 3251 (1963).
- [96] L. D. DeLoach, S. A. Payne, L. L. Chase, L. K. Smith, W. L. Kway, and W. F. Krupke, *Evaluation of Absorption and Emission Properties of Yb<sup>3+</sup> Doped Crystals for Laser Applications*, 1993.
- [97] W. F. Krupke, *IEEE J. Quantum Electron.* **6**, 1287 (2000).
- [98] A. Lucca, G. Debourg, M. Jacquemet, F. Druon, F. Balembois, and P. Georges, *Opt. Lett.* **29**, 2767 (2004).
- [99] M. K. Ashurov, S. T. Boibobeva, I. Nuritdinov, E. A. Garibin, A. A. Demidenko, S. V. Kuznetsov, and P. P. Fedorov, *Inorg. Mater.* **52**, 842 (2016).
- [100] P. P. Feofilov, *Opt. Spektrosk.* **1**, 992 (1956).
- [101] C. MacKeen, F. Bridges, M. Kozina, A. Mehta, M. F. Reid, J.-P. R. Wells, and Z. Barandiarán, *J. Phys. Chem. Lett.* **8**, 3313 (2017).
- [102] S. M. Kaczmarek, T. Tsuboi, M. Ito, G. Boulon, and G. Leniec, *J. Phys.: Condens. Matter* **17**, 3771 (2005).
- [103] I. Nicoara, L. Lighezan, M. Enculescu, and I. Enculescu, *J. Crys. Growth* **310**, 2026 (2008).
- [104] J. L. Merz and P. S. Pershan, *Phys. Rev.* **162**, 217 (1967).
- [105] J. L. Merz and P. S. Pershan, *Phys. Rev.* **162**, 235 (1967).
- [106] M. Douglas and N. M. Kroll, *Ann. Phys. (N.Y.)* **82**, 89 (1974).
- [107] B. A. Hess, *Phys. Rev. A* **33**, 3742 (1986).

- [108] B. A. Hess, C. M. Marian, U. Wahlgren, and O. Gropen, *Chem. Phys. Lett.* **251**, 365 (1996).
- [109] Z. Barandiarán and L. Seijo, *J. Chem. Phys.* **89**, 5739 (1988).
- [110] L. Seijo and Z. Barandiarán, in *Computational Chemistry: Reviews of Current Trends*, edited by J. Leszczyński (World Scientific, Singapore, 1999), Vol. 4, pp. 55–152.
- [111] A. Gellé and M.-B. Lepetit, *J. Chem. Phys.* **128**, 244716 (2008).
- [112] B. O. Roos, R. Lindh, P. A. Malmqvist, V. Veryazov, P. O. Widmark and A. C. Borin, *J. Phys. Chem. A* **112**, 11431 (2008).
- [113] B. O. Roos, P. R. Taylor, and P. E. M. Siegbahn, *Chem. Phys.* **48**, 157 (1980).
- [114] P. E. M. Siegbahn, A. Heiberg, J. Almlöf, and B. O. Roos, *J. Chem. Phys.* **74**, 2384 (1981).
- [115] P. J. J. Olsen, B. O. Roos and J. A. Jensen, *J. Chem. Phys.* **89**, 2185 (1988).
- [116] P.-A. Malmqvist, A. Rendell, and B. O. Roos, *J. Phys. Chem.* **94**, 5477 (1990).
- [117] P.-Å. Malmqvist, K. Pierloot, A. R. Moughal Shahi, C. J. Cramer and L. Gagliardi, *J. Chem. Phys.* **128**, 204109 (2008).
- [118] K. Andersson, P.-A. Malmqvist, B. O. Roos, A. J. Sadlej, and K. Wolinski, *J. Phys. Chem.* **94**, 5483 (1990).
- [119] K. Andersson, P.-A. Malmqvist, and B. O. Roos, *J. Chem. Phys.* **96**, 1218 (1992).
- [120] A. Zaitsevskii and J.-P. Malrieu, *Chem. Phys. Lett.* **233**, 597 (1995).
- [121] J. Finley, P.-A. Malmqvist, B. O. Roos, and L. Serrano-Andrés, *Chem. Phys. Lett.* **288**, 299 (1998).
- [122] G. Karlström, R. Lindh, P. A. Malmqvist, B. O. Roos, U. Ryde, V. Veryazov, P. O. Widmark, M. Cossi, B. Schimmelpfennig, P. Neogrady, and L. Seijo, *Comput. Mater. Sci.* **28**, 222 (2003).
- [123] H. Chen, X. He, C. Sheng, Y. Ma, H. Nie, W. Xia, and W. Ying, *Int. J. Physiol. Pathophysiol. Pharmacol.* **3**, 243 (2011).
- [124] A. Gianoncelli, L. Vaccari, G. Kourousias, D. Cassese, D. E. Bedolla, S. Kenig, P. Storici, M. Lazzarino, and M. Kiskinova<sup>1</sup>, *Scientific Reports* **5**, 10250 (2015).
- [125] R. S. Kumar, A. Svane, G. Vaitheeswaran, Y. Zhang, V. Kanchana, M. Hofmann, S. J. Campbell, Y. Xiao, P. Chow, C. Chen, Y. Zhao, and A. L. Cornelius, *Inorg. Chem.* **52**, 832 (2013).

- [126] R. B. Hughes-Currie, K. V. Ivanovskikh, J.-P. R. Wells, M. F. Reid, and R. A. Gordon, *J. Phys.: Condens. Matter* **28**, 135502 (2016).
- [127] A. L. Ankudinov and J. J. Rehr, *Phys. Rev. B* **56**, R1712 (1997).
- [128] F. Bridges, J. Castillo-Torres, B. Car, S. Medling, and M. Kozina, *Phys. Rev. B* **85**, 064107 (2012).
- [129] F. Bridges, B. Car, L. Sutton, M. Hoffman-Stapleton, T. Keiber, R. E. Baumbach, M. B. Maple, Z. Henkie, and R. Wawryk, *Phys. Rev. B* **91**, 014109/1 (2015).
- [130] P. Görlich, H. Karras, C. Symanowski, and P. Ullmann, *Phys. Status Solidi* **25**, 93 (1968).
- [131] E. Friedman and W. Low, *J. Chem. Phys.* **33**, 1275 (1960).
- [132] J. Sierro, *Phys. Lett.* **4**, 178 (1963).
- [133] Z. Barandiarán, A. Meijerink, and L. Seijo, *Phys. Chem. Chem. Phys.* **17**, 19874 (2015).
- [134] Z. Barandiarán and L. Seijo, *J. Chem. Phys.* **143**, 144702 (2015).
- [135] J. Sugar and N. Spector, *J. Opt. Soc. Am.* **54**, 1484 (1974).
- [136] V. Kaufman and J. Sugar, *J. Opt. Soc. Am.* **66**, 1019 (1976).
- [137] W. C. Martin, R. Zalubas, and L. Hagan, *Atomic Energy Levels - The Rare Earth Elements*, Natl. Stand. Ref. Data Ser., Natl. Bur. Stand. No. 60 (U. S. GPO, Washington, D. C., 1978).
- [138] F. Bridges, *Mod. Phys. Lett. A* **30**, 630001/1 (2016), doi: 10.1142/S0217984916300015.
- [139] C. MacKeen, F. Bridges, L. Kovács, and J. Castillo-Torres, *Phys. Rev Materials* **2**, 093602 (2018).
- [140] M. D. Fontana and P. Bourson, *Appl. Phys. Rev.* **2**, 040602 (2015).
- [141] S. Sanna and W. G. Schmidt, *J. Phys.: Condens. Matter* **29**, 413001 (2017).
- [142] S. Nahar, M. F. M. Zain, A. A. H. Kadhum, H. A. Hasan, and M. R. Hasan, *Materials* **10**, 629 (2017).
- [143] L. A. A. García-Cabañes, A. Blázquez-Castro, F. Agulló-López, and M. Carras-cosa, *Crystals* **8**, 65 (2018).
- [144] F. Xin, G. Zhang, F. Bo, H. Sun, Y. Kong, J. Xu, T. Volk, and N. M. Rubinina, *J. Appl. Phys.* **107**, 33113 (2010).

- [145] Y. Kong, S. Liu, and J. Xu, *Materials* **5**, 1954 (2012).
- [146] K. Lengyel, Á. Péter, L. Kovács, G. Corradi, L. Pálfalvi, J. Hebling, M. Unferdorben, G. Dravecz, I. Hajdara, Z. Szaller, and K. Polgár, *App. Phys. Rev.* **2**, 040601 (2015).
- [147] J. G. Marques and K. Lorenz, *Opt. Eng.* **53**, 060901 (2014).
- [148] M. Wöhlecke, G. Corradi, and K. Betzler, *Appl. Phys. B* **63**, 323 (1996).
- [149] D.-L. Zhang, C.-X. Qiu, W.-H. Wong, and E. Y.-B. Pun, *Mater. Research Bull.* **60**, 771777 (2014), <http://dx.doi.org/10.1016/j.materresbull.2014.09.064>.
- [150] M. Bazzan and C. Sada, *Appl. Phys. Rev.* **2**, 040603 (2015), <http://dx.doi.org/10.1063/1.4931601>.
- [151] D. Zheng, Y. Kong, S. Liu, J. Yao, L. Zhang, S. Chen, and J. Xu, *AIP Advances* **5**, 017132 (2015).
- [152] L. Li, Y. Li, and X. Zhao, *Phys. Rev. B* **96**, 115118 (2017).
- [153] B. Grabmaier, W. Wersing, and W. Koestler, *J of Cryst. Growth* **110**, 339 (1991).
- [154] N. Iyi, K. Kitamura, Y. Yajima, S. Kimura, Y. Furukawa, and M. Sato, *J. Solid State Chem.* **118**, 148 (1995).
- [155] J. Liu, W. Zhang, and G. Zhang, *Phys. Stat. Sol. (a)* **156**, 285 (1996).
- [156] S. C. Abrahams, J. M. Reddy, and J. L. Bernstein, *J. Phys. Chem. Solids* **27**, 997 (1966).
- [157] S. C. Abrahams, H. J. Levinstein, and J. M. Reddy, *J. Phys. Chem. Solids* **27**, 1019 (1966).
- [158] H. D. Megaw, *Acta Cryst. A* **24**, 583 (1968).
- [159] L. Kovács, Z. Szaller, K. Lengyel, and G. Corradi, *Opt. Mater.* **37**, 55 (2014).
- [160] M. Wöhlecke and L. Kovács, *Crit. Rev. Solid State Mater. Sci.* **26**, 1 (2001).
- [161] F. Bridges, C. MacKeen, and L. Kovács, *Phys. Rev. B* **94**, 014101 (2016).
- [162] A. A. Kaminskii, *Laser Crystals*, 2nd ed. (Springer-Verlag, Berlin/Heidelberg, Germany; New York, NY, USA, 1990), pp. 210–212.
- [163] Y. Sun, C. W. Thiel, R. L. Cone, R. W. Equall, and R. L. Hutcheson, *J. Lumin.* **98**, 281 (2002).
- [164] D. Bravo, A. Martín, and F. J. López, *Solid State Commun.* **112**, 541 (1999).

- [165] L. Kovács, L. Kocsor, Z. Szaller, I. Hajdara, G. Dravecz, K. Lengyel, and G. Corradi, *Crystals* **7**, 230 (2017).
- [166] F. A. Kröger and H. J. Vink, *Solid State Phys.* **3**, 307 (1956).
- [167] I. Baumann, R. Brinkmann, M. Dinand, W. Sohler, L. Beckers, C. Buchal, M. Fleuster, H. Holzbrecher, H. Paulus, K.-H. Müller, T. Gog, G. Materlik, O. Witte, H. Stolz, and W. von der Osten, *Appl. Phys. A* **64**, 33 (1997).
- [168] C. Prieto, C. Zaldo, P. Fessler, H. Dexpert, J. A. Sanz-Garcia, and E. Dieguez, *Phys. Rev. B* **43**, 2594 (1991).
- [169] C. Zaldo and C. Prieto, *Ferroelectrics* **134**, 47 (1992).
- [170] C. Prieto and C. Zaldo, *J. Phys.: Condens. Matter* **6**, L677 (1994).
- [171] J. J. Rehr, R. C. Albers, and S. I. Zabinsky, *Phys. Rev. Lett.* **69**, 3397 (1992).
- [172] S. I. Zabinsky, J. J. Rehr, A. L. Ankudinov, R. C. Albers, and M. J. Eller, *Phys. Rev. B* **52**, 2995 (1995).
- [173] A. McKale, B. Veal, A. Paulikas, S.-K. Chan, and G. Knapp, *J. Amer. Chem. Soc.* **110**, 3763 (1988).
- [174] J. Rehr, J. M. de Leon, S. Zabinsky, and R. Albers, *J. Am. Chem. Soc.* **113**, 5135 (1991).
- [175] Y. Kong, J. Deng, W. Zhang, J. Wen, G. Zhang, and H. Wang, *Phys. Lett. A* **196**, 128 (1994).
- [176] B. Hauer, R. Vianden, J. G. Marques, N. P. Barradas, J. G. Correia, A. A. Melo, J. C. Soares, F. Agulló-López, and E. Dieguez, *Phys. Rev. B* **51**, 6208 (1995).
- [177] L. Rebouta, M. da Silva, J. Soares, J. Sanz-García, E. Dieguez, and F. Agulló-López, *Nucl. Instru. Meth. Phys. Res. B* **64**, 189 (1992).
- [178] M. G. Th. Gog and G. Materlik, *Phys. Lett. A* **181**, 417 (1993).
- [179] V. Dierolf and M. Koerdt, *Phys. Rev. B* **61**, 8043 (2000).
- [180] V. Dierolf and C. Sandmann, *J. Lumin.* **125**, 67 (2007).
- [181] T. P. Th. Nolte and J.-M. Spaeth, *Solid State Commun.* **104**, 53.5 (1997).
- [182] R. Hammoum, M. Fontana, M. Gilliot, P. Bourson, and E. Kokanyan, *Solid State Commun.* **149**, 1967 (2009).
- [183] J. G. Marques, A. Kling, J. Soares, L. Rebouta, M. da Silva, E. Diéguez, and F. Agulló-López, *Nucl. Instru. Meth. Phys. Res. B* **136-138**, 431 (1998).

- [184] H. Xu, D. Lee, S. Sinnott, V. Dierolf, V. Gopalan, and S. Phillpot, *J. Phys.: Condens. Matter* **22**, 135002/1 (2010).
- [185] H. Blume, T. Bader, and F. Lüty, *Optics Commun.* **12**, 147 (1974).
- [186] W. M. Kelly and F. Bridges, *Phys. Rev. B.* **18**, 4606 (1978).
- [187] B. Y. Price, G. Hardal, M. Açıkgöz, S. Repp, and E. Erdem, *J. Appl. Phys.* **118**, 175705 (2015).
- [188] E. Erdem, R. Böttcher, H.-J. Gläsel, and E. Hartmann, *Magn. Reson. Chem.* **43**, S174 (2005).
- [189] S. Jang, B. D. White, I. K. Lum, H. Kim, M. A. Tanatar, W. E. Straszheim, R. Prozorov, T. Keiber, F. Bridges, L. Shu, R. E. Baumbach, M. Janoschek, and M. B. Maple, *Phil. Mag.* **94**, 4219 (2014), <http://dx.doi.org/10.1080/14786435.2014.976287>.
- [190] K. Polgár, A. Péter, L. Kovács, G. Corradi, and Z. Szaller, *J. Crystal Growth* **177**, 211 (1997).